Università degli Studi di Genova

Facoltà di Scienze Matematiche, Fisiche e Naturali
XVII Ciclo

Tesi di Dottorato in Fisica

Real Time Tracking with ATLAS Silicon Detectors and its Applications to Beauty Hadron Physics

Candidato:

Carlo Schiavi

Relatore:
Dr. Paolo Morettini

Relatore esterno:
Dr. John T. M. Baines

Contents

Introduction

The purpose of the work presented here is a complete characterization of a track reconstruction algorithm, designed to operate in the on-line event selection system of the ATLAS experiment.
The ATLAS (A Toroidal LHC ApparatuS) experiment will start taking data in 2007 at the Large Hadron Collider (LHC), a proton-proton collider, which is currently under construction at the European Organization for Nuclear Research (CERN). At the LHC, protons will collide at a center of mass energy of 14 TeV, with a bunch spacing of 25 ns and a design luminosity of $10^{34}\,\mathrm{cm}^{-2}\,\mathrm{s}^{-1}$.
ATLAS is a multipurpose experiment, designed to cover various aspects of high energy physics phenomenology: discovering new physical phenomena, like Higgs bosons or supersymmetrical particles, predicted by theories compatible with the current experimental observations; performing precision Standard Model (SM) studies, like measurements of the t quark and W boson masses; detecting possible unexpected signals from unpredicted physics scenarios.
The very high LHC design luminosity, while allowing to observe phenomena characterized by a low cross section, poses, on the other hand, stringent design demands on both the detectors and the trigger system. Operating at design luminosity, $\sim 23\,pp$ interaction will occur at every bunch crossing, i.e. every 25 ns, in addition to any interesting physics events, while the final data storage rate will be limited to about 200 events per second. Hence, an efficient on-line event selection strategy has to be put in place, in order to reject most of the events containing uninteresting background collisions, while preserving as much as possible the interesting physical signals.
Another important design requirement for the trigger system comes from the wide physics programme envisaged for the ATLAS experiment; infact, the experiment's trigger strategy must be capable of switching between different configurations, in order to be adapted to external factors, such as changes in the luminosity and the physical background conditions or the topology of the new phenomena that will be presumably discovered once LHC will start its operations.
In order to meet these performance and flexibility requirements, the on-line event selection for the ATLAS experiment is implemented through three different trigger selection layers; an hardware-based trigger selection performs a preliminary rejection using only data coming from the calorimeters and the muon detectors; further event selection is then performed by software tools running on dedicated commercial processor farms and is implemented in two layers, the Second Level trigger (LVL2) and the Event Filter (EF), collectively referenced as High Level Trigger (HLT).

In case of crowded hadronic environments, such as LHC, track reconstruction proves to be one of the most powerful selection ingredients, both in terms of flexibility and rejection power. In the ATLAS experiment, track reconstruction is based on three different detector subsystems: moving from the beam line toward the outer detector layers, we find two Silicon detectors, respectively adopting pixel and strip sensor elements and providing precise three-dimensional measurements, and a detector based on straw tubes, granting additional particle identification capabilities.
As already mentioned, the work presented here will provide a complete characterization of a track reconstruction algorithm, SiTrack, based on data coming from the silicon detectors and designed to operate at LVL2. Given the stringent timing constraints imposed on LVL2 algorithms in order to meet the required rate reduction, the algorithm will be characterized not only in terms of reconstruction performance but also in terms of execution time.
After a more detailed overview of the physical motivations of the ATLAS experiment (chapter 1), of its general design (chapter 2) and, in particular, of its high level trigger scheme (chapter 3), the track reconstruction strategy implemented in the SiTrack algorithm will be described in detail and the results in terms of single track reconstruction will be provided (chapter 4).
Then the application of the SiTrack algorithm to different physics selections will be discussed and the corresponding results will be provided, both in terms of pure tracking performance and of impact on the physical event selection strategy. The following cases will be covered in detail:

- identification of high momentum isolated electrons (chapter 5); in this selection, tracks identified by the tracking detectors are matched to the energy deposits in the calorimeters. As a consequence, a good resolution of the directional parameters of the reconstructed tracks is required;

- identification of jets containing beauty hadrons (chapter 6), usually referred to as b-tagging; in this case the most stringent requirement is posed on the purity of the reconstructed track sample, even for particles having a low momentum ($\sim$2 GeV), to avoid feeding the flavour tagging algorithms with fake track candidates. In this chapter much effort will be put not only on optimizing the track reconstruction algorithm, but also on the definition on the on-line b-tagging selection strategy;

- selection of decay channels relevant to B-physics studies (chapter 7); in this case the reconstruction efficiency has to be stable with respect to the particle's momentum, down to values around $\sim$ 1.5 GeV. The reconstruction of both exclusive and semi-inclusive hadron decays will be addressed, characterizing the physics selection performance not only in terms of the efficiency for signal events, but also in terms of the corresponding LVL2 output trigger rate. Infact this parameter is strongly constrained by the ATLAS trigger budget and thus plays a fundamental role in the definition of every trigger selection strategy.

Besides being one of the most demanding application for on-line track reconstruction, B-physics studies are also the ones for which the interplay between the adopted trigger strategy

and the offline analyses is more evident. So, chapter 8 will discuss the impact of the trigger selection described in chapter 7 on the set of measurements that could be achieved in ATLAS. After a brief overview of flavour physics, the present status of the Unitarity Triangle determination is presented, along with the expected ATLAS reach in this sector. In particular, the attention will focus on studies regarding the $B_s^0 - \bar{B}_s^0$ mixing properties and the measurement of the corresponding Δm_s parameter.
The choice of using this measurement as a testing bench for the physical impact of the online track trigger is guided by two main considerations; first of all, the determination of the Δm_s parameter, if not previously measured by other experiments, will probably represent the most important B-physics outcome of the ATLAS experiment and, in general, of the experiments operating at LHC; furthermore, since it is measured in the decay channels posing the most stringent demands on HLT track reconstruction algorithms, its study contributes significantly to a complete characterization of SiTrack's performance.
From this point of view, the possible contribution of the ATLAS experiment to the Δm_s measurement will be determined as a function of the trigger performance obtained in previous chapters.

Chapter 1

Particle Physics and Future Hadronic Experiments

1.1 Historical remarks

Elementary particle physics made impressive progress in the second half of the last century, both from the theoretical and the experimental point of view. This led to the formulation of a comprehensive theory of particle physics, known as the Standard Model (SM), which correctly describes all known interactions in physics, except for the gravitational one. This doesn't mean that a deeper understanding of elementary interactions is not possible and that no further experimental and theoretical efforts are needed, since the Standard Model suffers from many limitations, as discussed later in this chapter; nevertheless it is certainly a very solid basis against which any new theory or experimental result must be tested.
Even if the most significant ideas upon which the SM is based came out only in the last fifty years, the origins of modern elementary particle physics may be traced back to the first half of 1900; in particular, the success of quantum electrodynamics in the late 1940's showed that quantum field theory was the right approach to the description of fundamental interactions. That fertile decade was then followed by a period of disillusionment; the four-fermion theory of weak interactions was proved not to be renormalizable, and thus useless at any order in perturbation theory apart from the lowest one; on the other hand, the Yukawa theory proposed as a description of strong interactions, even if renormalizable, could not be used in perturbation theory to produce any phenomenological predictions, given the big coupling constant of strong interactions. Furthermore both these theories looked like they had been tuned to fit the experimental measurements, but no coherent picture of weak and strong interactions was available. It was during the 1950's and 1960's that three fundamental ideas emerged, even if they weren't immediately recognized as such, leading to the development of modern elementary particle physics [1].
First of all, in 1964 the quark model was independently proposed by Gell-Mann and Zweig [2]. They suggested that hadrons are made of quarks and antiquarks, thus explaining to some extent the list of observed hadrons, continuously expanding at that time. Furthermore, the quark model very soon got experimental confirmation in 1968, from the SLAC experiment

led by Friedman, Kendall, and Taylor [3].
The second turning point was the idea of gauge or local symmetry, used by Yang and Mills [4] who, in 1954, constructed a theory based on the three-dimensional SU(2) group, in order to apply it to strong interactions. The interesting peculiarities of this theory were that the form of the interactions directly followed from the chosen symmetry and that its lagrangian contained self-interaction terms for the gauge bosons. However these theories were proved to become non-renormalizable as soon as any explicit mass term is inserted in the lagrangian; this was an evident obstacle to their application to the weak or the strong interactions.
This problem was finally overcome with the third fundamental idea, that of spontaneously broken symmetry, i.e. the possibility of having symmetries of the lagrangian which are not symmetries of the vacuum. In 1962 Goldstone, Salam and Weinberg [5] proved that each spontaneously broken symmetry leads to the existence of a massless spinless particle, while Higgs [6] in 1964 showed that the Goldstone theorem does not apply to local gauge symmetries like the SU(2) of the Yang-Mills theory. In that case the Goldstone boson is still in the theory, but goes into the helicity-zero part of a gauge boson, to which is thereby attributed a mass.
These ingredients were then brought together, in the late 1960's, into a coherent description of electroweak interactions by Weinberg [7] and Salam [8] and, in addition, were used to build the quantum chromodynamics theory describing strong interactions. At this point the Standard Model and its many predictions were ready to be tested in various experiments, as described in the next section. In the following sections a brief overview of possible SM extensions of the experiments which should test them in the next few years is given.

1.2 The Standard Model

In this section the Standard Model is described in a slightly more detailed way; first of all a very simple overview of its theoretical foundations is given and then the main related experimental achievements and open problems are discussed.

1.2.1 Theoretical overview

The Standard Model describes the interaction between pointlike spin 1/2 fermions, mediated by spin 1 gauge bosons [9]. The elementary fermions of this theory are listed in table 1.1, along with their basic properties.
As far as the electroweak sector is concerned, the four-fermion theory of low energy interactions, mentioned in the previous section, was based on a non-renormalizable effective lagrangian, the so called Fermi lagrangian, which contained a product of axial and vector currents for each physical process it described. As an example, the μ and the nucleon β decays are described by

$$\mathcal{L} = -\frac{G^{(\beta)}}{\sqrt{2}}\bar{p}\gamma^{\alpha}(1 - a\gamma_5)n\bar{e}\gamma_{\alpha}(1-\gamma_5)\nu_e - \frac{G^{(\mu)}}{\sqrt{2}}\bar{\nu}_{\mu}\gamma^{\alpha}(1-\gamma_5)\mu\bar{e}\gamma_{\alpha}(1-\gamma_5)\nu_e$$

where $G^{(\beta)} = G^{(\mu)} = G_F = 1.16639 \times 10^{-5}$ GeV^{-2} and $a = 1.239 \pm 0.09$, and where each fermionic field is identified with the symbol of its corresponding particle.

Family	Leptons			Quarks		
	Flavour	Charge (e)	Mass (GeV)	Flavour	Charge (e)	Mass (GeV)
1st	ν_e	0	$< 5 \cdot 10^{-9}$	u	2/3	$2 \div 8 \cdot 10^{-3}$
	e	-1	$511 \cdot 10^{-6}$	d	-1/3	$5 \div 15 \cdot 10^{-3}$
2nd	ν_μ	0	$< 0.3 \cdot 10^{-3}$	c	2/3	$1.0 \div 1.6$
	μ	-1	$106 \cdot 10^{-3}$	s	-1/3	$0.1 \div 0.3$
3rd	ν_τ	0	< 0.03	t	2/3	176 ± 13
	τ	-1	1.777	b	-1/3	$4.1 \div 4.5$

Table 1.1: The elementary Standard Model fermions (spin $\frac{1}{2}$) with their charges and masses. In addition to the particles listed here, for each fermion exists a corresponding antiparticle having the same mass and spin but opposite charge; furthermore the quarks are also characterized by the colour quantum number, which can take three different values.

This theory, though effective in describing the experimental observations, was not renormalizable, as follows from the fact that it contains terms with a mass dimension higher than four, thus violating a necessary condition for perturbative renormalization.
Anyway, following the ideas introduced in the previous section, a renormalizable description of weak interactions can be obtained with a gauge theory, i.e. requiring local invariance with respect to the action of some transformation group. This theory has then to reduce to the Fermi one in the low energy limit; in the gauge theory framework, this behaviour can be interpreted as the exchange of a massive intermediate vector boson with a momentum lower than its mass.
The group of local invariance can be then chosen by studying the currents in the Fermi lagrangian. As an example, the one involving the electron and its neutrino,

$$J_\mu = \bar{\nu}_e \gamma_\mu \frac{1}{2}(1 - \gamma_5) e$$

can be rewritten as

$$J_\mu = \bar{L} \gamma_\mu \tau^+ L$$

where

$$L = \frac{1}{2}(1 - \gamma_5) \begin{pmatrix} \nu_e \\ e \end{pmatrix} = \begin{pmatrix} \nu_{eL} \\ e_L \end{pmatrix}, \qquad \tau^+ = \frac{1}{2}(\tau_1 + i\tau_2),$$

ν_L and e_L are the left-handed neutrino and electron fields and τ_i are Pauli matrices; then weak interaction processes will also be described by the hermitian conjugate current, involving τ^-. finally, since the group generators form a closed set with respect to the commutation operation, the

$$\tau_3 = [\tau^+, \tau^-]$$

generator will correspond to the neutral current

$$J_3^\mu = \bar{L} \gamma^\mu \tau_3 L.$$

Choosing this set of currents leads to a gauge theory invariant with respect to the $SU(2)$ symmetry group, whose generators are the Pauli matrices. In this theory the left-handed neutrino and electron fields form an $SU(2)$ doublet, while their right-handed components, which never appear in weak interactions, must be then assigned to the singlet representation of $SU(2)$.
The same procedure can be then repeated for each lepton family. However the symmetry group is not yet complete, if we want to describe coherently both weak and electromagnetic interactions. As a matter of fact, the neutral J_3^μ current cannot be identified with the electromagnetic one, which doesn't distinguish between left and right-handed components and doesn't contain neutrino fields.
The easiest way to extend the symmetry group in order to contain another neutral generator is the addition of an Abelian $U(1)$ factor, obtaining

$$SU(2) \rightarrow SU(2) \otimes U(1).$$

The covariant derivative for this gauge then becomes

$$D^\mu = \partial^\mu - igW_i^\mu T_i - ig'\frac{Y}{2}B^\mu$$

where W_i^μ and B^μ are gauge vector fields, g and g' are the coupling constants associated with the $SU(2)$ and $U(1)$ factors respectively, T_i are the generators of $SU(2)$ ($T_i \equiv \tau_i/2$ when acting on the doublet and $T_i \equiv 0$ when acting on the singlet) and Y is a diagonal matrix bearing the hypercharge quantum numbers associated to each field.
The vector fields can be rearranged as

$$\begin{aligned} W_\mu^\pm &= \frac{1}{\sqrt{2}}(W_\mu^1 \mp iW_\mu^2), \\ B^\mu &= A^\mu cos(\theta_W) - Z^\mu sin(\theta_W), \\ W_3^\mu &= A^\mu sin(\theta_W) + Z^\mu cos(\theta_W) \end{aligned}$$

where the Weinberg angle θ_W must satisfy the relation

$$gsin\theta_W = g'cos\theta_W = e,$$

in order to identify the A^μ field with the photon one. From this follows the relation

$$T_3 + \frac{Y}{2} = Q$$

where $T_3 = \pm 1/2$ respectively for the upper and lower $SU(2)$ left-handed doublet components, $T_3 = 0$ for the right-handed fields and Q is the electromagnetic charge quantum number. In this way a one-to-one correspondence is obtained between the bosons of the theory and the experimentally observed ones, whose properties are summarized in table 1.2.
This theory can then be extended to the hadronic sector, whose charged current is

$$J^\mu = \bar{Q}\gamma^\mu \tau^+ Q$$

Interaction	Coupling strength	Boson	Charge (e)	Mass (GeV)
Electromagnetic	$\alpha = 1/137$	γ	0	0
Weak	$\alpha_w = 1.02 \cdot 10^{-5}$	$W^{\pm}$	± 1	80.22 ± 0.26
		Z^0	0	91.187 ± 0.007

Table 1.2: Gauge bosons (spin 1) in the Standard Model electroweak sector. The strength of each interaction is parametrized by an adimensional coupling constant.

where Q is an $SU(2)$ left-handed doublet representing a quark family, e.g. $Q = \begin{pmatrix} u_L \\ {d'}_L \end{pmatrix}$ and

$$\begin{pmatrix} {d'}_L \\ {s'}_L \\ {b'}_L \end{pmatrix} = V \begin{pmatrix} d_L \\ s_L \\ b_L \end{pmatrix}$$

where V is the 3×3 Cabibbo-Kobayashi-Maskawa (CKM) unitary matrix, responsible for the charged flavour changing currents, described in more detail in chapter 8.
As mentioned before, this theory reduces to the Fermi one in the low energy limit, provided that the weak gauge bosons are massive; but no explicit mass term can be added to the lagrangian if we want to preserve the renormalizability requirement. A possible solution is the introduction of an additional scalar field in the theory, spontaneously breaking its symmetry. A couple of requirements guides the choice of this scalar field; first of all it must transform in a non-trivial way under the action of the symmetry it breaks; then the correct choice must also preserve the electromagnetic $U(1)$ invariance, in order for the photon to remain massless. This leads to the introduction of a scalar Higgs field ϕ assigned to the doublet $SU(2)$ representation

$$\phi = \begin{pmatrix} \phi_1 \\ \phi_2 \end{pmatrix}$$

for which the most general gauge invariant and renormalizable potential

$$V(\phi) = m^2|\phi|^2 + \lambda|\phi|^4$$

is chosen; the minimum for this potential can be calculated and the choice for the corresponding value of ϕ is constrained by requiring that the minimum is invariant for electromagnetic $U(1)$ transformations, obtaining

$$|\phi|^2 = -\frac{m^2}{2\lambda} \equiv \frac{1}{2}v^2, \quad \phi = \frac{1}{\sqrt{2}} \begin{pmatrix} 0 \\ v \end{pmatrix}, \quad Y(\phi) = +1, \quad Q(\phi_1) = 1, \quad Q(\phi_2) = 0.$$

The Higgs doublet can be thus reparametrized as

$$\phi = \frac{1}{\sqrt{2}} e^{i\tau^i \theta^i / v} \begin{pmatrix} 0 \\ v + H \end{pmatrix},$$

where θ and H are real scalar fields.
Applying this parametrization to the scalar potential, the mass of the Higgs field can be calculated as

$$m_H^2 = 2\lambda v^2;$$

furthermore, in the kinetical term $(D^\mu\phi)^\dagger D_\mu\phi$, a mass term appears for each vector boson, thus acquiring masses

$$m_W^2 = \frac{1}{4}g^2v^2$$
$$m_Z^2 = \frac{1}{4}(g^2 + g'^2)v^2.$$

In order to provide a mass for the elementary spinors, other terms must be added to the SM lagrangian. In particular, for the quarks a Yukawa interaction term between both their left- and right-handed components and the Higgs field is added. This coupling term can be written as

$$\mathcal{L} = -\frac{1}{\sqrt{2}}(v+H)\sum_{f=1}^{3}(h_D^f \bar{d}^f d^f + h_U^f \bar{u}^f u^f),$$

where h_U and h_D are diagonal matrices; these matrices, entering the charged current lagrangian terms, are strictly related to the CKM matrix and are responsible for flavour changing and mixing phenomena, as will be discussed in more detail in chapter 8.
A similar approach can be followed for the leptonic sector; however in this case, since the right-handed neutrino fields don't interact at all, the same Yukawa coupling matrix h_E can be used for both charged leptons and left-handed neutrinos. Thus, the Yukawa interaction results

$$\mathcal{L} = -\sum_{f=1}^{3} h_E^f(\bar{L}^f\phi e_R^f + \bar{e}_R^f\phi^\dagger L^f),$$

while, unlike what happens in the quark sector, the charged current lagrangian terms are left unchanged and no leptonic flavour changing phenomena are admitted. This isn't true anymore if a mass has to be introduced for the neutrino fields, as seems to be the case from experimental evidence. In this case the Yukawa interaction for the leptonic sector is similar to the hadronic one and the mixing between different leptonic flavours is described in terms of a single unitary matrix.
Moving to the strong interactions sector, it is clear from experimental observations that each quark flavour can come in three different colours, which correspond to an additional quantum number. Furthermore, observable hadrons are neutral in colour and therefore have to belong to the singlet representation of the colour symmetry group. Another experimental hint toward the construction of a theory of strong interactions is given by the fact that it has to be asymptotically free, i.e. weakly coupled at high energies.
The only known asymptotically free four-dimensional field theories are the gauge theories based on non-Abelian symmetry groups; it is thus natural to choose $SU(3)$ as the transformation group describing the colour symmetry, which is considered to be exact. In this case there is no need for a symmetry breaking mechanism and the theory, known as Quantum

Chromo Dynamics (QCD), is automatically renormalizable. This model predicts the existence of eight different massless vector bosons, the gluons; these, unlike the electromagnetic photon, carry a colour charge and can thus self-interact.
The main QCD achievement is the explanation of both the low energy symmetry properties observed in the hadron spectrum and the asymptotic freedom at high energies. Furthermore this is obtained without spoiling the coherence of the electroweak theory, since the $SU(3)$ colour commutes with the electroweak $SU(2) \otimes U(1)$ group. On the other hand, the fact that QCD is based on the same mechanisms as the electroweak theory, opens the possibility for a uniform and unified description of both sectors in terms of gauge theories.
Nevertheless QCD is still unable to rigorously explain basic phenomena like colour confinement, i.e. the fact that the only quantities we can observe belong to the singlet representation of $SU(3)$. Furthermore, at low energies, QCD becomes a strongly interacting theory and the only possible way to perform calculations is by computer simulation of QCD on a lattice, that is to say on a finite discrete model of space-time. Anyway, since essentially no viable alternative theory has been formulated so far, a significant effort both in theoretical and experimental physics is devoted to testing QCD predictions.

1.2.2 Fundamental experimental validation

The first experimentally tested Standard Model prediction was the existence of neutral currents; the SM was not the first theory predicting them, but in its case their strength could be also calculated. Infact, it was shown that although, in the electroweak theory, they are somewhat weak compared to the ordinary charged-current weak interactions, they are not too weak to be seen [10]. In particular, it was pointed out that the ratio of elastic neutrino-proton scattering to the corresponding inelastic charged-current reaction would have a value between 0.15 and 0.25, depending on the value of the angle θ_W. In 1970 an experiment [11] had given a value of 0.12 ± 0.06 for this ratio, but the evidence for neutral currents was not yet clear, so this result was quoted as an upper bound. Neutral currents were finally discovered in 1973 at CERN [12] and the parity violation they introduced was measured at the expected level in electron-nucleon scattering at SLAC in 1978 [13], granting the electroweak theory a striking first success.
From the experimental point of view, another step toward the completion of the Standard Model was the discovery of the third generation: the τ lepton [14] (and the corresponding neutrino) and the bottom [15] and top [16] quarks. This provided a new mechanism for CP violation, the complex phase factor in the Cabibbo-Kobayashi-Maskawa matrix [17], which appears in the semi-leptonic weak interactions. The fact that the third generation of quarks is only slightly mixed with the first two by this matrix, naturally explains why CP violation produced in this way is rather weak.
The Standard Model picture was finally complete in 1983 with the discovery [18] of the W and the Z intermediate vector bosons. It proved possible to measure their masses with great precision, and this allowed a stringent comparison between the electroweak theory and experimental results. This comparison has even begun to provide hints of the properties of as yet undiscovered particles, as explained in the next section.
Even if those mentioned so far are the first important SM experimental validations, many

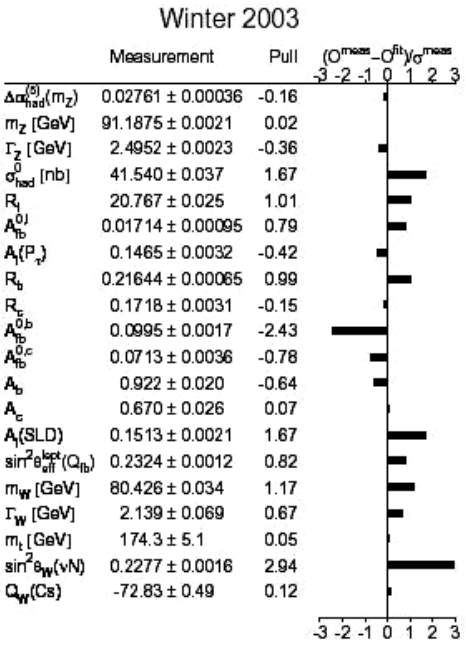

Figure 1.1: Standard Model measurements; agreement between theoretical predictions and their experimental determination.

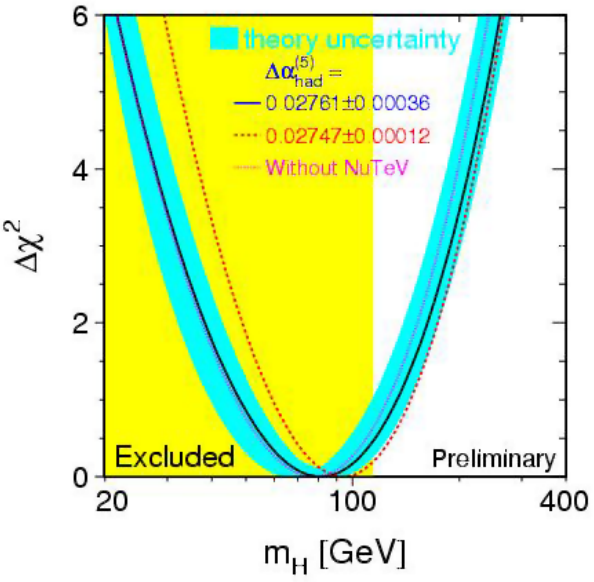

Figure 1.2: Constraints on Standard Model Higgs mass. The coloured region is ruled out by direct measurements.

other precision measurements have been made which are in remarkable agreement with theoretical predictions, mainly by the experiments that operated at the Large Electron-Positron collider (LEP). Some of them are shown in figure 1.1 and reported e.g. in [19] and [20].

1.2.3 Higgs boson searches

The Higgs boson has yet to be observed and the value of its mass can be constrained only weakly by theoretical considerations. On the other hand, tighter constraints come from experimental measurements: direct searches performed at LEP ruled out mass values lower than 114.4 GeV/c^2 (at the 95% confidence level). Indirect measurements obtained from electroweak parameters fit, like those involving radiative corrections to the W and t-quark masses, instead suggest $m_H = 96^{+60}_{-38}$ GeV, as shown in figure 1.2 [20].
As already mentioned said, theory grants less stringent constraints: a lower limit comes from the requirement of stability of the vacuum, while an upper limit can be evaluated requiring that the SM is valid up to a given energy scale Λ [21].

1.3 Beyond the Standard Model

In the previous sections the main successes of the Standard Model have been pointed out; it is a unitary and renormalizable theory describing particle interactions in amazing agreement

with experimental data; the Higgs mechanism, the simplest way of spontaneously breaking the gauge symmetry, also seems to be the best one; flavour symmetry can be broken by operating only on the charged current sector, again achieving consistency with the phenomenological observations, as described in chapter 8.
However, the Standard Model can't be considered a completely satisfactory theory and thus some possible extensions have been studied; both these aspects will be briefly covered in the next two sections.

1.3.1 Unsatisfactory aspects of the Standard Model

There are many reasons why the description of fundamental interactions cannot be considered to be complete in the Standard Model; amongst these:

- the origin of flavour symmetry breaking is not known; the mechanism proved to work very well, but the CKM picture is just a parametrization of the phenomenological observations and doesn't lead to any deeper theoretical insight;
- the feasibility of a grand unification, i.e. the unification of all fundamental forces in nature, is neither proved nor excluded; a first unification between fundamental interactions has been introduced in the Standard Model, describing electromagnetic and weak phenomena in terms of the same gauge symmetry, however the same is not true for strong and gravitational interactions;
- the Standard Model doesn't contain any description of the gravitational interactions in the context of quantum field theories.

In particular, the last two points lead to further questions, the so-called hierarchy and naturalness problems.
As a matter of fact, while the masses of all known particles, including the one predicted for the SM Higgs boson, are not far from the weak scale ($\mathcal{O}(200\text{GeV})$), other much larger scales have to become relevant at some point, namely the Planck scale ($M_P \sim 10^{19}$ GeV) and the grand unification scale ($M_{GUT} \sim 10^{16}$ GeV). The hierarchy problem corresponds to asking: why is the weak scale so much smaller than these other scales? Furthermore, while fermion and vector boson masses are naturally small, since their radiative corrections are proportional to the masses themselves, the same is not true for scalar particles. Infact these are not naturally small, since no symmetry is recovered as their masses vanish; this means that the mass of all the scalar particles, including the Higgs boson, should be strongly sensitive to any large energy scale, unless a fine tuning of theory parameters is performed. These considerations are usually known as the naturalness problem.
All these open issues are automatically answered in supersymmetrical theories, briefly described in the next section.

1.3.2 Overview of supersymmetrical theories

The most important extension proposed to overcome the difficulties arising in the Standard Model is the so-called supersymmetry [22]. Its main idea is the introduction of a symmetry between fermions and bosons; each fermionic SM particle has a bosonic partner and

vice-versa. In particular it turns out from general considerations that any supersymmetric multiplet of the new symmetry must contain an equal number of fermionic and bosonic degrees of freedom. In this way the fine tuning problem is automatically solved; as a matter of fact, with bosons and fermions in the same multiplet, scalar masses are protected by the same symmetry that protects fermion masses from large radiative corrections. Furthermore, it can be shown that the requirement of invariance with respect to a local supersymmetry paves the way for a description of gravitational interactions.
One supersymmetrical theory, called Minimal Supersymmetric Standard Model (MSSM), obtained by requiring that the gauge group is the SM one, has the following phenomenological implications:

- no supermultiplet can be formed out of standard particles (e.g. γ, μ);
- all the particles contained in the same supermultiplet have equal masses and equal gauge transformation properties, provided the supersymmetry is exact;
- matter fermions must belong to chiral supermultiplets, because left and right fermions transform differently under the weak gauge group;
- gauge bosons belong to gauge supermultiplets;
- two Higgs doublets are needed, along with their fermionic partners;
- R-parity is conserved; it is defined as $R = (-1)^{3(B-L)+2S}$ (where B is the barionic number, L is the leptonic number and S is the particle spin) and is equal to $+1$ for SM particles and Higgs bosons and -1 for supersymmetrical particles. As a consequence, superparticles are always produced in pairs and the Lightest Supersymmetric Particle (LSP) is stable.

The particle content of the MSSM is summarized in table 1.3.

Spin 0	**Spin 1/2**	**Spin 1**
$\tilde{u}_L$, $\tilde{d}_L$	u_L, d_L	
$\tilde{u}_R$	u_R	
$\tilde{d}_R$	d_R	
$\tilde{\nu}$, $\tilde{e}_L$	ν, e_L	
$\tilde{e}_R$	e_R	
H_u^+, H_u^0	$\tilde{h}_u^+$, $\tilde{h}_u^0$	
H_d^0, H_d^-	$\tilde{h}_d^0$, $\tilde{h}_d^-$	
	$\tilde{g}$	g
	$\tilde{w}^{\pm}$, $\tilde{w}^0$	$W^{\pm}$, W^0
	$\tilde{b}^0$	B^0

Table 1.3: Particle spectrum of the MSSM.

Supersymmetry has not been experimentally observed, so it has to be violated at an energy scale around 1 TeV, since the Standard Model proved to be valid below those energies. For the same reason the supersymmetrical partners of SM particles have to be heavier than those accessible at current accelerator facilities. This can be explained from the theoretical point of view since, while ordinary particles would be massless in the absence of spontaneous electroweak symmetry breaking, the contrary is true for their partners. Infact scalar masses are always allowed by gauge symmmetries and gauginos, the fermionic partners of vector bosons, do not belong to a chiral multiplet and thus no symmetry is recovered as they become massless.
Going back to the Higgs sector, it can be shown that the two Higgs doublets H_1 and H_2 can be reduced to five physical Higgs boson fields, namely the scalar fields h and H, the pseudoscalar field A and the charged fields $H^{\pm}$. These fields can be rewritten using the vacuum expectation values for H_1 and H_2, v_1 and v_2, often parametrized in terms of the A boson mass and $\tan\beta = v_2/v_1$. In the MSSM, Higgs bosons satisfy the following relations:

$$\begin{aligned} m_{H^{\pm}} &\geq m_W \\ m_h &\leq m_A \leq m_H \\ m_h &\leq m_Z |\cos 2\beta| \leq m_Z \\ m_h^2 + m_H^2 &= m_A^2 + m_Z^2 \end{aligned}$$

In particular, the third equation seems to conflict with experimental evidence, since the lower limit for Higgs boson masses is above 114.4 GeV. This contradiction is overcome taking into account radiative corrections, since in that case the upper mass limit for the h boson is set to 125 GeV.
Finally, another interesting feature of the MSSM is related to the coupling constants of the different interactions, which, in a general field theory, depend on the energy scale. The peculiar aspect of the MSSM is that the electromagnetic, weak and strong coupling constants converge and unify at a single energy scale, placed around 10^{16} GeV; the same isn't true in the Standard Model, where it is not possible to find a suitable energy scale. This feature is depicted in figure 1.3.

1.4 Future experimental searches

Today the primary interest of experimental particle physics is devoted to exploring those issues which are still open in the Standard Model and to testing possible extensions. These kinds of searches can follow two main directions; pursuing a direct discovery or performing very high precision measurements. The first route relies on the possibility of directly observing new phenomena foreseen in the different theoretical scenarios; an example is the production of supersymmetrical particles. This obviously means increasing the energy scale accessible at accelerator facilities, along with their luminosity, in order to have a significant probability of observing events characterized by small cross sections. However for these kinds of studies an extremely high precision on the measured quantities is not mandatory; so the most suitable choice for the corresponding experiments are hadronic accelerators. Infact, if

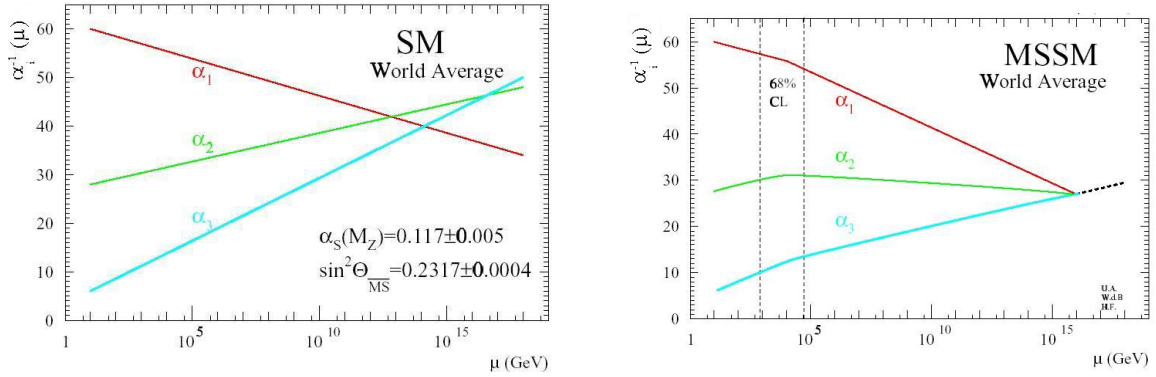

Figure 1.3: Evolution of the coupling constants for the electromagnetic, weak and strong interactions as a function of energy; the difference between MS and MSSM predictions is evidently shown.

confronted with leptonic machines, these grant a much easier way to span different energy ranges, at the cost of having to cope with problematic background conditions.
On the other hand, indirect searches aim at achieving very precise measurements of known quantities, hoping to find some small deviations, due to radiative corrections, with respect to the values predicted by the Standard Model. Leptonic machines are the best suited for these studies, since they provide a very clean environment and the possibility of performing a full reconstruction of the events. As a drawback, the maximum energy scale they can reach is not as high as for hadron accelerators; however this is not a limitation for these searches. Finally, a strategy shared by the two different approaches is that of looking for very rare decays, which are forbidden or highly suppressed in the SM.
In the next sections a brief overview is given of the experiments which should be able to explore the frontiers of high energy physics in the next few years. The case of leptonic machines will be treated first and then hadronic experiments will be covered, with particular emphasis on the Large Hadron Collider project.

1.4.1 Experiments using leptonic machines

As mentioned before, the experiments based on leptonic accelerators are the ones capable of providing the most precise measurements. They can be thus designed in order to perform multipurpose and discovery studies (like e.g. in the LEP era), but can also be used to achieve very precise and specialized measurements on a given set of phenomena; two examples of this approach will be discussed.
The BaBar and Belle experiments, based respectively at the PEP-II and KEKB linear electron-positron accelerators, are currently exploring the field of CP violation in the B meson decays. From these kinds of studies indirect evidence of the limitations of the CKM picture, which is the only way through which CP violation is introduced in the Standard Model, could be provided. In particular, as will be explained in more detail in chapter 8, were the direct measurements of quantities related to the angles and sides of the Unitarity Triangle (UT) to produce results inconsistent with the CKM picture, evidence for mecha-

nisms not foreseen by the SM would be provided.
The Muon Electron Gamma (MEG) experiment, instead proposes to search for the lepton flavour violating decay $\mu^+ \to e^+ \gamma$ with a sensitivity of 10^{-14}. In the Standard Model, lepton flavour conservation (LFC) is granted assuming vanishing neutrino masses; once neutrino masses and their mixing are introduced, the SM predicts unmeasurably small lepton flavor violation (LFV). On the other hand, supersymmetrical theories predict LFV at a measurable level. Processes such as $\mu^+ \to e^+ \gamma$, which should occur with a decay branching ratio somewhere above 10^{-14}, are therefore very clean, i.e. not contaminated by the background of the Standard Model, and provide a real chance of discovering evidence for new physics beyond the standard model. Anyway, even the non-observation of the decay at the foreseen experimental sensitivity will provide a stringent constraint on SUSY theories and will be thus of crucial importance for particle physics. The experiment will be conducted at PSI by using the πE5 beam, the most intense DC muon beam presently available in the world.

1.4.2 Experiments using hadronic machines

Among the experiments based at hadronic accelerators, the most important is the Collider Detector at Fermilab (CDF), which started its operation in 1985 and has recently entered its second run phase (Run II). It operates at the Tevatron collider, producing collisions of 1 TeV protons with 1 TeV anti-protons, which currently correspond to the highest energy ever achieved.
CDF has been designed as a multipurpose experiment, in order to achieve direct discoveries while also producing precise measurements of known quantities and granting the selection performance needed to observe very rare phenomena.
Undoubtedly its main achievement was the discovery of the top quark, claimed in 1995 in collaboration with D0 [27], the other experiment operating at Tevatron. The CDF physical program also included the direct search for Higgs bosons but, due to accelerator technical problems, the integrated luminosity values reached up to now are much lower than expected. As a consequence, since sensitivity beyond LEP exclusion would start at ~ 2 fb^{-1}, while Run II has collected less than 400 pb^{-1} since 2002, it is quite unlikely that the CDF contribution to Higgs searches will become significant before the Large Hadron Collider experiments, described in next section, will start taking data.
Anyway, CDF can still play an important role in the beauty hadron physics sector, e.g. studying B_s mixing properties as described in chapter 8. Furthermore, the very precise measurements of the W and t-quark masses will help to indirectly constrain the SM Higgs mass using electroweak fits. CDF will also carry on the search for rare decays such as B_s, B_d, $D^0 \to \mu^+\mu^-$, which should have very low ($< 10^{-9}$) branching ratios according to SM predictions. These BR could be enhanced up to $\mathcal{O}(10^{-7})$ in SUSY theories, so their precise determination could provide indirect evidence for new physics phenomena, while tighter upper limits would reduce the allowed region for SUSY parameters.
An even wider physics program is foreseen for the experiments that will operate at the Large Hadron Collider, as described in detail in next section.

1.4.3 The Large Hadron Collider

The Large Hadron Collider (LHC) is a proton-proton accelerator machine which is currently under construction at the European Organization for Nuclear Research (CERN) and is foreseen to become operational in late 2007; its main design characteristics are the unprecedented 14 TeV center-of-mass beam energy and the target luminosity of 10^{34} cm^{-2} s^{-1} . These design parameters forced the choice of accelerating and colliding two proton beams, although this isn't the easiest solution from the technological point of view. It would be impossible to use electron beams, like at LEP, since in that case the amount of energy lost by syncrotron radiation would be too high. The only way to reduce those losses in order to operate a circular accelerator at the TeV scale, would be to increase the ring radius well beyond practical feasibility. For a fixed beam energy and trajectory, syncrotron radiation becomes less relevant as particle mass increases; so the problems that prevent the acceleration of electrons are automatically solved in case much heavier particles, like protons, are used. So, from this point of view, it would be possible to accelerate and collide a proton and an antiproton beam; this choice would also exploit the simplification due to the fact that the beams, containing particles with the same mass and opposite charge, could be accelerated in opposite directions by the same bending magnetic field. But this solution has to be discarded too, since it is currently impossible to build an antiproton source powerful enough to grant the bunch density needed to achieve the desired luminosity.
The high LHC design luminosity is mandatory in order to produce, even at the highest energy value, a sufficient number of interesting collisions, granting both high precision measurements of already known physical quantities and a significant probability to observe new phenomena characterized by a low cross-section. Infact, since the number of collisions occurring in a fixed time interval is proportional to the luminosity and to the total cross-section, luminosity must grow as E^2, where E is the beam energy. This is due to the fact that, as E grows, the De Broglie wavelength of the particles decreases as $1/E$ and the corresponding cross-section decreases as $1/E^2$.
At LHC, in order to obtain a luminosity exceeding by two orders of magnitude the highest nowadays available, each accelerator cavity will be filled with 2835 bunches containing 10^{11} particles each and crossing the beams every 25 ns. In this way, by having on average 23 interactions per bunch crossing, an interaction rate of around 10^9 Hz will be obtained.
Due to the complexity of this project, the startup phase will probably be followed by a period of reduced luminosity (10^{32} cm^{-2}s^{-1}) running, that will be used to solve possible accelerator tuning problems. From the physics point of view, this phase will be devoted to perform high precision measurements exploiting the signal to background ratio, enhanced with respect to the high luminosity environment.
Even if LHC will be mainly used as a proton-proton collider, it is also designed to be able to accelerate and collide heavy ion beams, like lead ions, with a total collision energy exceeding 1.250 TeV, about thirty times higher than the one obtained by the RHIC (Relativistic Heavy Ion Collider) Brookhaven accelerator.
As shown in figure 1.4, four main experiments will study the collisions produced at LHC. ATLAS and CMS, studying proton-proton collisions, mainly aim at obtaining new evidence confirming or rejecting the Standard Model, possibly providing hints on its proposed exten-

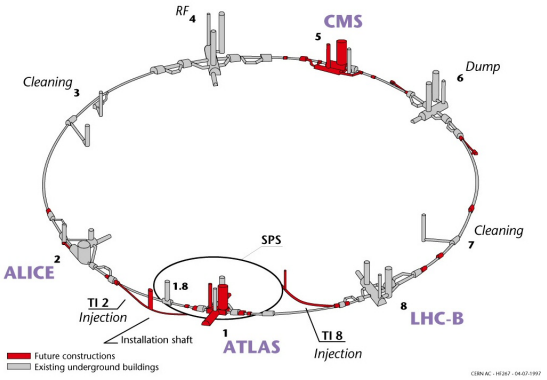

Figure 1.4: The LHC ring; the sites where the four experimental areas are placed are shown along the accelerator perimeter.

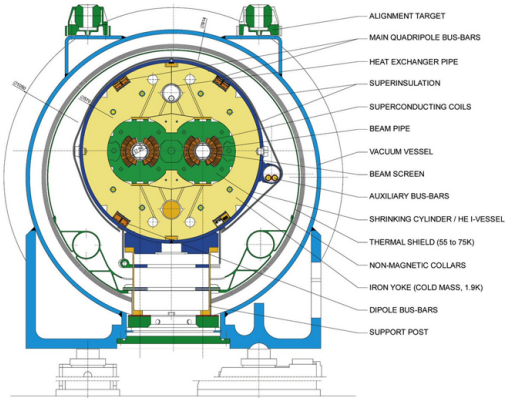

Figure 1.5: LHC dipole transverse section; the two proton beams will be accelerated in opposite directions by two separate cavities.

sions. In this context, their main interest is the search for particles which have never been directly observed, although foreseen by the current theories, like the Higgs boson. Anyway these two multi-purpose experiments will also be devoted to improve the measurement precision in already explored sectors.

In particular, CMS (Compact Muon Solenoid) strongly relies on very precise identification and measurement of muons, electrons and photons, using muon spectrometers and electromagnetic calorimeters. The energy resolution for these particle will be better than 1% at 100 GeV. These features should enable CMS to find out the electroweak symmetry breaking mechanism, to study top and beauty quarks and τ physics and to operate also on heavy ion collisions. In the CMS interaction area will also operate the TOTEM (Total Cross Section, Elastic Scattering and Diffraction Dissociation at the LHC) experiment.

A more detailed description of the ATLAS experiment will be provided in chapter 2.

LHCb (Large Hadron Collider beauty experiment), studying proton-proton collisions, will instead focus on events containing beauty quarks, to extract information regarding CP violation. The experiment will be equipped with a vertex detector, two RICHs (Ring Imaging CHerenkov), a particle tracking system, hadronic and electromagnetic calorimeters and muon spectrometers.

ALICE (A Large Ion Collider Experiment) will be devoted to heavy ion physics; its main purpose is to study strong interactions at unprecedented energies, conditions in which the formation of a new phase of matter, the quark-gluon plasma, is foreseen. The existence of such a phase of matter and the study of its properties are crucial for understanding many aspects of QCD, as quark confinement.

The main constraint for the LHC design is posed by the necessity to reuse the tunnel that contained the main LEP accelerator. This choice, though greatly lowering the construction costs and time scale, requires on the other side a significant effort in the field of superconducting magnets. Infact, given the 3100 m accelerator radius, in order to accelerate a proton beam up to 7 TeV, the bending magnets have to provide a 8.33 T field, very close to the

Center-of-mass energy	7 TeV
Dipole bending field (at 7 TeV)	8.33 T
Luminosity	10^{34} cm^{-2} s^{-1}
Current	0.582 A
Spatial bunch spacing	7.48 m
Time bunch spacing	24.95 ns
Number of particles per bunch	$1.15 \cdot 10^{11}$
Beam crossing angle	285 μrad
High luminosity lifetime	13.9 h
Energy loss per turn	7 keV
Beam spacing	194 mm

Table 1.4: Nominal design performance for the LHC accelerator.

PROTONS		HEAVY IONS	
Accelerator	Energy	Accelerator	Energy
RFQ	750 keV	RFQ	
Linac 2	50 MeV	Linac 3	4.2 MeV/u
PS Booster	1.4 GeV	LEIR	14.8 MeV/u
PS	25 GeV	PS	4.25 GeV/u
SPS	450 GeV	SPS	177 GeV/u
LHC	7 TeV	LHC	2.8 TeV/u

Table 1.5: Injection chain at LHC.

limit of today technology. In table 1.4 the main LHC characteristics are briefly summarized. Another distinguishing feature of the LHC superconducting magnet system is that of being able to accelerate two proton beams in opposite directions at the same time. This necessitated equipping the magnets with two different cavities, each for accelerating one beam, as shown in figure 1.5, where a dipole transverse section is shown.
The beam trajectories will cross with an angle of about 300 μrad in the four sites where experiments are installed.
At all the big accelerator machines, a number of smaller supporting accelerators are used as injectors. In the LHC case some machines already operating at CERN are used; in table 1.5 the protons and heavy ions acceleration chain is summarized and for each machine the maximum beam energy is reported.

Chapter 2

The ATLAS Experiment

2.1 General description

As mentioned in chapter 1, the ATLAS (A Toroidal Lhc ApparatuS) experiment will operate at the LHC and will be devoted to the study of interactions produced in the collision of two proton beams. ATLAS is a multipurpose experiment, designed to achieve the highest possible flexibility in different sectors of high energy physics. Even if a wide physics programme has already been planned, it is possible that unexpected phenomena will show up, requiring the study of unforeseen channels. Its main design requirement is thus to be capability of performing precise measurements not only on expected physical event topologies but also on possible new phenomena.
To achieve this goal, the detector design has to avoid biases from the physical programme and from theoretical expectations; it must be then capable of good identification and kinematical measurement of all the stable particles that can be produced in pp collisions at the LHC. In particular, the ATLAS detector has to fulfill the following requirements [32]:

- excellent electromagnetic calorimeter precision, to identify and measure electrons and photons; high hermeticity hadronic calorimeters, to provide accurate measurement of jets from quark hadronization and of missing transverse energy;
- muon identification and precise measurement of their momentum, granting accurate measurements even at maximum LHC luminosity, using only the external muon spectrometer;
- efficient track reconstruction at high luminosity, to measure leptons with high transverse momentum (p_T), and to identify electrons, photons, τ leptons and heavy quark hadrons; at low luminosity complete event reconstruction is required;
- high pseudorapidity (η) acceptance, with almost complete coverage of the azimuthal angle (ϕ) over the entire detector. The azimuthal angle is measured around the beam axis (Z axis), while pseudorapidity is related to the polar angle (θ), measured starting from beam direction, by $\eta = -\ln\left[\tan\left(\frac{\theta}{2}\right)\right]$. This variable usually replaces θ, since the hadronic cross section is flat in η;

- first level trigger using the lowest possible p_T thresholds, to grant high efficiency for the interesting physical processes accessible at LHC.

The ATLAS detector can be subdivided, moving from the inside out, into three main parts: the Inner Detector, designed to precisely reconstruct tracks from charged particles and to measure their momentum; the electromagnetic and hadronic calorimeters; the muon spectrometer. A fundamental role is also played by the superconducting magnet systems, which provides the field bending the trajectories of charged particles. In the next paragraphs all of these parts will be briefly described, along with the data acquisition and trigger systems.

2.2 The magnet system

The superconducting magnet system is comprised of two parts; a central solenoid, providing the field for the Inner Detector; a set of three big toroids, placed around the central solenoid and at both ends of the detector, generating the field for the muon spectrometer. The solenoid magnet provides an average 2 T field, with a maximum of 2.6 T near the magnet itself; the central and the two side toroids produce 3.9 and 4.1 T fields respectively. The toroids are powered by a 21 kA generator and the solenoid by an 8 kA one, while the cooling is indirectly provided by a forced 4.5 K helium flux.

2.3 Inner Detector

The Inner Detector [33] (ID in the following) has the role of efficiently reconstructing the tracks and vertices contained in each event, contributing, along with the calorimeters and the muon spectrometer, to the identification of electrons, photons and muons; it is also fundamental in order to gather information about the decay vertices of short-lived particles. The accuracy requirements on vertices and on particle momentum, measured through the bending in the solenoidal magnetic field, can only be met employing detectors with high spatial precision; these must also be characterized by high granularity, given the track density foreseen during LHC operation. To this purpose, the Inner Detector, completely enclosed within the central solenoid magnet, is composed of high resolution detectors placed near the beam line and of continuous trackers placed in the outer volume.

2.3.1 Pixel detector

The Silicon pixel sensor technology is well adapted to the innermost region of the Inner Detector, since this is the optimum solution granting efficient track reconstruction near the primary interaction vertex, where the maximum particle flux is produced.
In particular, the ATLAS pixel detector employs 50×400 μm^2 sensor elements. It is structured as a set of three cylinders (the barrel), having their axes on the beam line and a mean radius of 5.05, 8.75 and 12.25 cm respectively, and two sets of three discs (the endcaps), having a mean radius of 17 cm and placed at both ends of the barrel to complete the pseudorapidity coverage. In this way, at least three precise space points are measured by the pixel detectors for each track, enabling the reconstruction of a track segment independently from

other detectors. The barrel cylinders and endcap disks are covered by with a total of more than 1700 modules, i.e. the basic detector elements repeating identically in every detector part. Each module, covering a 6.28×2.2 cm^2 surface, contains a 328×144 pixel matrix.
Due to budgetry reasons, the staging of part of the ATLAS detector was proposed in the past; nowadays this solution has been discarded, anyway it is worth mentioning, since it will be studied in chapter 7. In particular, the staged scenario foresaw to start operation without the intermediate pixel layers in both the barrel and the endcaps; these would have the been inserted during the long shutdown that should follow the first physics run.
The main purpose of the pixel detector is to efficiently reconstruct tracks and vertices at each beam crossing. In particular its role is essential to perform the b-tagging (c-tagging, τ-tagging) selection, separating jets produced by high momentum hadrons containing b quarks (c quarks, τ) from gluon or light quark jets. This selection strongly depends on the precise measurement of the perigee distance (distance of closest approach) between reconstruted tracks and the primary interaction vertex and thus exploits the high spatial resolution granted by the pixel detector.

2.3.2 SemiConductor Tracker

The SemiConductor Tracker (SCT), placed in the intermediate region of the Inner Detector, is designed to measure at least four precise space points for each track; it plays a fundamental role in reconstructing particle trajectories, in measuring their parameters and in the identification of primary and secondary vertices.
The SCT barrel consists of four double layers of Silicon microstrip detectors to measure both the position along the beam line, i.e. the z coordinate, and in the orthogonal plane, i.e. the r and ϕ coordinates. Each wafer covers a 6.36×6.40 cm^2 area and contains 768 strips, each 80 μm wide. Two wafers are bonded end to end to make a detector 12 cm long. Unlike the pixel sensors, the SCT microstrips do not provide an intrinsically three dimensional position measurement. This capability is provided using a stereoscopic geometry, grouping into pairs the detector planes in such a way that the strips from one layer form a 40 mrad angle with those contained in the other one. The strips in one layer are parallel to the beam-pipe in order to give a precise ϕ measurement. In this way the spatial resolution obtained is 16 μm in $r\phi$ and 580 μm in z.
As in the pixel detector, discs are placed in the endcap regions in order to increase the geometrical acceptance; the modules used in the endcaps are similar to the barrel ones, but are trapesoid in shape with radial strips, rotated by 40mRad in the stereo layer.

2.3.3 Transition Radiation Tracker

The Transition Radiation Tracker (TRT) uses straw tube detectors, well adapted to the difficult LHC environment, given their good radiation tolerance. Its geometry is designed in order to provide typically about 36 spatial points for each charged track passing through its volume.
The barrel, covering the radial region between 56 and 107 cm, contains ~ 50000 tubes orientated parallel to the beampipe, each divided in two parts in order to reduce the occupancy

of the readout electronics. The endcaps contains 320000 tubes aligned along the radial direction; in this case the output signals are sampled from the outermost side only.
Each tube is 4 mm wide and contains a sense wire with a diameter of 30 μm; each channel, exploiting the drift time measurement provides a 170 μm resolution on the radial coordinate and two independent thresholds. The higher threshold is used to measure the transition radiation (TR), providing separation between pions and electrons; the emission of TR photons is a threshold effect which depends on the relativistic velocity p/m. Rejection against charged pions is then achieved by counting the fraction of TRT straws which have a high threshold (TR) hit. The rejection power is maximal for p_T around 2-5 GeV, while, at higher energies, the relativistic rise in dE/dx causes the pions to deposit more energy resulting in reduced separation.
The possible staging of the ATLAS detector could affect also the TRT; in particular, in the staged scenario, data taking operation would start without the endcap wheels.

2.4 Calorimeters

The calorimeters, unlike other detectors such as the magnetic spectrometers, increase their intrinsic resolution as the measured energy grows. They are thus particularly suitable for very high energy physics applications and, in the LHC experiments, they will play a crucial role in the reconstruction of the most interesting physical channels.
The main tasks of the ATLAS calorimetry system are: precise measurement of energy, position and shower shape for electrons, photons and jets; estimation of the missing transverse momentum; particle identification, separating electrons and photons from hadrons and jets, and hadronic τ decays from background jets; event selection for triggering purpose.
These goals are particularly difficult to achieve, given the characteristics of the LHC environment. The high center-of-mass energy requires a good and stable performance for energies ranging from few GeV to more than one TeV. Furthermore, since at design luminosity more that twenty proton-proton collisions will occur every 25 ns, the calorimeters have to grant both a fast response and a fine granularity. Finally, to cope with the enormous particle flux expected during more than ten years of operation, a good radiation tolerance is mandatory.
The ATLAS calorimetry system surrounds the Inner Detector and is in its turn enclosed inside the muon spectrometer. This system comprises liquid argon (LAr) calorimeters [34], contributing both to electromagnetic and hadronic measurements, and a larger tile hadronic calorimeter [35], based on scintillating plates and placed in the outer endcap regions. Furthermore, a LAr presampling plane is placed in contact with the cryostat used by the magnet providing the solenoidal field for the Inner Detector; it can be used to measure showers that start in the magnet and in the cryostat. The design energy resolution can be written as a function of the energy E (given in GeV); it corresponds to $10\%/\sqrt{E} \oplus 0.7\%$ for the electromagnetic calorimeter, to $50\%/\sqrt{E} \oplus 3\%$ for the barrel hadronic calorimeter and to $100\%/\sqrt{E} \oplus 10\%$ for the endcap hadronic calorimeter.

2.5 The muon system

A reliable and precise measurement of muon momentum is crucial for the study of the phenomena that will occur at LHC. The range of muon energies for which a good precision is required goes from a few GeV, e.g. for events containing b-quark hadrons, up to the TeV scale, where interesting new processes could appear.
To this purpose ATLAS is equipped with a muon spectrometer [36] based on the magnetic trajectory bending provided by the three toroidal superconducting magnets. The correct working conditions are also granted by the particle filtering performed by the hadronic and electromagnetic calorimeters. As a matter of fact only muons with a momentum exceeding 3 GeV can reach the muon spectrometer by passing through the calorimeters.
In order to enhance the momentum resolution in the region below 100 GeV, tracks reconstructed in the muon spectrometer can be extrapolated back to the Inner Detector volume and thus matched with the one reconstructed in the tracking detectors. Two different procedures can be used to perform this track matching; one is based on a statistical combination of the two independent track parameters measurements; the other one performs a global fit on both the Inner Detector and the muon spectrometer spatial measurements. In both cases a resolution below 2% for $p_T < 100$ GeV and around 10% for $p_T \sim 1$ TeV can be achieved. Furthermore, the matching between tracks reconstructed by different detectors enhances the rejection power against muons produces by secondary interactions as well as those coming from the "in-flight" decays of π and K mesons.
Finally, the muon spectrometer plays a crucial role in the trigger selection. In order to be able to produce a fast decision signal it is equipped with detector elements less precise but faster than those used for track reconstruction and momentum measurements.

2.6 Data acquisition

Given the requirements presented by the LHC environment, the trigger and data acquisition (TDAQ) system is one of the most crucial parts of the ATLAS experiment [37].
In this and in the next section, some of the principal components and functions of the TDAQ system are briefly described; a schematic diagram showing the interplay between different parts of the TDAQ chain is given in figure 2.1. The data-taking process can be broken down into four principal systems, namely:

- the Data Flow (DF) system, taking care of receiving data from the different detectors, making it available in the trigger infrastructure, and providing the interface to save the selected events to mass storage;

- the Trigger system, responsible for the event selection and filtering, leading to a rate reduction of a factor of $\sim 2 \cdot 10^5$, and for the classification of the accepted events;

- the Online system, coordinating the different aspects of data-taking operation during both physics and calibration runs;

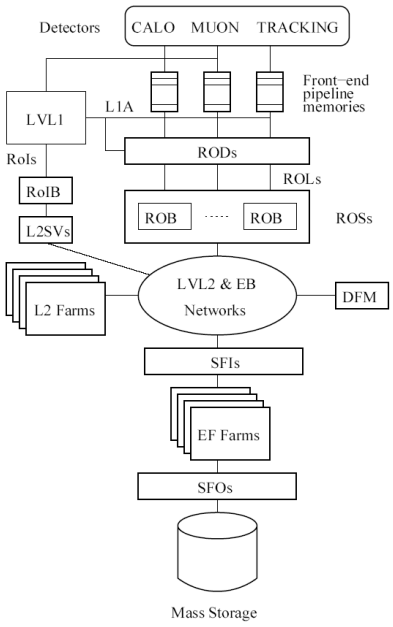

Figure 2.1: Principal components of the Data Flow and Trigger systems.

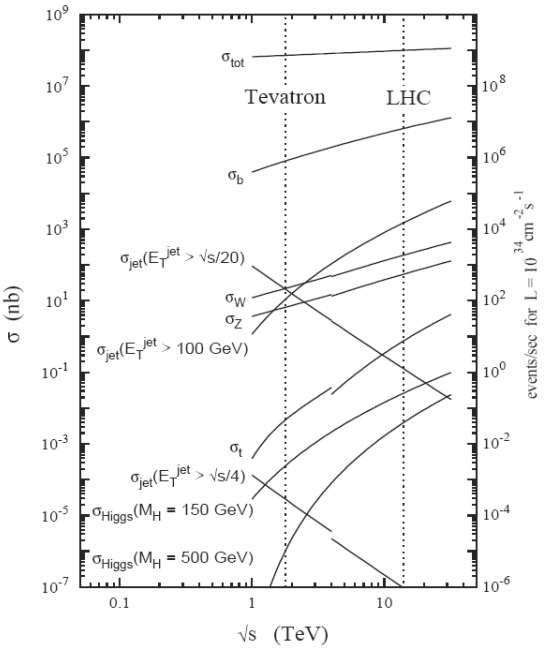

Figure 2.2: Energy dependence of some characteristic proton-antiproton cross sections at the LHC and at the Tevatron.

- The Detector Control System (DCS), responsible for the so-called slow controls, granting coherent and safe operation of the ATLAS detector, it also provides the interface with external systems and services, including the LHC itself.

2.6.1 Detector specific readout

In the ATLAS experiment, the boundary between the detector readout and the common data acquisition path is placed at the output of the Read Out Drivers (RODs).
These are VME boards, developed by the subdetector communities, taking care of all the detector specific features; as an example they provide the interface with the front-end electronics and handle the different data format conversions for each subsystem. Every time an event is accepted by the first level trigger, the corresponding data is transferred from the detector pipeline memories into the ROD; this then performs the necessary operations on the data and sends the it to the common DAQ infrastructure, described in the next subsection. Since they provide the only way of interfacing with the on-detector electronics, the RODs play a crucial role in the configuration of the detectors. Finally, in some cases, as for the pixel system, the detector calibration procedures heavily rely on the RODs.

2.6.2 Common readout components

The common data acquisition chain starts at the input of the Read Out Buffers (ROBs), receiving data output by the different RODs. In particular, data fragments of events accepted by the first level trigger selection are transferred from the detectors RODs to the ROBs through over 1600 point-to-point readout links (ROLs), for which the agreed ATLAS standard foresees a maximum bandwidth of 160 MByte/s.
The ROBs are then grouped into several Read Out Subsystems (ROSes); these exploit the ROBs in order to provide temporary buffering of the ROD event fragments for the duration of the second level trigger decision. Furthermore, the ROS handles the data requests issued by the trigger system and the subsequent elements of the data flow.
Event data fragments for the events selected by the second level trigger are then built into complete events by the Sub-Farm Interfaces (SFIs). These make the entire events available for the last selection stage, the Event Filter. The events passing this last selection are then moved to permanent storage via the final element of the DF system, the Sub-Farm Output (SFO).

2.6.3 Online system operation

The Online software system manages the configuration, control and monitoring of the entire TDAQ system. It has to coordinate the operation of the various sub-systems, providing, at the same time, the interface between the human users and the TDAQ system.
Furthermore, it has the roles of guiding the TDAQ through its start-up and shutdown procedures, so that they are performed in an orderly manner, and of keeping the synchronization of the states of a run in the entire TDAQ system.

2.7 The trigger system

At LHC design luminosity, $\sim 23\,pp$ interactions will occur at every bunch crossing, i.e. every 25 ns; at the same time, the high number of detector channels, $\mathcal{O}(10^8)$ in total, leads to an average event size of $\sim$ 1.5 MB. These two factors pose stringent design demands on both the detectors and the data acquisition system and limit the final event storage rate to a maximum value of $\sim$ 200 Hz. Furthermore, as depicted in figure 2.2, background QCD events have a much higher cross-section than the rare collisions of particular interest to the ATLAS physics programme.
This means that the trigger system must be capable of efficiently selecting the valuable events, gathering and permanently saving the corresponding data from the different detectors; this way they will be available to perform offline studies.
The trigger strategy adopted by the ATLAS experiment foresees three different selection steps, as depicted in figure 2.1:

- first level trigger (LVL1): this stage receives input data at a 40 MHz frequency and aims at reducing it to a maximum of 75 kHz upgradable to a maximum of 100 kHz. The LVL1 selection is based on the information coming from the calorimeters and the

muon trigger chambers and has to act within a fixed latency of 2.5 μs; as a consequence, this stage uses simple algorithms, implemented on custom hardware processors;

- second level trigger (LVL2): the events passing the LVL1 are then filtered by a second decision level, based on software selections, running on commercial processor farms and reducing the rate to ~ 2 kHz. This stage, seeded by the results obtained at LVL1, can access full granularity information from all the subdetectors. Data is processed in parallel inside one or more geometrical regions identified at LVL1, the so called Regions of Interest (RoI), each corresponding, on average, to the 2% of the total event. The algorithms used are more sophisticated than those available at LVL1; and they must be optimized for speed, since the LVL2 decision must be taken within an average processing time of 10 ms;

- event filter (EF): this final software selection level has much looser time constraints, around 1 s. It can be seeded, in its turn, by the LVL2 results, or the whole event can be analyzed, as an example for the missing transverse energy triggers. More complex reconstruction strategies, including bremsstrahlung and converted photons recovery, can be executed at this stage.

The choice of having two different software selection levels, collectively referenced as High Level Trigger (HLT), though increasing the complexity of the system, has the effect of significantly reducing the network bandwidth needs and of improving the flexibility of the event selection scheme.
In the following sections a more precise description of the first level trigger is given (while more details on the HLT can be found in the next chapter), along with an overview of the ATLAS trigger menu mechanism.

2.7.1 First Level Trigger

The LVL1 trigger has the task of performing a first quick selection of the interesting events. This is accomplished using information from the calorimeters and muon trigger detectors, the Resistive-Plate Chambers (RPC) and the Thin-Gap Chambers (TGC).
The LVL1 trigger can be subdivided in three parts: the calorimetry trigger, retrieving data from the calorimeters and manipulating it for the trigger decision; the muon trigger, doing the same with muon chambers data; and the event decision part, implemented in the Central Trigger Processor (CTP).
The ingredient used to build the trigger decision is the multiplicity of the physical objects detected in the calorimeters and in the muon spectrometer, once criteria such as a given p_T or E_T threshold is applied. The calorimeter cuts can also include EM and hadronic isolation. As far as the calorimeters are concerned, these objects can be electrons/photons, τ leptons/hadrons and jets; triggers based on the total transverse energy (E_T) and of the missing transverse energy (E_{Tmiss}) are also available.
As said before, the LVL1 trigger acts within a fixed 2.5 μs latency, taking into account also the time needed to transmit the electrical signals from the detectors to the trigger logic. During this latency, data has to be temporarily stored inside all the subdetectors, using

built-in pipeline memories. If a particular event is accepted by the LVL1, the corresponding data is moved from the detectors into the ROBs and thus made available for LVL2 and EF processing.
For every selected event, a set of Regions of Interest (RoI) is identified, each built around one of the interesting physical objects; this geometrical information is then used at LVL2 in order to reduce the amount of processed data.

2.7.2 Event selection strategy

The ATLAS trigger system aims at reaching the highest possible efficiency for selecting new physics channels, while retaining a good rejection power against background events. Furthermore, since it is currently impossible to have a completely reliable prediction for the physics scenario and for the background conditions at LHC energies, the trigger design must be flexible enough to enable the switching between different schemes depending on what will be observed once LHC starts its operation. Following this idea, a set of trigger schemes covering different physical aspects has been prepared:

- single and double lepton inclusive triggers: these will cover great part of the ATLAS physics programme, as explained in more detail in chapter 5. Examples of significant physical processes identified by this trigger are the associated Higgs boson production (e.g. $t\bar{t}H$, $H \to ZZ \to 4l$), t-quark physics, $z \to l\bar{l}$ decays used for detector calibration studies, $W \to l\nu$ decays;

- jet triggers: multiplicities between one and four jets are foreseen; the thresholds range, at the HLT level, from $\sim$ 400 GeV for single jets down to the 100 GeV of the four jet trigger; in addition this scheme can also be used to trigger jets traveling in a direction close to the proton beam. The main physical applications of this trigger are QCD studies and the determination of the background for other interesting channels; but they can also be used for discovery studies, selecting new physics signatures such as new resonances or R-parity violating events;

- total and missing tranverse energy triggers: these are crucial for new physics studies, e.g. to tag invisible decays and to identify supersymmetry signatures. The missing transverse energy threshold will be set to values around 150 GeV, while the total transverse energy trigger plays an important role at about 1 TeV;

- mixed triggers: in these selections, as an example, lepton and jet triggers are combined with missing E_T;

- other triggers: apart from the main trigger items described above, a number of more specific ones will be available; these will be used, as an example, in the B hadron physics sector, described in more detail in chapter 8, for calibration purposes and detector efficiency studies.

The thresholds for the different trigger selections are obtained from studies based on Monte-carlo simulation and try to reach the best possible trade-off between selection efficiency and

rate reduction. It should be noted that the description of both the ATLAS detector response and of the physics processes used in the simulations could differ significantly from what will be observed during real operation; this means that, most probably, as soon as more precise theoretical predictions and better detector simulations will be available, some thresholds will have to be partially tuned to new values.

Signature (LVL1)	**Rate (LVL1, kHz)**	**Signature (HLT)**	**Rate (HLT, Hz)**	**Purpose**
MU20	0.8	$\mu 20i$	40	$t\bar{t}H, H \to WW, ZZ$, top, $W', Z', Z \to ll$
2MU6	0.2	$2\mu 10, 2\mu 6$+mass	10, 10	$H \to WW, ZZ$, $B, Z \to ll$
EM25i	12	$e25i, \gamma 60i$	40, 25	$t\bar{t}H, H \to WW, \gamma\gamma$ top, $W', Z', Z \to ll$, $W \to \nu l$
2EM15i	4	$2e15i, 2\gamma 20i$	<1, 2	$H \to WW, ZZ, \gamma\gamma$ $Z \to ll$
J200	0.2	$j400$	10	QCD, new physics
3J90	0.2	$3j165$	10	QCD, new physics
4J65	0.2	$4j110$	10	QCD, new physics
J60 + xE60	0.4	$j70$ + xE70	20	Supersymmetry
MU10 + EM15i	0.1	$\mu 10 + e15i$	1	$H \to WW, ZZ$ fully leptonic $t\bar{t}$

Table 2.1: Trigger rate estimates for the most significant signatures. The LVL1 and HLT values are given for the low luminosity scenario. The signature names are structured as "NoXXi", where N represents the minimum number of required objects, "o" is the object type (electron, photon, jet...), "XX" is the E_T threshold (in GeV) and "i" tells whether isolation is required. In particular, EM, MU, and J respectively identify a LVL1 electron/photon, muon or jet; xE corresponds to the missing transverse energy selection (both for the LVL1 and the HLT); e, γ, μ and j identify electron, photon, muon and jet trigger objects at the HLT. The threshold for the 2MU6 signature hasn't been decided yet. The term "mass" in the $2\mu 6$ signature corresponds to the fact that a cut on the invariant mass of the two muons can be applied, e.g. requiring that it matches the J/Ψ mass.

Table 2.1 [39], [38], [40] gives an estimate of the rates expected for the most important signatures at initial luminosity (2×10^{33} cm^{-2} s^{-1}). The total rates for the LVL1 trigger and the HLT are respectively 25 kHz and 200 Hz. Since the LVL1 is designed to cope with rates up to 75 kHz, it will be possible to add new signatures, e.g. those used for B physics studies; but it must be taken into account that the evaluated rates could be affected by errors corresponding to a factor of two, corresponding to the uncertainties on Montecarlo predictions.
The trigger menu thresholds can be adapted to the experiment's operating conditions, such

as luminosity drops w.r.t. the peak value, changes in the LHC background or in the detector performance, and to the physics programme. As an example, for lower luminosity runs, in order to fully exploit the trigger system bandwidth and the HLT processing power, the selection criteria could be modified in order to keep the HLT rate constant. This could be done lowering some thresholds or adding new signatures, as explained, as an example, in the B-physics chapter.

2.8 Physics programme

The energy and luminosity of the LHC will give the opportunity of performing a great variety of physical studies. ATLAS will aim at testing the SM predictions and at precisely measuring the properties of already known objects, such as the gauge bosons, while, on the other hand, searching evidence for new physical phenomena foreseen by SM extensions.
The first kind of studies will mainly exploit the initial reduced luminosity phase. The search for possible new phenomena, requiring the highest possible statistics, will be instead carried on during the period in which LHC will operate at its design luminosity.

2.8.1 Running at initial luminosity

In the initial LHC operation phase, large samples of gauge bosons will be available and many QCD and heavy flavour processes will be accessible. This will give the opportunity to perform precise measurements exploiting the better signal to background ratio with respect to the one obtained at design luminosity.
The QCD studies will focus on two main aspects; first of all, since QCD processes will provide the dominant background for discovery signals, a precise knowledge of their properties in the unexplored LHC kinematical region will be sought. Furthermore the current QCD predictions will be tested with precision measurements, e.g. providing strong constraints on parton distributions inside the proton. Finally, observations deviating from theoretical QCD predictions could also point out the presence of new physical phenomena.
Moving to the flavour physics sector, LHC collisions will produce, even in the reduced luminosity regime, very large samples of hadrons containing b-quarks (B hadrons), due to the high hadronic cross-section for $b\bar{b}$ production. In particular, about one collision out of one hundred will produce a couple of b-quarks; thus the statistics for these kinds of samples will be limited only by the trigger rate. Hence the B-physics programme has to be selective, and in general it will concentrate on CP violation, precision measurements of flavour oscillations and decay frequencies for B_s^0 and B_d^0 mesons and rare decays. Both these topics will provide additional constraints on the elements of the CKM matrix, as described in more detail in chapter 8. Furthermore, ATLAS will look for decays strongly suppressed in the SM; these, if observed at frequencies significantly higher than the expected ones, would provide indirect evidence of new physical scenarios.
Theoretical predictions also foresee that, operating at reduced luminosity, more than eight million $t\bar{t}$ pairs will be produced every year. This, along with the good signal to background ratio, will provide the ideal condition for studies on t-quark properties. There are many physical motivations for these studies; first of all the t-quark is the only known fundamental

fermion having a mass of the order of the electroweak scale and, thus, the study of its properties is an excellent probe for the electroweak symmetry breaking mechanism; new physical phenomena may then be discovered by studying both its production and its decays; in addition to this, the t-quark mass measurement provides indirect constraints on the SM Higgs boson mass; finally, events containing t-quarks will greatly contribute to the background for many interesting channels and so have to be accurately studied, in order to refine the selections used in these other analyses.
Another important goal, during the first ATLAS operating stages, will be that of measuring the W boson mass with a precision below 15 MeV. Thanks to the 300 millions single W events that will be stored in one year of operation, the statistical error will be around 2 MeV; so, to obtain the desired precision, the systematic error has to be kept below 10 MeV. In case both the W and t-quark masses will be measured within the design resolutions, ATLAS will be able to indirectly constrain the SM Higgs mass or the MSSM h mass with a precision below 30%.

2.8.2 Operation at design luminosity

In case the Higgs boson will not be discovered before LHC start-up, the searches for it or its possible supersymmetrical extensions will be the main focus of the ATLAS experiment. The search strategies will exploit different decay channels, whose choice is guided by the signal frequency and by the signal to background ratio in the various mass regions.
Figure 2.3 shows the SM Higgs discovery sensitivity for the ATLAS experiment in the intermediate mass region; different curves are drawn for the integrated luminosity values achievable at reduced and design luminosity. The main channels used to search for the Standard Model Higgs boson are:

- $H \to \gamma\gamma$ from direct production;
- $H \to \gamma\gamma$ from associated production channels WH, ZH and $t\bar{t}H$, selected by a lepton (e, μ) coming from the vector boson or t-quark decay;
- $H \to b\bar{b}$ from associated production channels WH, ZH and $t\bar{t}H$, selected by a lepton (e, μ) and by b-tagging techniques;
- $H \to ZZ^* \to 4l$;
- $H \to ZZ \to 4l$ and $H \to ZZ \to ll\nu\nu$;
- $H \to WW \to l\nu jj$ and $H \to ZZ \to lljj$.

The analysis of the Higgs sector is even more complicated in the MSSM scenario, given the number of possible signals. That theory foresees five different physical particles related to the spontaneous symmetry breaking mechanism; two of them are charged ($H^{\pm}$) and three are neutral (h, H, A). In the semi-classical approximation, the masses and couplings of these particles can be described in terms of two parameters, usually m_A, the mass of the CP-odd boson, and $\tan\beta$, the ratio between the vacuum expectation values of the two Higgs doublets. The results obtained in this scheme, even if substantially modified by radiative corrections,

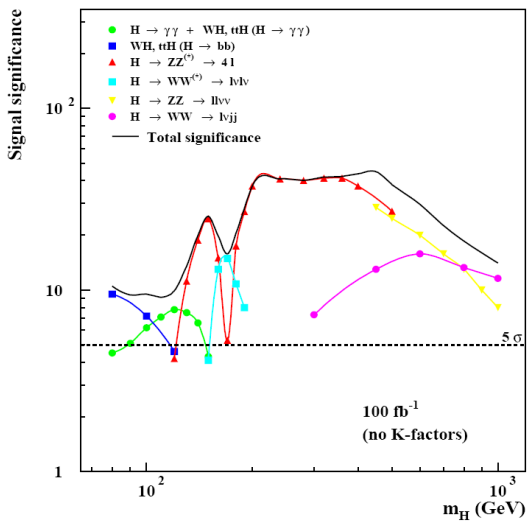

Figure 2.3: ATLAS sensitivity for SM Higgs boson discovery in the intermediate mass region; the sensitivity of each analyzed channel is reported, along with the overall one. Results are given for one year of operation at design luminosity.

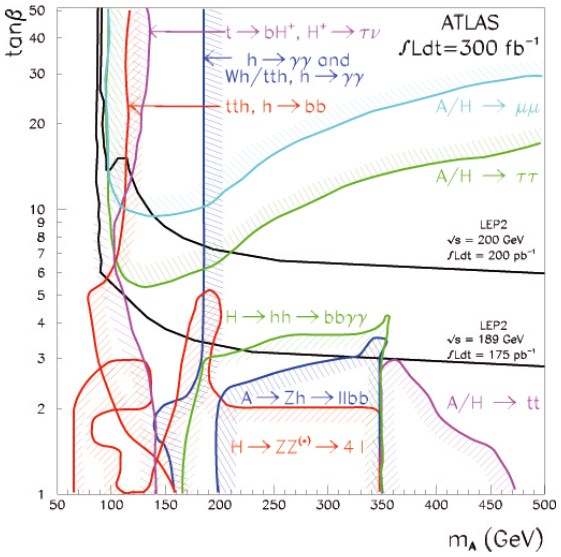

Figure 2.4: ATLAS sensitivity for MSSM Higgs boson discovery; the boundary of the 5σ region for each channel is shown in the (m_A, $\tan\beta$) plane. The regions ruled out by LEP experiments are also drawn.

can anyway provide strong hints for the experimental searches. In case SUSY particles would be too heavy to be produced in Higgs boson decays, the most relevant channels would be the same described for the SM case. On the other hand, if SUSY particles could be produced in Higgs decays, the SM channels would be strongly suppressed. The ATLAS sensitivity for MSSM Higgs bosons discovery is depicted in figure 2.4, as a function of the m_A and $\tan\beta$ parameters.

Finally, the discovery of particles foreseen by supersymmetrical theories should be relatively easy if these have masses lower or close to 1 TeV. The ATLAS experiment aims not only at providing evidence for their existence, but also at gaining insight on their fundamental nature through precision measurements of their properties; this would also provide a good experimental ground against which the different SUSY models could be tested.

Chapter 3

The ATLAS High Level Trigger

3.1 Introduction

As mentioned in chapter 2 the ATLAS software trigger selection, the High Level Trigger, is subdivided in two different layers, the LVL2 and EF [37].
Both of them, unlike the LVL1 trigger, are implemented uniquely using software algorithms, running on commercial processor farms. The HLT trigger selection chain is depicted in figure 3.1.

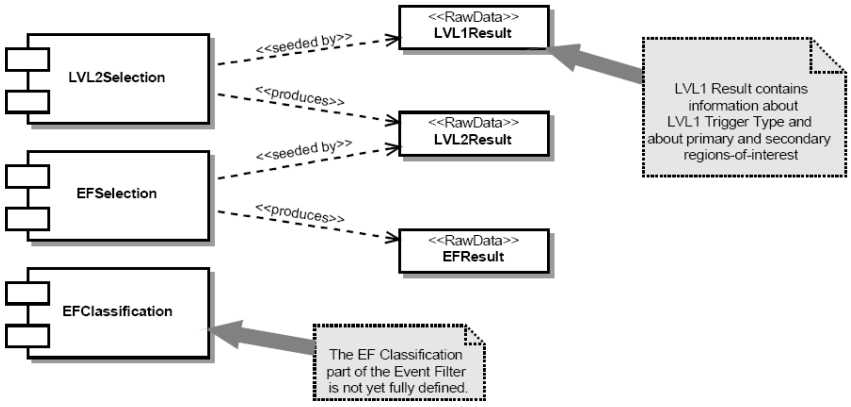

Figure 3.1: The HLT selection chain.

The RoI information obtained at LVL1 is passed to the LVL2, which uses them as seeds, i.e. as a starting point to initiate the reconstruction process. On its turn, the LVL2 produces an output result which can be used as a seed for the reconstruction at the EF. Anyway, it is also possible to ignore the LVL2 result and seed the EF directly with LVL1 information; this operational mode proves very useful, as an example, to study and validate the LVL2 selection performance.
As described in chapter 2, data produced in events accepted at LVL1 is sent from each detec-

tor to its corresponding ROSs, each containing several ROB. At the same time, information on the location of RoIs identified by LVL1 is sent to the LVL2 supervisor, to guide the LVL2 event selection. Figure 3.2 shows the exchange of messages that are then used to control the HLT process.

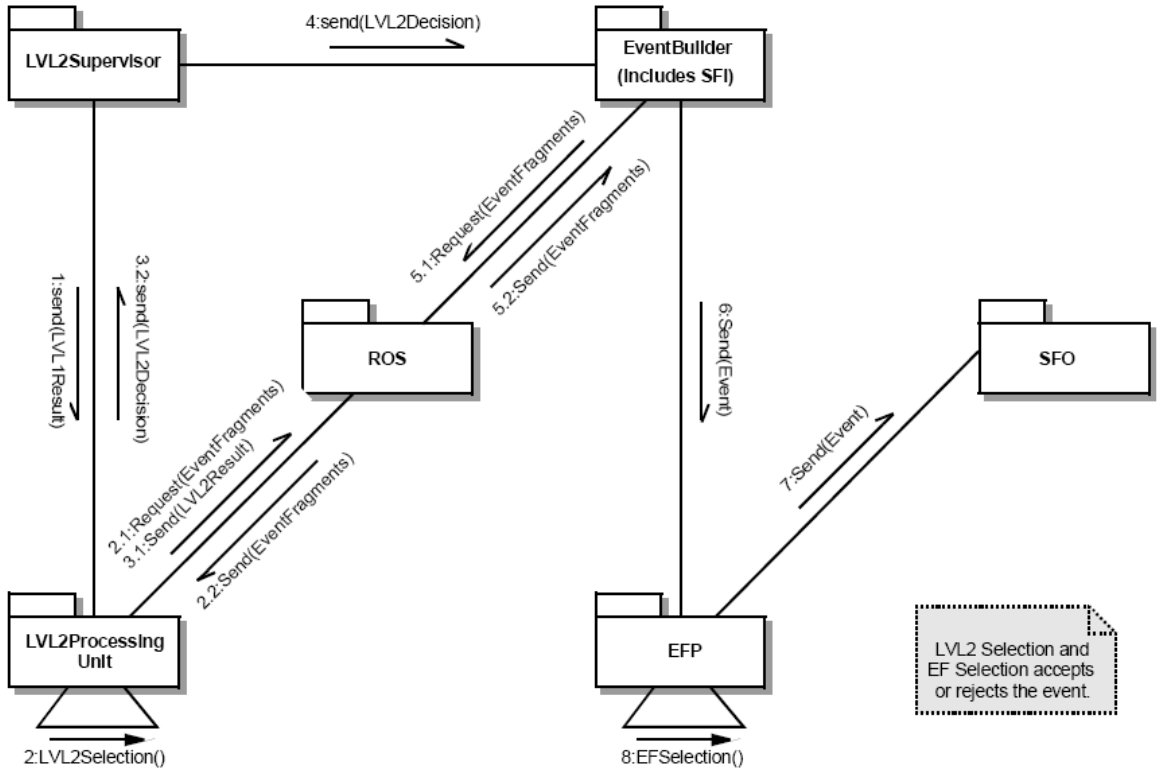

Figure 3.2: Schematic diagram of the HLT messaging infrastructure.

The LVL2 supervisor sends the LVL1 Result to the LVL2 Processing Unit (L2PU), where the LVL2 selection is performed. Using the LVL1 result as guidance, specialized LVL2 algorithms request a sub-set of the event data from the ROSs to perform the event reconstruction. In this way only a few per cent of the event data need to be transferred to the LVL2 system, thus considerably reducing the network bandwidth required. For events accepted by LVL2, details are sent to the ROS (in the LVL2 result) to be included in the event. The L2PU send their LVL2 decisions back to the LVL2 supervisor, which forwards them to the Event Builder, where each accepted event is assembled into a single record, including the LVL2 Result. The entire event is then passed to the Event Filter Processor, where offline quality algorithms are applied, exploiting the information already obtained at LVL1 and LVL2, to further refine the event selection. Events passing the EF are then permanently stored for offline analysis.

3.2 The second level trigger

The second level trigger is guided, in his event selection, by the RoIs produced at LVL1 and uses the information they provide as a starting point to validate LVL1 decisions. The software components involved in the LVL2 selection process are:

- the RoI Builder (RoIB): combines the information coming from the LVL1 RoIs and sends it to the LVL2 supervisor;
- the LVL2 Supervisor (L2SV): selects a LVL2 processor, feeds it with LVL1 information and then waits for a decision for the corresponding event, the so-called LVL2 decision;
- the LVL2 Processors (L2P): these are a processors farm executing the Event Selection Software (ESS); they request the event data to the ROSs, process it and output a LVL2 decision.

The event selection is accomplished in more subsequent steps, the first of which is to the validation of the LVL1 RoI, used as an input for LVL2 reconstruction; this is done using full granularity data coming from the muon chambers and from the calorimeters. In the following steps, data from all the other detectors is used.
Another feature peculiar to the event selection strategy is the early rejection, achieved through event processing in alternate steps of event reconstruction and hypothesis testing on the reconstructed quantities; this means that an event can be rejected after any of these steps, if the reconstructed features do not fulfill required criteria or signatures.
For the events passing the LVL2 selection, which will be then moved to the Event Filter, LVL2 processors send more details on the LVL2 selection to the pseudo Read-out System (pROS); this way, the information on the LVL2 result can be then retrieved and used by both the EF and the offline reconstruction software.

3.3 The Event Filter

The functionality of the EF has been logically distributed between two main entities:

- the Event Handler (EH) performs the activities related to event selection. This includes: the data flow, both between the main DAQ system and the EF, and internally between different parts of the EF; the framework to support various tasks, including the Processing Tasks (PT) where the ESS runs;
- the EF Supervisor handles the control operations, in coordination with the overall T/DAQ control system. Its responsibilities include the monitoring of the EF.

The EF has been designed so that additional functions can be added without jeopardizing the selection activity. Examples of such extra activities are the global monitoring of the detectors or tasks related to alignment and calibration.

3.4 HLT selection strategy

The HLT selection strategy is based on two basic criteria:

- the selection process is always seeded by a limited number of RoIs;
- the selection decision is achieved following a step process; after each step, the original hypothesis can be validated or rejected, while the reconstructed features are refined using data coming from different detectors or adopting more complex algorithms.

The main advantage of this approach is that it greatly speeds-up the HLT decision process. As a matter of fact, starting the reconstruction from a few RoIs means significantly reducing the amount of processed data; furthermore, the early rejection of a candidate events, granted by the step processing strategy, minimizes as much as possible their average processing time. Figure 3.3 shows, as an example, the selection scheme for the $2e20i$ signature, requiring a couple of isolated electrons with p_T exceeding 20 GeV.

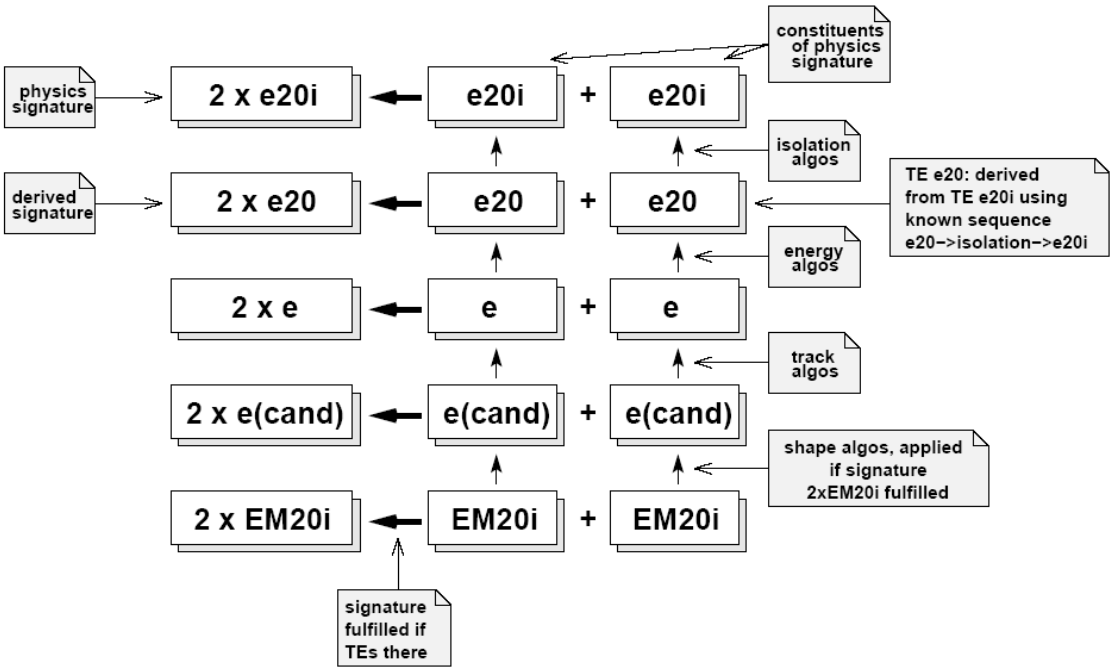

Figure 3.3: Signature validation process; the 2e20i signature, corresponding to the selection of couples of isolated electrons with p_T exceeding 20 GeV, is used as an example.

During the first step, information is gathered from the LVL1 RoIs and the 2LVL1::EM20i signature, requiring two isolated LVL1 signals exceeding 20 GeV in the EM calorimeter, is validated. In case this first selection is passed, more complex algorithms are used to refine the information provided by the RoIs; this analysis must be capable of distinguishing between electromagnetic signals produced by single electrons or photons and signals due to $\pi^0 \to \gamma\gamma$

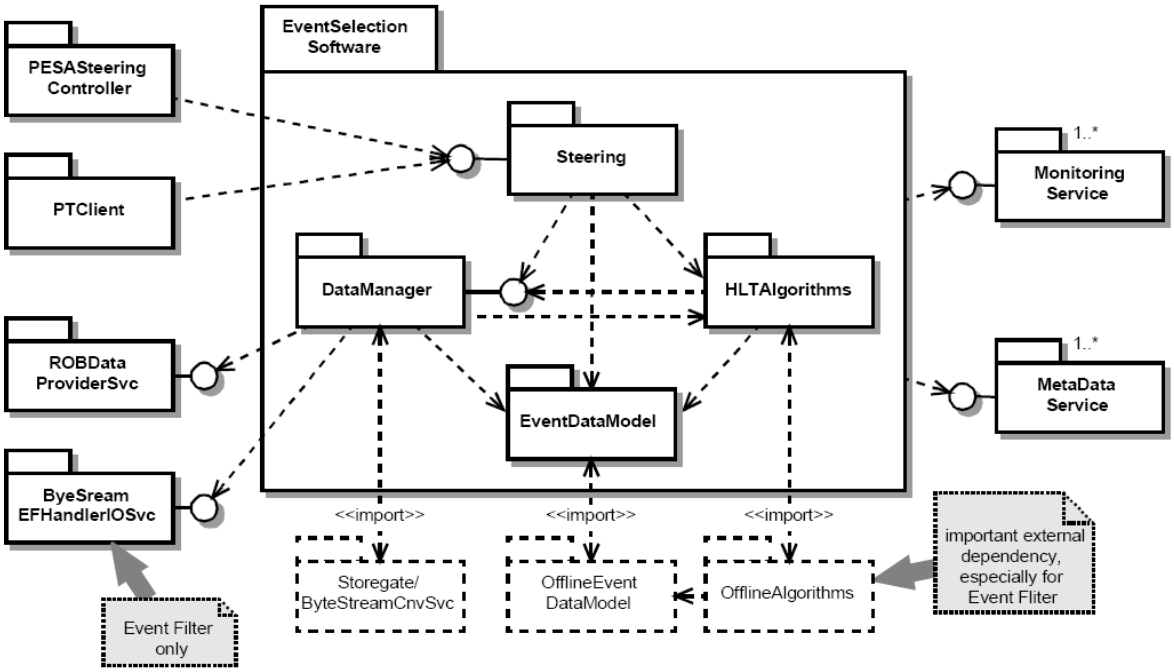

Figure 3.4: The HLT Selection Software scheme.

decays in jets. Data passing this further filter is tagged as an HLT::EM signature; in case two objects of this kind are found in the event, the 2HLT::EM signature is validated and the reconstruction process continues. The following step will then check if the detected signals exceed the selected E_T threshold (20 GeV, in our example) and whether they are isolated enough; in this case the 2HLT::EM20i signature is fulfilled. Finally, tracks are reconstructed in the ID, looking for those matching the calorimeter clusters; if such tracks exist, the EM clusters are identified with electron candidates, the 2HLT::e20i signature is satisfied and the corresponding reconstructed event is selected.

3.5 HLT Selection Software

The decision of accepting or rejecting a particular event is taken by the HLT Selection Software (HLTSSW), executed by the L2PU and by the Event Handler.
The ESS is subdivided into four sub-packages, as listed below; these are shown in figure 3.4, along with their most important external software dependencies:

- the Steering, which controls the selection software; it organizes the HLT algorithm processing in the correct order, so that the required data is produced and the trigger decision is obtained;
- the event data is structured following the Event Data Model (EDM). The EDM covers

all data entities in the event and the relationships between them. The data entities span from the raw data in byte stream format (originating from the detector RODs), the LVL1 Result, and all other reconstruction entities up to the LVL2 and EF Results;

- the HLT Algorithms [41], which are used by the Steering to process the event and to obtain the data on the basis of which the trigger decision is taken;
- the Data Manager, which handles all event data during the trigger processing.

The HLTSSW has been developed inside the ATHENA software framework [42], based on its turn on the Gaudi framework [43], designed to support the offline analysis software.
The strategy of adopting a common framework for both the offline and the on-line reconstruction has many advantages; as an example, it allows a more flexible approach for the reconstruction algorithms. Furthermore, since the offline framework is a common development environment for the entire ATLAS experiment, it grants a larger number of users and developers contributing to the on-line algorithms.
Anyway, at least as far as LVL2 is concerned, the common framework needs a partial customization, in order to meet the processing constraints posed by on-line analysis.

Chapter 4

On-line Track Reconstruction Using Silicon Detectors

4.1 General remarks

In the ATLAS experiment, as in all the experiments carried on at hadronic colliders, track reconstruction is a fundamental ingredient for the selection of many event signatures; anyway, since it relies on the precise spatial measurements (referenced as space points in the following) provided by the Silicon detectors, this selection can only act starting from the LVL2, as LVL1 only uses low granularity data from calorimeters and muon chambers.
In particular, a good tracking performance is required both at the LVL2 and at the EF, in order to cover the following menus:

- identification of high p_T isolated charged particles; this can be done directly, as for electrons and muons, or through the reconstruction of their decays, as for the τ leptons. In order to refine the selection, tracks identified in the ID can be matched to the clusters reconstructed in the outer detectors; this requires a good resolution of the directional parameters of the reconstructed tracks;

- b-jet identification; the purity of the reconstructed sample has to be good down to low p_T values, to avoid feeding the flavour tagging algorithms with fake track candidates. This kind of selection could enable to reduce the LVL1 jet thresholds, playing a particularly important role in scenarios where new physics leads to fully hadronic final states; this is the case of the supersymmetrical Higgs decay channel $H \to hh \to b\bar{b}b\bar{b}$;

- B hadron physics; in this case the reconstruction efficiency must be stable with respect to p_T down to values around $\sim$ 1.5 GeV. This requirement is mandatory for the reconstruction of exclusive ($B \to \pi^+\pi^-$) or semi-inclusive ($J/\Psi \to e^+e^-$, $\mu^+\mu^-$) B hadron decays.

In the LVL2 reconstruction environment, data from the tracking detectors are available, along with full granularity calorimeter and precise muon measurements; furthermore, this is the earliest selection stage where it is possible to combine information from different detectors.

The main limitation is the average event processing time, which has to be kept below 10 ms; anyway, the RoI-based approach, greatly reducing the amount of information to be processed, makes it possible to apply track reconstruction algorithms at LVL2.
In the next sections, SiTrack, a tracking algorithm designed for LVL2 operation, will be described; the results of basic functionality tests based on single track reconstruction will also be given. In the following chapters, the SiTrack algorithm will be then applied to the selection of the different signatures described above; in particular, chapter 5 will cover high p_T isolated electron reconstruction, chapter 6 will focus on the b-tagging selection and chapter 7 will study the application to a decay channel interesting for B-physics studies. All the studies mentioned so far have been carried on using simulated data; next chapter will, instead, report the results obtained operating on data taken in a real on-line environment.

4.2 The SiTrack algorithm

In this section, the SiTrack algorithm is described; SiTrack is a LVL2 track reconstruction algorithm based on Pixel and SCT detectors data and is an improved version of PixTrig [44], originally implemented using only the three Pixel detector layers. Its track reconstruction strategy is based on the selection of space points triplets registered in the Silicon tracking system. The selected triplets are taken as track candidates and an estimate of their parameters is extracted from the equation of the circle connecting the points in the R/Φ plane.
The track seeds, from which the reconstruction of the final track candidates starts, are formed using couples of space points from detector layers close to the interaction region; at the same time the Z position of the primary vertex is reconstructed. The seeds pointing to the primary vertex are then extended using data from outer layers, adding a third space point; the track parameters are finally computed in both Z and R/Φ planes.
These track segments could be, in principle, used as seeds for more sophisticated track finding algorithms; anyway they also can be directly used to apply LVL2 selections, as is done in the following.
The following sections describe in more detail the process of track reconstruction inside SiTrack. The design of the algorithm is modular and so it can be easily decomposed in terms of its component blocks. In particular, next subsection explains the pattern recognition approach adopted for track reconstruction and, in particular, the principle used to group physical detector modules into "logical layers"; the following subsections will, instead, provide a detailed description of the main algorithm blocks and of their tuning procedures.

4.2.1 Pattern recognition approach

SiTrack processing is based on the use of logical layers. A logical layer can be roughly defined as a set of detector modules from different physical layers, playing the same role during track reconstruction.
More precisely, SiTrack logical layers are built examining Montecarlo tracks that produced a space point on the first layer of the pixel barrel (B-layer); their hits are then ordered and numbered with increasing r values and, finally, the modules containing space points with the same number are grouped together. So, as an example, the second logical layer contains

all the modules on which the second space point from at least one Montecarlo track lays. Information on logical layer composition is stored in two separate maps used in the track seeding and extension phases.
Obviously, the above definition implies that the first logical layer exactly corresponds to the B-layer; this choice follows from the fact that the space points it provides are very close to the interaction region and greatly contribute to an accurate track impact parameter evaluation.
This pattern recognition approach grants two main benefits; first of all it enables to reduce the amount of space point combinations analyzed by the algorithm, along with the processing time spent in both the seeding and the extension phases.
In addition, the effect of the parametrical detector inefficiencies introduced in the Montecarlo simulation is automatically taken into account, since the learning phase is based on simulated tracks. This follows from the fact that a logical layer doesn't correspond to a physical layer: as an example, if the second logical layer is selected for the track seeding, a set of modules belonging to the second physical layer, but also, to a lower extent, to the third one will be examined; this way there will is the possibility to reconstruct a good seed even for those tracks whose hit on the second physical layer is lost due to detector inefficiencies.
More realistic effects, such as a complete inefficiency for a limited set of detector modules or the presence of hit losses correlated with the event signatures, could be introduced with the same technique, and their effect on track reconstruction could be evaluated.
The basic robustness of the algorithm can then be further improved, since SiTrack can handle more than one second and third logical layers. Anyhow, in those cases both the processing time and the fraction of fake candidate tracks can increase along with the amount of combinatorial background. So a precise tuning is needed, as will be shown in the following, to increase the algorithm robustness while retaining a good rejection power and a reasonable timing.
Finally, each physical layer can be excluded from the learning phase, so that maps suited for staged geometries can be easily produced, even starting from data sets in which the complete geometry is used.

4.2.2 Algorithm description

In the following subsections, each of the algorithmic blocks is described in more detail.

Space point sorting

SiTrack, as all the algorithms operating at the LVL2 trigger, is designed to work in RoI-guided mode. This means that the first operations performed by SiTrack are the retrieval of the input RoI and the request for the Silicon space points it contains; as explained in the previous chapter, this request is handled by the region selector service.
The first algorithmic operation performed is the sorting of the retrieved space points, according to their physical module address. In particular, a pointer to each retrieved space point is inserted in a C++ standard library multimap [45], which uses a structure describing physical module addresses as a key for its entries.
As will be discussed in the following chapters, this procedure, while consuming a negligi-

ble fraction of the total algorithmic processing time, greatly speeds up data access for the subsequent reconstruction steps, and so turns out to be a convenient choice for the overall algorithm structure.

Track seeds formation

As already mentioned, the first logical layer, i.e. the set of modules containing the space points from which track reconstruction starts, always coincides with the B-layer. Given a space point on this layer, the corresponding second logical layer is identified using the Montecarlo map linking B-layer modules to other physical layers; this process is pictorially explained in figures 4.1 and 4.2. To grant faster access during the event processing, the entries for this map are loaded in memory at the algorithm initialization.
Every combination of space points from the first two logical layers undergoes a preliminary compatibility test based on their ϕ coordinates and on their alignment with respect to the central RoI η value. In particular the following cuts are applied:

$$\phi_{12} = |(\phi_2 - \phi_1)/(r_2 - r_1)| < \Delta\phi_{12},$$
$$\eta_{12} = |(r_2 - r_1)/(z_2 - z_1) - tan(\theta_{\mathrm{RoI}})| < \Delta\eta_{12},$$

where ϕ_n, r_n, z_n are the cylindrical coordinates of the space point coming from the n_{th} logical layer and θ_{RoI} is the angle corresponding to the central RoI η value.
The space point couples passing this selection are then fitted with a straight line and extrapolated back to the beam axis; for each track seed are evaluated the impact parameters z_{seed} and d_{seed}, i.e. respectively the Z and $R\Phi$ coordinates of the point, laying on the extrapolated trajectory, closest to the beam axis.
At this point, primary vertex reconstruction is performed as explained in next subsection, provided it is required by the analyzed event type and no external vertexing information is available.
Each track seed is finally accepted if the conditions

$$d_{12} = |(d_{seed} - d_{vtx})/\sqrt{r_2 - r_1}| < \Delta d_{12},$$
$$z_{12} = |z_{seed} - z_{vtx}| < \Delta z_{12},$$

are satisfied, where z_{vtx} and d_{vtx} are the coordinates of the primary vertex. While d_{vtx} is always taken to be 0, z_{vtx} can either be one of the vertices computed by SiTrack or the output of other packages; obviously, the second cut is not applied in case no vertex reconstruction is performed.
It must be noticed that some of the variables defined above are strongly correlated with the track parameters, while some others are not. In particular, η_{12} and z_{12} don't show any dependence from track parameters, provided the straight line approximation is valid in the RZ plane, i.e. approximately for $p_T > 2$ GeV; on the opposite, ϕ_{12} and d_{12}, being related to the bending of the reconstructed trajectory, show a strong p_T dependence. So, applying a cut on those two variables corresponds to selecting the p_T acceptance of the algorithm, as will be demonstrated in the section on tuning procedures.
During the algorithm initialization phase, it is also possible to select whether to include or

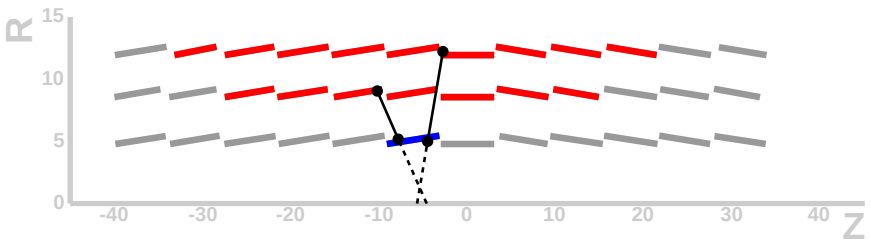

Figure 4.1: Pictorial view of the seed formation process in the RZ plane; couples are formed combining B-layer space points with those coming from different sets of modules identified by one or more logical layers.

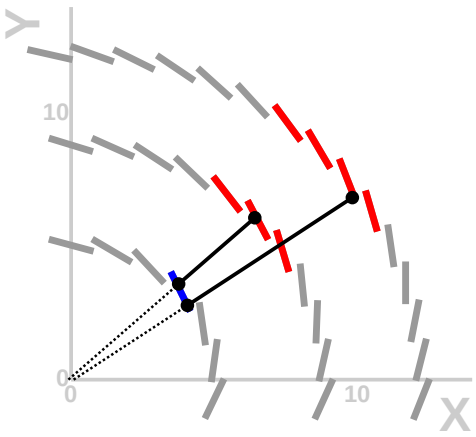

Figure 4.2: Pictorial view of the seed formation process in the $R\Phi$ plane; couples are formed combining B-layer space points with those coming from different sets of modules identified by one or more logical layers.

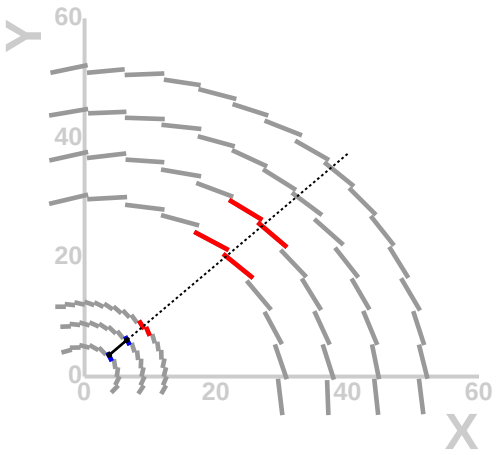

Figure 4.3: Pictorial view of the seed extrapolation process in the $R\Phi$ plane; triplets are formed combining space point couples belonging to a seed with those coming from different sets of modules identified by one or more logical layers.

not SCT modules in the second logical layer; this choice has implications on the vertex reconstruction and, in general, on tracking performance. As a matter of fact, the inclusion of SCT modules in the second logical layer increases the robustness of the algorithm and its tracking efficiency. On the other side, as explained in the next subsection, vertex reconstruction is based on track seeds; thus, since the seeds reconstructed using only the Pixel detector data have a better resolution on the Z impact parameter, the vertexing performance is improved if SCT modules are not used for seeding purposes. The effects of these contrasting choices have to be balanced, as will be discussed with a practical example in chapter 7.

Primary vertex reconstruction

The z coordinate of the primary vertex can be evaluated during the track seeding phase by histogramming z_{seed} for all the candidate seeds passing the preliminary η/ϕ selection and further separate cuts on z_{seed} and d_{seed}; these last two cuts are usually very different from the ones described in the previous section. In particular, the cut on z_{seed} corresponds to the maximum expected spread of the primary vertex position along the beam axis, so it is always set to 20 cm; the selection on d_{seed} corresponds, instead, to a very rough cut on p_T for the track seeds filling the vertexing histogram. For events containing high p_T jets, as in case of b-tagging samples, applying a strong cut on d_{seed} can efficiently reject most of the fake seeds, enabling to fill the histogram mostly with "signal" seeds.
The binning of the basic vertexing histogram is fixed; anyway, its maxima are evaluated using a sliding window approach, where the optimal window width is tuned for each event, according to the number of seeds found, and always ranges within user-selectable minimum and maximum values.
Once the histogram has been scanned using the sliding window, a fixed number of candidate vertices are identified and their z coordinates are taken as estimates of z_{vtx}.

Track extension

The last algorithmic phase of SiTrack extends each track seed with the addition of a third space point coming from outer Inner Detector layers. This is accomplished with the aid of a Montecarlo map that associates the couple of modules hit by each seed to a set of module lists (roads), where further hits most probably lay; a pictorial view of this step is given in figure 4.3. A subset of modules is then selected for each road, according to the distance from the beam line; different choices for the third logical layer lead, in general, to quite different track parameter resolutions and fake fractions. As a matter of fact, in case the outer logical layers are used, the lever arm of the space point triplet is increased, leading to a better p_T determination; anyway, in this case, also the track extrapolation error is increased, along with the number of fake candidates; obviously the opposite is true in case the innermost third logical layers are chosen.
Space points coming from the selected third layer modules are, first of all, filtered by the following preliminary cuts:

$$\phi_{23} = |(d\phi_{23} - d\phi_{12})/(d\phi_{23} + d\phi_{12})| < \Delta\phi_{23},$$
$$\eta_{23} = |(r_3 - r_1)/(z_3 - z_2) - (r_2 - r_1)/(z_2 - z_1)| < \Delta\eta_{23},$$

where $d\phi_2 3 = (\phi_3 - \phi_2)/(r_3 - r_2)$ and $d\phi_1 2 = (\phi_2 - \phi_1)/(r_2 - r_1)$.
In case the third point passes these cuts, the straight line corresponding to the track seed is extrapolated at r_3 and the following selections are applied:

$$d_{23} = \sqrt{((x_3 - x_{extrap})^2 + (y_3 - y_{extrap})^2)/(r_3 - r_2)^3} < \Delta d_{23},$$
$$z_{23} = |(z_3 - z_{extrap})\cos(\theta)| < \Delta z_{23},$$

where x_{extrap}, y_{extrap} and z_{extrap} are the coordinates of the point extrapolated at r_3 and θ is the angle between the seed and the beam line. If these conditions are also met, the triplet

obtained with the addition of the third space point to the seed is selected as a possible track candidate.
Again, provided the straight line approximation is valid in the RZ plane, no dependence from track parameters is shown by the ϕ_{23}, η_{23} and z_{23} cuts; on the opposite, d_{23}, in analogy to what described for the ϕ_{12} and d_{12} seeding cuts, is strongly correlated with p_T.
A further problem is posed by the fact that each space point can belong to more than one of the extended triplets; so, it must be possible to filter some track candidates, if an unambiguous use of the space points is desired.
The procedure for the overlap removal is performed in two steps and is based on the following track quality parameter

$$D = \sqrt{(d_{23}/\Delta d_{23})^2 + (z_{23}/\Delta z_{23})^2}.$$

First of all, for each seed, only the extension having the smallest D value is kept. Then, after all seeds have been extended, candidate tracks are grouped together if they share at least one space point; this grouping is performed following an associative rule, so that two tracks in the same group can be non overlapping if both share a cluster with a third track. The tracks in each group are then ordered by quality parameter and only the one with the smallest D value is retained. Those sharing a space point with it are discarded, while the others are regrouped and the procedure is iterated.
Each of these ambiguity resolution steps can be independently deactivated and, in that case, all the triplets compatible with the selection cuts are taken as candidate tracks. This operation mode is mainly used to evaluate the impact of ambiguity resolution on the fake fraction and on the reconstruction efficiency.
After the final track candidates set is available, each corresponding triplet of space points is fitted with a straight line in RZ and with a circle in $R\Phi$; from these fits the following five track parameters are extracted:

- η, the direction in the RZ plane;
- $\phi 0$, the direction in the $R\Phi$ plane evaluated at the closest distance from the beam line;
- z_0, the Z impact parameter;
- d_0, the $R\Phi$ impact parameter;
- p_T, the transverse particle momentum.

4.2.3 Tuning of the selection parameters

The optimization of the cuts, used in the tracks finding phase, is performed looking at the distributions of the corresponding parameters, for the good and the fake reconstructed tracks. Here, a good track is a candidate track in which all the three points where actually produced by the same generated track. In particular, for each cut is required an efficiency exceeding 95%, in order to mantain a reasonable overall tracking efficiency, while rejecting as much combinatorial background as possible.

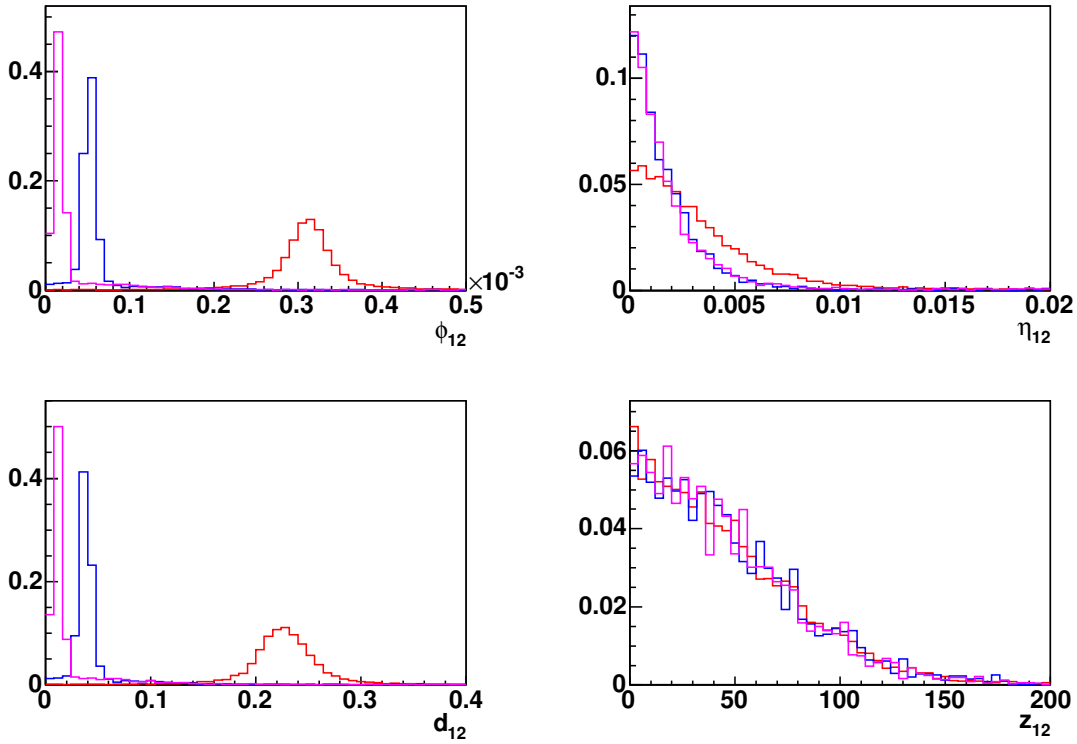

Figure 4.4: Seeding cut variables for single muons with different p_T values; red, blue and magenta curves correspond respectively to 1, 6 and 20 GeV reconstructed tracks.

The cuts are roughly independent from the logical layer configuration adopted. Infact, variables such as ϕ_{12} or d_{23}, that could be in principle sensitive to the extrapolation radii $r_{12} = r_2 - r_1$ and $r_{23} = r_3 - r_2$, which are the quantities that most strongly depend on the layer configuration, contain scaling factors depending on r_{12} and r_{23} which lead to a reasonable uniformity.
So, the only dependence left is the p_T one; anyway, this is a useful feature, since it allows to apply a p_T threshold on reconstructed tracks before the fit is executed, thus leading to smaller processing times.
The distributions of the cut variables described above are shown in figures 4.4 and 4.5, for three simulated data samples containing single muons with p_T equal to 1, 6 or 20 GeV; in these plots the p_T dependence of ϕ_{12}, d_{12} and d_{23} can be noticed. Furthermore, η_{23} and z_{23} clearly show that, as long as the straight line parametrization is valid in RZ (for 6 and 20 GeV), no p_T dependence is found; anyway, as the transverse momentum falls to 1 GeV, the shape of these cut variables drastically changes. As a final comment, no cut is applied on z_{12}, since no vertex reconstruction is performed on single particles. The resulting cuts, corresponding to three different p_T acceptances, are summarized in table 4.1. In next section,

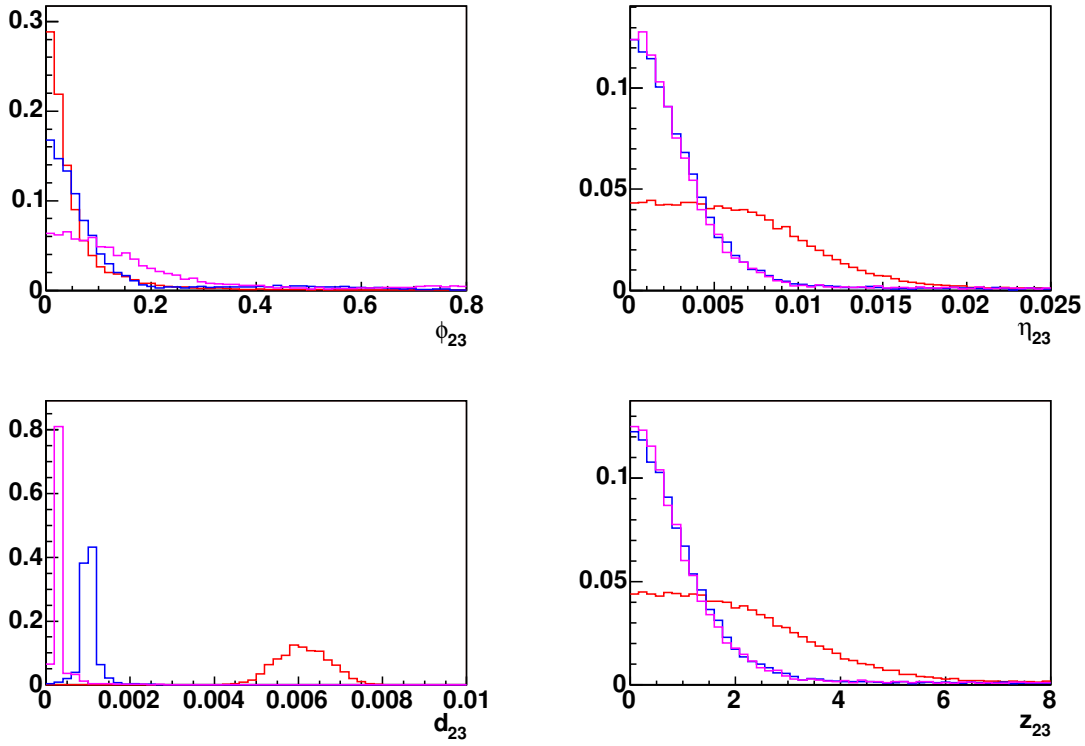

Figure 4.5: Extension cut variables for single muons with different p_T values; red, blue and magenta curves correspond respectively to 1, 6 and 20 GeV reconstructed tracks.

	$p_T > 1$ GeV	$p_T > 6$ GeV	$p_T > 20$ GeV
$\Delta\phi_{12}$	0.5×10^{-3}	0.1×10^{-3}	0.05×10^{-3}
$\Delta\eta_{12}$	0.015	0.01	0.01
Δd_{12}	0.35	0.07	0.04
$\Delta\phi_{23}$	0.6	0.6	0.6
$\Delta\eta_{23}$	0.025	0.015	0.015
Δd_{23}	0.008	0.002	0.001
Δz_{23}	7	4	4

Table 4.1: Cut values for three different p_T acceptances, evaluated on single muon samples.

these cuts will be applied to the same muon samples, in order to characterize the performance of SiTrack on single particles.

4.3 Performance studies

In order to evaluate the performance of any tracking algorithm, three kinds of information have to be provided: its reconstruction efficiency for good tracks, the percentage of fake reconstructed track candidates and its resolution on the fitted track parameters.
Working on simulated samples, these results can be easily obtained, comparing the reconstructed track samples with the Montecarlo generated particles. Anyway, some definitions, such as the ones for good tracks and fake candidates, must be provided before the performance is evaluated; the definitions adopted in the following are explained in next section. Finally, in the last section, the results obtained on single muon reconstruction are summarized.

4.3.1 Tracking quality definitions

Once a set of track candidates is produced by SiTrack, the link between the reconstructed tracks and the Montecarlo particles is established through the space points; each track is associated to the particle that produced the majority of the space points it is built from; the number of linked space points is also provided.
Exploiting this information, the definitions used to evaluate the tracking performance can be provided as follows:

- reconstructible Montecarlo particle: a particle passing a set of geometrical selection cuts (being contained in one of the processed RoIs, crossing the pixel B-layer, pointing to the primary vertex) and a p_T cut;

- good track: a reconstructed track linked to a reconstructible particle by at least two space points; the geometrical and p_T cuts used for the Montecarlo particles are applied to the reconstructed tracks too;

- best track: for each reconstructible particle, more than one good track can be available; the best track is defined as the one with the most precise η and ϕ matching w.r.t. the linked particle;

- fake track: a reconstructed track (passing geometrical and p_T cuts) which is not a good track;

- efficiency: ratio between best tracks and reconstructible particles;

- fake fraction: ratio between fake tracks and all the reconstructed tracks passing the applied cuts;

- track multiplicity: the number of reconstructed tracks passing the applied cuts, averaged on each RoI.

These ingredients are then combined to produce a set of histograms, summarizing the performance of the tracking algorithm; an example is provided in next section.

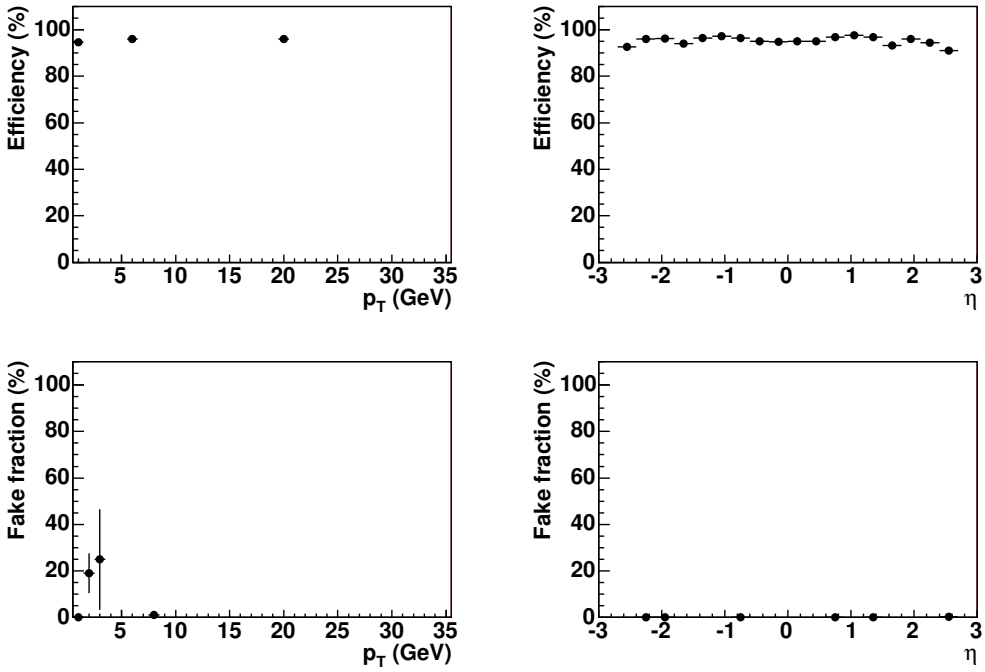

Figure 4.6: Tracking efficiency for single muons with different p_T values; every bin in η and p_T is normalized to the track candidates it contains.

4.3.2 Results on single muons reconstruction

Here are summarized the results obtained from the analysis of single muon samples having p_T equal to 1, 6 and 20 GeV, reconstructed in the LVL2 framework using SiTrack. The datasets used here contain no pile-up interactions, in order to provide a very clean way of tuning the track finding algorithm; the only source of space points which are not linked to a true particle is thus the electronic noise.

	$p_T = 1$ GeV	$p_T = 6$ GeV	$p_T = 20$ GeV
Efficiency	94.7 ± 1.1 %	96.0 ± 1.1 %	96.0 ± 1.1 %

Table 4.2: Tracking efficiency for single muons having three different p_T values.

In figure 4.6 the efficiency and fake histograms are shown; in particular:

- in the top row the efficiency is plotted as a function of p_T and η; for the η plot the selected 0.5 GeV p_T cut is applied;
- in the bottom row the fake fraction is plotted as a function of p_T and η.

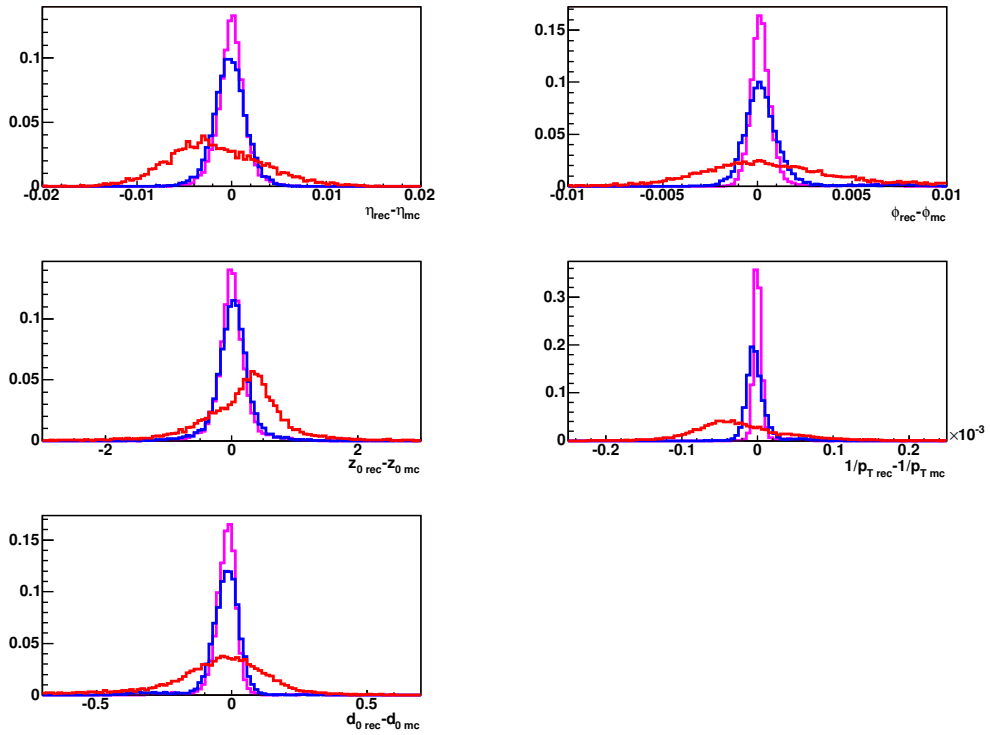

Figure 4.7: Track parameter resolutions for single muons with different p_T values; red, blue and magenta curves correspond respectively to 1, 6 and 20 GeV particles.

It can be noticed that the efficiency is very stable for all the three p_T values, as summarized in table 4.2, and over the η range covered by the Inner Detector tracking system. The fake fraction is, instead, obviously negligible, since it is due only to hits produced by the electronic noise inside the detectors.

	$p_T = 1$ GeV	$p_T = 6$ GeV	$p_T = 20$ GeV
η	$4,8 \times 10^{-3}$	1.7×10^{-3}	1.3×10^{-3}
ϕ (mrad)	3.4	0.83	0.4
z_0 (μm)	420	210	180
$1/p_T$ (GeV^{-1})	44×10^{-3}	10×10^{-3}	4.2×10^{-3}
d_0 (μm)	150	45	26

Table 4.3: Track parameters resolution for single muons having three different p_T values.

Figure 4.7 shows the resolution plots for the five track parameters (η, ϕ, z_0, $1/p_T$ and d_0), i.e. the distributions for the difference between their reconstructed value and the corresponding Montecarlo generated one; in particular, these plots are filled using the best tracks with at

least two space points linked to the same Montecarlo particle.
The resolution for each parameter, evaluated as the σ of the gaussian distribution that best fits the corresponding resolution plot, is reported in table 4.3 as a function of the transverse momentum of the generated muons.
The resolution values obtained on 1 GeV muons evidently show that, for those p_T values, the SiTrack fit procedure, performed with a straight line in RZ and with a circle in $R\Phi$, doesn't describe correctly the helical particle trajectory. Furthermore, in that case, the resolution plots are not even centered on zero; this can be easily explained, because the samples used contain only negatively charged muons and thus the trajectory curvature effect is highly asymmetrical. A better resolution could be achieved, even on very low p_T samples, performing a more precise track fit. Anyway, as explained in the following, the best choice could be to try to extend the reconstructed track candidates in order to use all the Silicon detector layers; this way the final fit, necessarily more sophisticated, would automatically provide better results.

Chapter 5

Application to Electron and Photon Selection

5.1 Physical relevance of e/γ selection

Many interesting physical phenomena at LHC, such as $H \to 4\,e$ or $H \to \gamma\gamma$, lead to a final state containing isolated high p_T electrons and/or photons. These kind of signatures are always very relevant in hadronic experiments, since they provide, along with muon signatures, one of the cleanest ways of selecting the signal events out of the enormous QCD background. As a consequence, they are a key ingredient in the reconstruction of possible discovery channels characterized by a potentially high statistical significance.
Furthermore, the electron selection will prove very valuable also for detector calibration and alignment and during the commissioning phase; as an example, a common channel like $Z \to e^+e^-$, which provides a multipurpose tool for many key applications, can be easily selected by a double electron trigger.
Obviously, electron and photon reconstruction mainly exploits data coming from the electromagnetic LAr calorimeter, which provides a precise measurement of their energy; anyway, the ID tracking system plays a fundamental role too. As a matter of fact, combining an EM calorimeter cluster with a track reconstructed inside the Inner Detector, it is possible to obtain the complete reconstruction of the kinematical properties of these particles, taking into account bremsstrahlung effects and photon conversions. Furthermore, significant particle identification and rejection of fake candidates can be achieved; this proves essential for on-line event selection, as described in detail in next section.

5.2 The electron and photon trigger menus

In this section, the current ATLAS trigger strategy for the selection of electron and photon candidates will be briefly described.

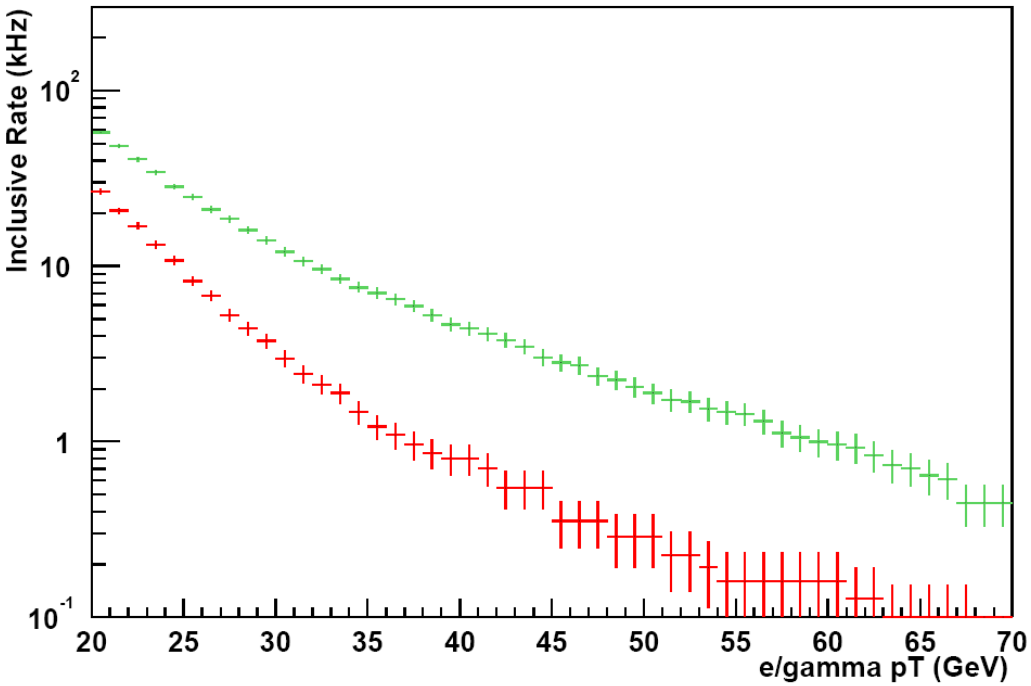

Figure 5.1: Electron and photon trigger rate versus E_T threshold without (top) and with (bottom) isolation requirements at start-up luminosity.

5.2.1 Single and double object trigger menus

In the current budget for the ATLAS trigger menus, the inclusive electron and photon triggers are expected to contribute an important fraction of the total high-p_T trigger rate.
Single and double object trigger menus are foreseen for both the electrons and the photons; obviously the single object LVL1 triggers are the ones providing a bigger rate and thus undergo tighter E_T thresholds; 25 GeV and 30 GeV thresholds are currently foreseen for electrons, respectively at start-up and design luminosity, while the start-up threshold for the single photon trigger is set to 60 GeV.
The rate of the LVL1 electron/photon triggers is dominated by misidentified jets; an isolation cut must hence be applied at LVL1, spoiling part of the selection efficiency, but drastically reducing the trigger rate. Studies, based on the full LVL1 simulation, have been performed in order to estimate the trigger rate for the single and double electron/photon triggers as a function of the E_T threshold adopted [46]; these studies have been performed for both the start-up and the design luminosity regimes. Figure 5.1 shows the estimated trigger rate for the single electron and photon trigger as a function of the E_T threshold for a luminosity of 2×10^{33} cm^{-2}s^{-1}; the upper and lower bands give the two rates obtained in case the isolation requirement is applied or not; for each E_T threshold value quoted the efficiency for selecting genuine electrons exceeding it is 95%.

5.2.2 High Level Trigger implementation

The strategy for electron and photon selection at the HLT is based on the RoI mechanism. In particular, LVL2 reconstruction uses information on the transverse energy and the direction of the electromagnetic clusters selected by the LVL1 trigger, so that typically around 2% of the whole event needs to be further analyzed. First of all, the energy and position measurements obtained at LVL1 are refined; the leakage into the hadronic calorimeter is evaluated and variables related to the shower shape in the electromagnetic calorimeter are used to perform preliminary particle identification, distinguishing isolated objects from jets. If a candidate is found to be consistent with an electron, track reconstruction is performed in the ID; cluster to track association is done using (η, ϕ) matching criteria, achieving further rejection against fake candidates. In case the matching was successful, the E_T/p_T ratio between the transverse energy measured in the EM calorimeter and the transverse momentum of the corresponding ID track is evaluated for particle identification; the e/π separation power can be further enhanced by the transition radiation measurement performed in the TRT detector.
In the case of photon candidates, reconstructed EM clusters undergo tighter shower shape cuts.
If the objects under analysis fulfill the required signatures, the selected event and the corresponding LVL2 result are passed to the EF, where information on the complete event is available, along with more precise calibrations and alignment constants. Even if selection at the EF follows the same scheme described for LVL2 operation, the looser timing constraints enable to employ more sophisticated reconstruction algorithms, taking care of bremsstrahlung recovery for electrons and conversion reconstruction for photons.

5.3 On-line track reconstruction

Studies devoted to tune the track reconstruction for isolated electron triggers are performed on signal samples containing a single electron track having a fixed p_T value (25 GeV for start-up luminosity and 30 GeV for design luminosity), which are mixed with a set of pile-up events, to reproduce the desired luminosity conditions.
In this section, the configuration adopted to reconstruct high p_T isolated electrons with SiTrack will be discussed; in particular, the distributions for the tracking cut variables will be shown, to provide an example of tuning in conditions where the background due to pile-up interactions is relevant.
After the tuning will be defined, the corresponding reconstruction performance will be evaluated for both the start-up and the design luminosity regimes.
Finally, the impact of LVL2 tracking with SiTrack on the electron selection menus, obtained from studies performed by the ATLAS e/γ community, will be reported.

5.3.1 LVL2 tracking configuration

The detector simulation used for these studies corresponds to the complete detector scenario, so all the Pixel detector layers are available for track reconstruction.

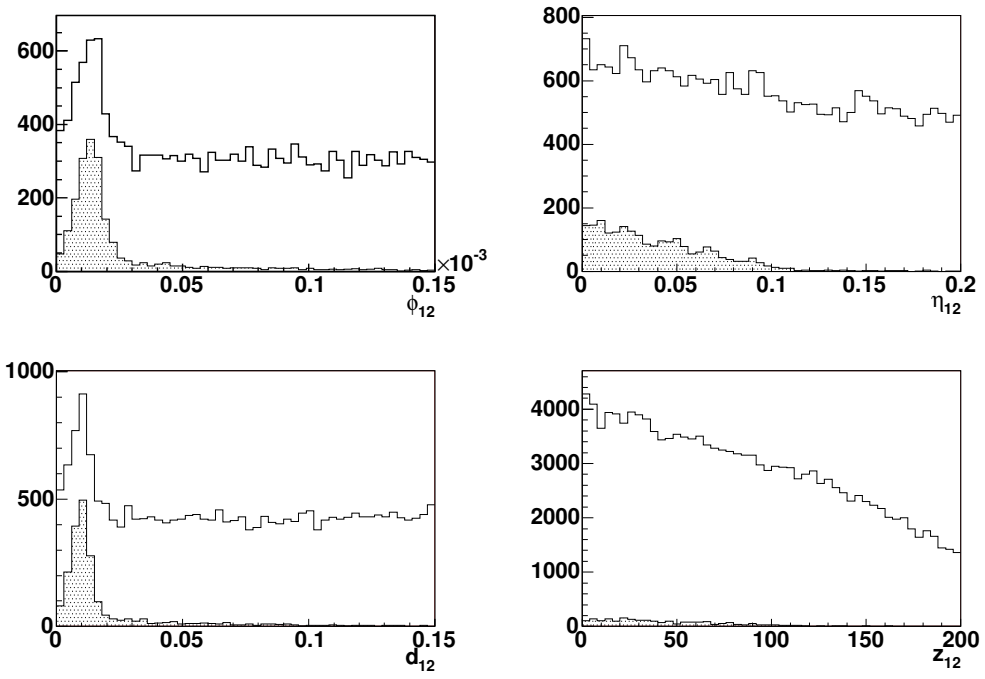

Figure 5.2: Seeding cut variables for single electrons with $p_T = 25$ GeV at start-up luminosity; the distribution for the signal seeds (shaded) is compared with the overall one.

As far as the logical layer configuration is concerned, track seeds are formed using the B-layer and the following two logical layers, excluding SCT space points; this choice aims at reducing the amount of combinations analyzed, to improve the timing performance and reduce the fake fraction. The seeds are then extended with SCT space points from two further logical layers.

As for the single muon case treated in chapter 4, no primary vertex reconstruction is attempted. As a matter of fact, since the amount of signal seeds produced by a single electron track is irrelevant with respect to the background ones, especially at high luminosity, it is very unlikely that vertex reconstruction can be efficiently performed. This choice could in principle affect the timing performance; anyway, since maximum efficiency is required only for high p_T values, very tight cuts can be applied to the tracking variables, as shown in the following. This greatly reduces the number of seeds and track candidates analyzed and thus leads to fast execution times.

Coming to the tracking variables, on which cuts are applied during the seeding and the extension phases, their distributions are shown in figures 5.2 and 5.3. In those plots, the signal distributions, corresponding to seeds and triplets made of hits coming from the single electron track, are compared with the overall ones, containing the combinatoric background produced by pile-up hits. It can be noticed that the signal and the background are very well separated; this means that, applying cuts on these variables, the fraction of fake track

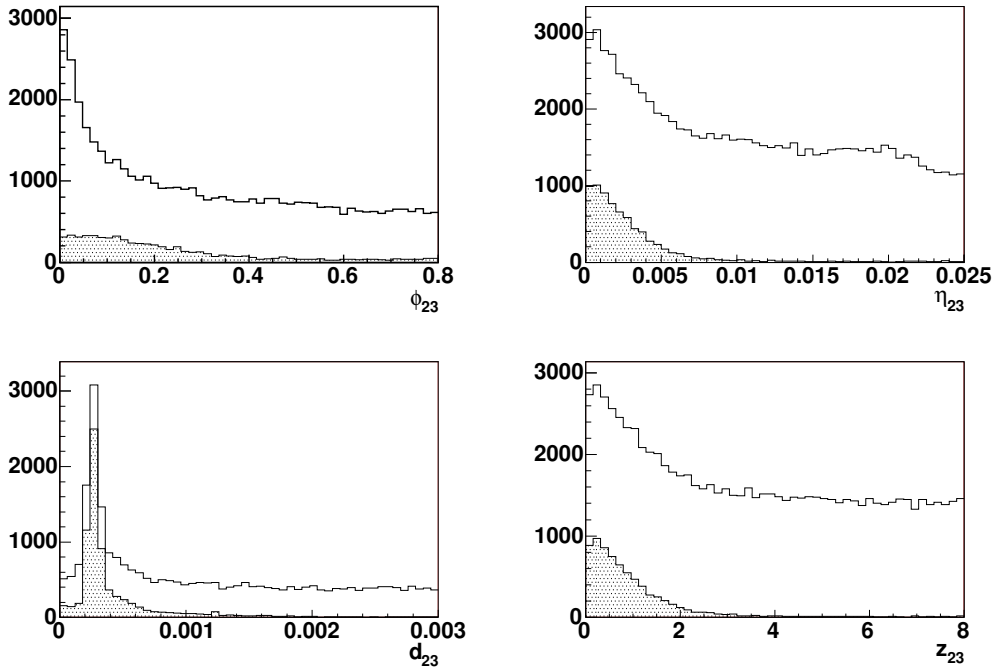

Figure 5.3: Extension cut variables for single electrons with $p_T = 25$ GeV at start-up luminosity; the distribution for both the signal triplets (shaded) is compared with the overall one.

$\Delta\phi_{12}$	0.075×10^{-3}	$\Delta\eta_{12}$	0.12
Δd_{12}	0.05	Δz_{12}	-
$\Delta\phi_{23}$	0.6	$\Delta\eta_{23}$	0.01
Δd_{23}	0.001	Δz_{23}	4

Table 5.1: Cut values tuned for the reconstruction of single electron samples; since primary vertex reconstruction is not performed, no cut is applied on z_{12}.

candidates in the reconstructed sample can be easily kept under control.
The resulting cut values, adopted for both luminosity conditions, are given in table 5.1.

5.3.2 LVL2 track reconstruction performance

The results obtained on single electron samples at both start-up and design luminosity are shown in figure 5.4 and summarized in table 5.2.
It must be noticed how the efficiency is close to the one obtained for single muons without pile-up; furthermore, it also proves very stable with respect to the luminosity conditions. As a matter of fact, the only significant difference between start-up and design luminosity is the

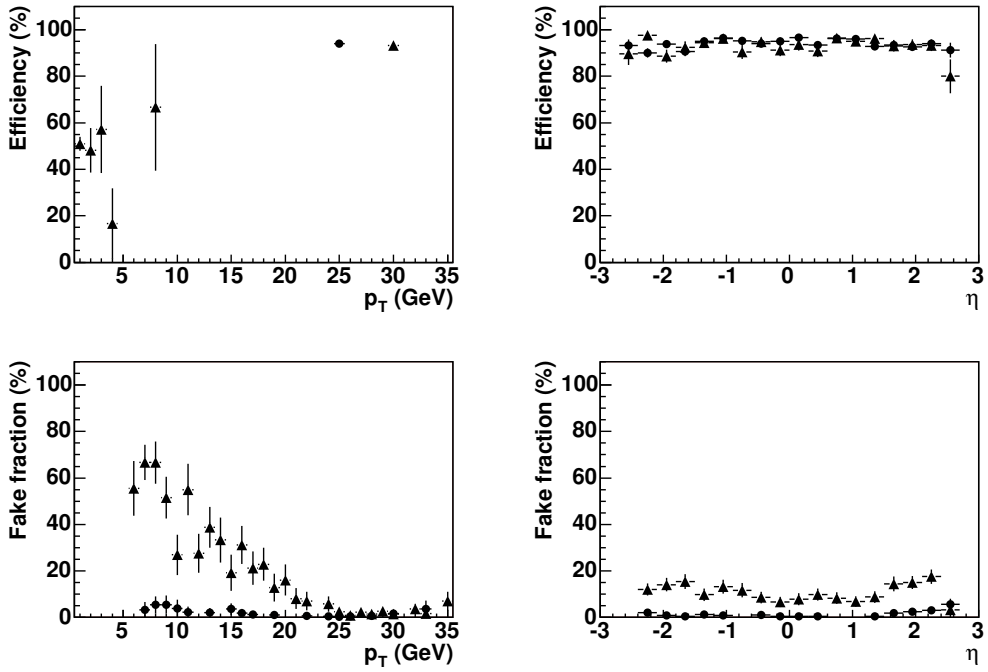

Figure 5.4: Tracking efficiency for single isolated electrons at start-up (circles) and design (triangles) luminosity. The upper and lower plots show respectively the tracking efficiency and the fake fraction, as a function of p_T and η.

	Start-up luminosity	**Design luminosity**
Efficiency	94.0 ± 1.6 %	93.3 ± 2.1 %
Fake fraction	1.1 ± 0.2 %	11.1 ± 0.6 %

Table 5.2: Tracking performance for single electrons at start-up and design luminosity.

fraction of reconstructed fake tracks; anyway, given the tight cuts adopted, their presence is almost negligible, especially in the p_T range where the signal lays.
Timing measurements have been performed on a 2.4 GHz processor, in order to evaluate whether the average algorithmic processing time is compatible with the requirements posed by the LVL2 environment. Figure 5.6 shows the distribution for the time consumed, in both luminosity conditions, processing an electromagnetic RoI identified at LVL1; figure 5.5 shows, instead, the contribution of each algorithm block to the overall time.
The average values, given in table 5.3, show that the performance of the SiTrack algorithm is well compatible with the LVL2 environment, which requires an average trigger decision time within 10 ms, even in the hypothesis of reconstructing more than one RoI per event.
The only open issue, from this point of view, is the time taken by the data processing, per-

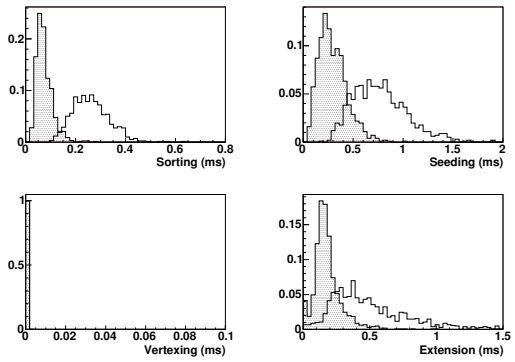

Figure 5.5: Processing time consumed by each algorithm block; since the vertexing step is skipped, the corresponding processing time is always negligible.

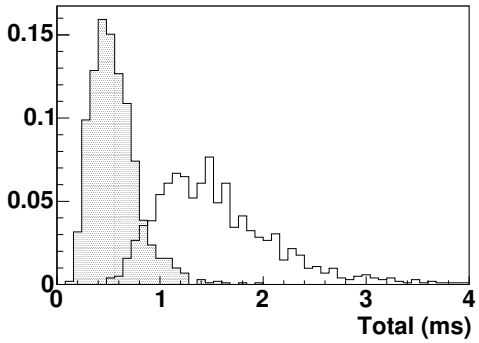

Figure 5.6: Processing time consumed by SiTrack in order to reconstruct the tracks contained in the EM RoI identified at LVL1.

	Start-up luminosity	**Design luminosity**
Sorting (ms)	0.07	0.26
Seeding (ms)	0.3	0.77
Extension (ms)	0.18	0.5
Total (ms)	**0.56**	**1.5**

Table 5.3: Timing measurements for single electron reconstruction at start-up and design luminosity; the average processing time taken by each reconstruction step is given, along with the average total algorithmic processing time.

formed before executing the reconstruction algorithms. A precise estimate for this quantity is not yet available and is out of the scope of this work; anyway, past studies have shown that its contribution to the overall timing should be lower than the one from reconstruction algorithms.

5.3.3 Impact on selection efficiency and event rate

In this section, the LVL2 tracking contribution to the performance of the HLT e/γ selection for single trigger menus is discussed.
The performance of the e/γ trigger menus has been evaluated [47] on Monte Carlo samples for which the detector response was simulated in detail; results are given in terms of the efficiency for the real electron signal and of the expected output rate, directly related to the rejection power for fake candidates.
Table 5.4 shows the efficiency and expected rate for the trigger menu selecting single isolated electrons with a transverse energy (E_T) exceeding 25 GeV ($e25i$) at initial luminosity; errors only take into account the statistical uncertainty contribution, while it should be noted that the uncertainties in the QCD di-jet cross-sections at the LHC are of the order of 2-3. Results

Trigger Step	**Rate (Hz)**	**Efficiency (%)**
LVL2 Calo	1.948 ± 46	95.6 ± 0.3
LVL2 Tracking	364 ± 21	89.4 ± 0.5
LVL2 Matching	143 ± 12	87.7 ± 0.6
EF Calo	101 ± 15	86.1 ± 0.6
EF Tracking	71 ± 10	82.0 ± 0.6
EF Matching	34 ± 6	79.7 ± 0.7

Table 5.4: Performance of the single isolated electron HLT trigger at initial luminosity.

have been evaluated on a simulated sample containing single electrons with $p_T = 25\,\text{GeV}$ over the full tracking rapidity range $|\eta| < 2.5$. The efficiencies and rates are evaluated, after each HLT selection step, with respect to a LVL1 output efficiency of 95% and a LVL1 EM cluster rate of 12 kHz, which are preliminary values.
Results show that a final electron selection efficiency of 80% with respect to LVL1 can be achieved with a final rate around 35 Hz. The final selected sample mainly contains real electrons (44% from electrons from b and c quark decays, 21% from converted photons, 19% from $W \to e\nu$ decays, 1% from $Z \to ee$ decays). Only 25% of the rate is coming from fake clusters.
These results clearly show that, matching the tracks reconstructed at LVL2 in the ID with calorimeter clusters, a significant rate reduction (corresponding to more than a factor of ten) can be achieved at the cost of a modest efficiency drop (around 8%). These results are even more interesting if we consider that, most probably, great part of the signal events lost at LVL2 contain electrons which undergo strong bremsstrahlung radiation, which wouldn't be correctly reconstructed even by the offline software; in order to prove this hypothesis, a detailed comparison of the on-line and offline results is currently being performed.

Chapter 6

Application to the b-tagging Selection

6.1 Physical relevance of b-tagging selection

Final states containing more than one b-jet have been proposed as signatures with a substantial discovery potential in different sectors [32]; the ability to separate b-jets from light-quark and gluon jets is thus an important ingredient for the physics selection strategy in ATLAS.
An example application of the b-tagging capabilities of both the on-line and offline reconstruction software is given by the study of the $H \to b\bar{b}$ decay, where the Higgs boson comes from the associated production channels WH, ZH and $t\bar{t}H$.
Another interesting case is the selection of final states containing four b-jets; this is fundamental in the searches for Higgs bosons in the intermediate mass range, 80 GeV $< m_H <$ 180 GeV. In particular, the most promising channels are $b\bar{b}H$, $b\bar{b}A$ with $H/A \to b\bar{b}$ or $H \to hh \to b\bar{b}b\bar{b}$.
In next section, these examples will be used to explain the relevance of an efficient b-tagging on-line selection, in particular at LVL2, in order to enhance the ATLAS jet trigger strategy. The following section will then study the LVL2 track reconstruction problem for jet topologies, applying the SiTrack algorithm to the reconstruction of b-jets produced in Higgs boson decays. Finally, in the last section, an on-line b-tagging algorithm will be proposed and its performance, based on LVL2 track reconstruction, will be studied.

6.2 The jet trigger menus

First of all, in this section a brief summary of the current LVL1 jet trigger menus will be given; the possible impact of an HLT b-tagging selection will be then discussed.

6.2.1 Single and multiple LVL1 jet trigger menus

Even if complete studies on the jet trigger selection are not yet available, preliminary results have shown that, given the enormous background from QCD jet production, a safe LVL1

trigger rate from jets should be obtained adopting rather high E_T thresholds. In particular, J180, 3J75, and 4J55 thresholds are foreseen at 1×10^{33} cm^{-2} s^{-1}, while J290, 3J130, and 4J90 should be used at 1×10^{34} cm^{-2} s^{-1}. This kind of studies, anyway, always foresees a large safety factor accounting for the unknown QCD rates; so, hopefully, these numbers should result pessimistic once the first physics runs will be performed.
Work is in progress to tune the LVL1 thresholds also for the present start-up scenario, foreseeing a luminosity of 2×10^{33} cm^{-2} s^{-1}.

6.2.2 High Level Trigger b-tagging

The Higgs boson search channels mentioned before provide two interesting and complementary use cases for a b-tagging selection at the HLT.
Its probably most important application is, as a matter of fact, the selection of channels such as $b\bar{b}H$ or $b\bar{b}A$, with $H/A \to b\bar{b}$, or $H \to hh \to b\bar{b}b\bar{b}$; all of these contain four b-jets in the final state. The main drawbacks of these channels are the multi-jet QCD background and their low rate; furthermore, the present LVL1 menu for three and four jets, described above, provides a modest efficiency for their selection.
Anyway, the use of a b-tagging selection at the HLT could provide additional flexibility and thus possibly better performance with respect to the standard strategy. In particular, for these topologies, containing many b-jets in the final state, the ability to separate them from jets generated by gluons and light quarks could allow a relaxation of the jet trigger E_T thresholds at LVL1, and hence lead to an increased signal selection efficiency.
The other interesting case is that of $H \to b\bar{b}$ decays from H associated production; these events are triggered at LVL1 by a lepton, coming from the decay of one of the particles produced in association with the Higgs boson (W, Z, t). So, in this case, the HLT b-tagging selection cannot be used to lower the LVL1 threshold and to increase the acceptance for signal events; anyway it can still play an important role, reducing the background, and hence the rate, for the events already selected by the leptonic trigger.
The study presented in this chapter will focus on the LVL2 implementation, which is the most crucial part of the HLT b-tagging strategy; as a matter of fact, even if b-tagging at the EF could provide a much better performance, it would not enable to use lower LVL1 jet trigger thresholds. Since a b-tagging selection at LVL2 requires fast track reconstruction capabilities, next section will cover the application of the SiTrack algorithm to this kind of event topology.

6.3 On-line track reconstruction

In this section, the LVL1 and LVL2 parameters adopted for the reconstruction and the identification of b-jets will be described. In particular, the tuning for track reconstruction with SiTrack and the corresponding performance will be discussed.

6.3.1 Data samples used

The b-tagging performance studies presented in this chapter are characterized on b-jets coming from $H \rightarrow b\bar{b}$ decays, where the Higgs boson has a mass of 120 GeV and is produced in association with a W. The standard background sample are the corresponding u-jets, taken as representatives of the light-flavour jets, obtained by artificially replacing the b-quarks from the Higgs decay with u-quarks.
Even in this very simple situation, the association between RoI and jets is not uniquely defined. As a matter of fact, a generic x-quark in the final state of an interaction or a decay can radiate gluons and, therefore, change its direction. An RoI from $H \rightarrow b\bar{b}$ or $H \rightarrow u\bar{u}$ is labeled as x-jet ($x = b$, u) if an x-quark from the original hard process pointed, after final state radiation, along the RoI direction within an angular distance of $\Delta R = \sqrt{\Delta\eta^2 + \Delta\phi^2} < 0.1$.

6.3.2 LVL1 configuration

As far as the LVL1 trigger simulation is concerned, a menu based on the selection of jet RoIs exceeding an E_T threshold of 30 GeV was adopted; these RoIs were then used at LVL2, in order to select the corresponding $\Delta\eta \times \Delta\phi = 0.4 \times 0.4$ regions centered on their direction.
Figure 6.1 shows the impact of the reconstructed E_T threshold adopted on the p_T distribution for the signal sample.
It can be noticed that the applied threshold biases the signal toward p_T values above 50 GeV.

6.3.3 LVL2 tracking configuration

The LVL2 track reconstruction, needed by the b-tagging selection, was performed using the SiTrack algorithm.
Since the detector simulation used for these studies corresponds to the complete detector scenario, the logical layer configuration adopted inside SiTrack almost coincides with the one described in chapter 5. In particular, track seeds are formed using the B-layer and the following two logical layers, excluding SCT space points in order to reduce the amount of processed data and to enhance the vertexing performance. The seeds are then extended with SCT space points from two further logical layers, exploiting the large lever arm to obtain a good precision on track parameters in the $R\Phi$ plane.
The most relevant quantities which have been specifically tuned for track reconstruction on jets are the p_T acceptance and the parameters for primary vertex reconstruction.
Among the requirements posed by the b-tagging selection, there is that of achieving the best possible tracking efficiency and purity down to reconstructed p_T values around 2 GeV; to achieve this goal, the cuts on ϕ_{12}, d_{12} and d_3 have been tuned on Montecarlo tracks with simulated transverse momentum exceeding 2 GeV. Tight values have been instead adopted for the other cuts, which are almost independent from p_T; this choice is guided by the requirement of reconstructing track samples containing a low fraction of fake candidates, even if this leads to a reduced tracking efficiency.
Moving to the tuning of the primary vertex identification, first of all the z_0 resolution of the track seeds has been evaluated, obtaining $\sigma(z_{0seed}) \sim 300\mu$m. The default sliding window width has hence been set to 1 mm. The d_{12} selection for the vertexing histogram has been

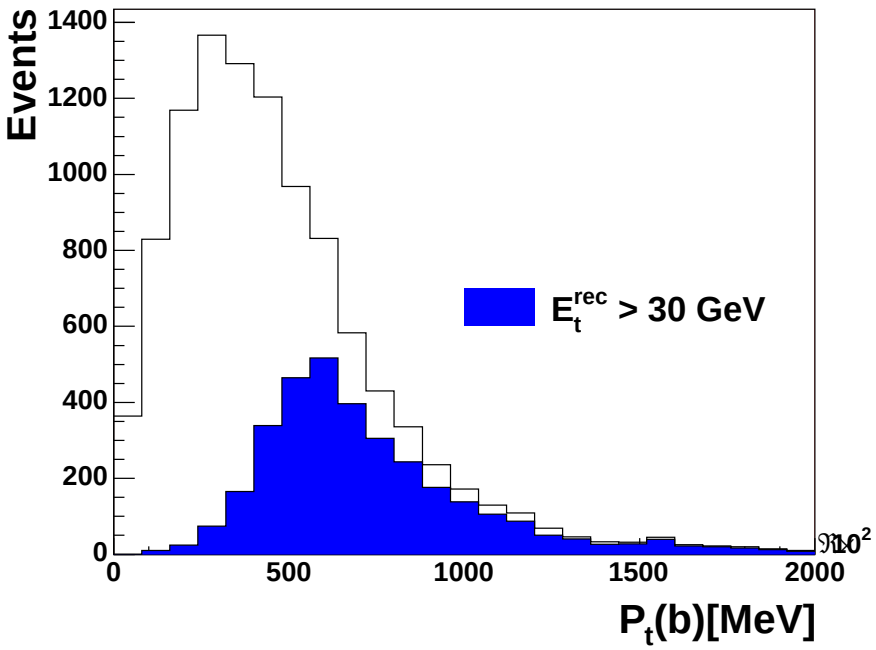

Figure 6.1: Distribution of the transverse momentum for the b-quarks matching the jet RoIs produced applying 30 GeV LVL1 E_T threshold; the p_T distribution for the unbiased signal sample is also shown.

tuned in order to be slightly tighter than the one adopted in the track reconstruction; as already explained in chapter 4, this choice aims at enhancing the contribution of signal seeds over the background ones.
Finally, the same tuning has been adopted for both the luminosity conditions under study.

6.3.4 LVL2 track reconstruction performance

The performance of the SiTrack algorithm has been evaluated, using the definitions described in chapter 4, on both the b-jet and u-jet samples. Given the complete equivalence of the results obtained in the two cases, u-jet plots will be used in the following, since they are characterized by an higher statistics.
The plots in figure 6.2 show the reconstruction efficiency and the fake fraction, as a function of p_T and η of the simulated tracks, for both luminosity conditions; in the η plot, the efficiency is evaluated on tracks having $p_T > 2$ GeV.
First of all, it must be noticed that the track reconstruction performance proves to be robust with respect to the background conditions; infact, the efficiency isn't much different in the two cases, while the fake fraction only doubles as the amount of pile-up tracks is increased by a factor of five.

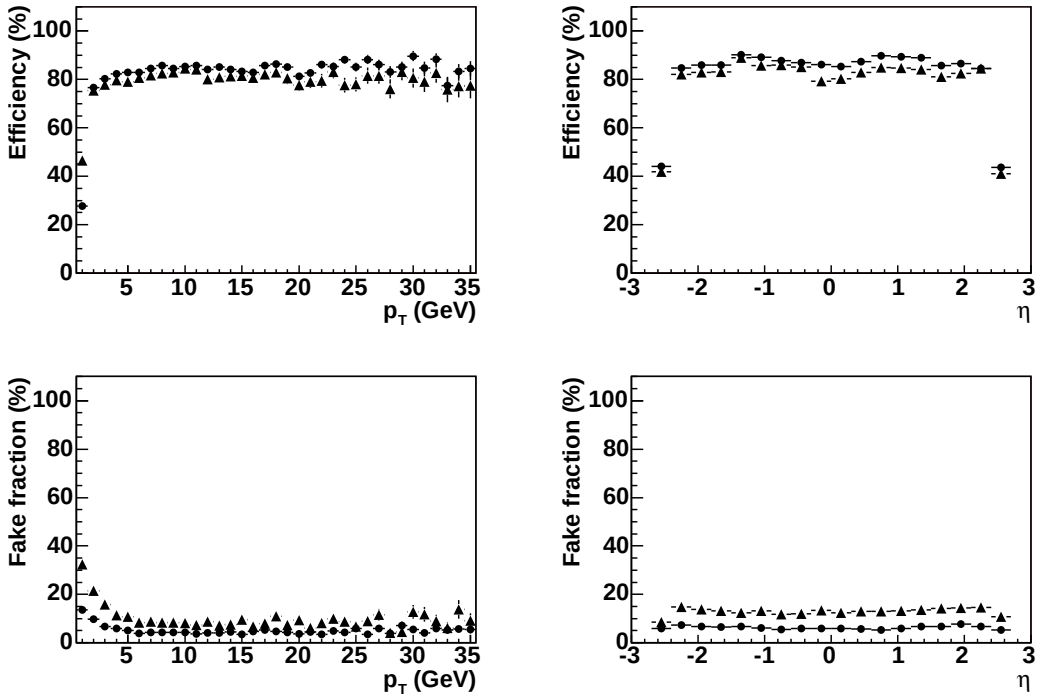

Figure 6.2: Tracking performance on b and u-jet samples. The upper two plots show the tracking efficiency as a function of p_T and η; in particular, the efficiency quoted in the left plot refers to tracks having a $p_T > 2$ GeV. The lower two plots, instead, show the fake fraction, again as a function of p_T and η.

	Start-up luminosity	**Design luminosity**
Efficiency	84.5 ± 0.5%	81.2 ± 0.5%
Fake fraction	6.0 ± 0.1%	15.3 ± 0.1%

Table 6.1: Average tracking efficiency and fake fraction, evaluated on b-tagging samples at both start-up (circles) and design luminosity (triangles).

Then, given the tight cuts applied, even if the asymptotic reconstruction efficiency is not as high as for high p_T isolated electrons, the fake fraction is always very small; the main requirement for b-tagging reconstruction is hence met. Average efficiency and fake fraction values are given in table 6.1.
In order to evaluate, in both luminosity regimes, the impact of primary vertex identification on track reconstruction, figure 6.3 shows the ratio between the overall η tracking efficiency and the one evaluated only on those RoIs where a good primary vertex candidate was identified.

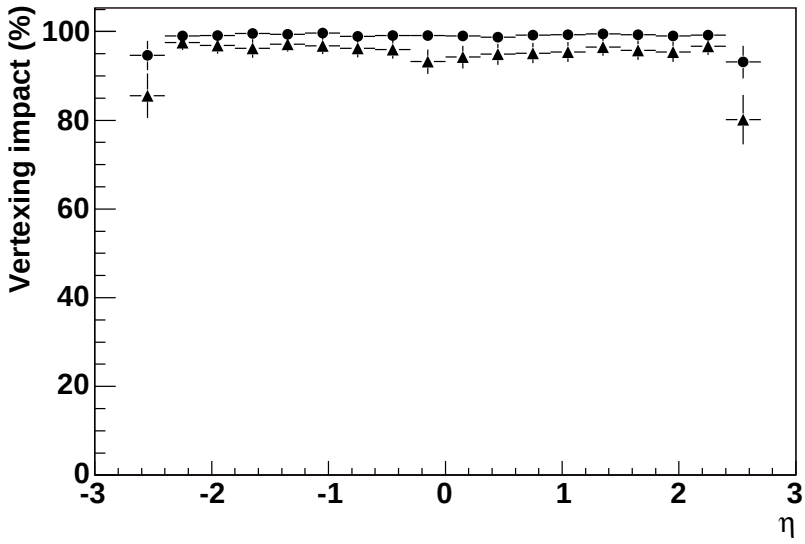

Figure 6.3: Impact of vertex reconstruction on tracking efficiency, as a function of η, at both start-up (circles) and design luminosity (triangles).

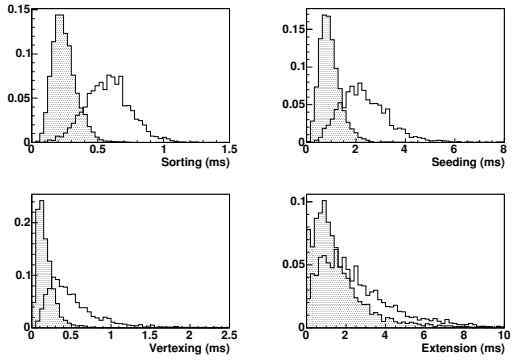

Figure 6.4: Processing time consumed by each algorithm block.

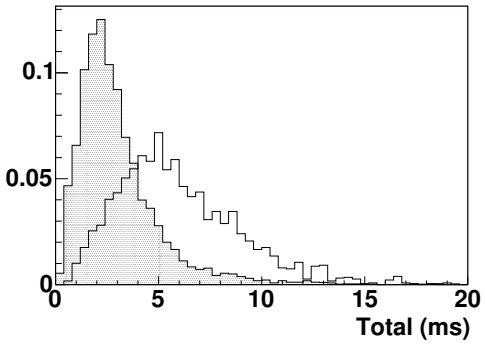

Figure 6.5: Processing time consumed by SiTrack in order to reconstruct the tracks contained in a jet RoI identified at LVL1.

As done for single electron samples, timing measurements have been performed on a 2.4 GHz processor, in order to evaluate the average algorithmic processing time. Figure 6.5 shows the distribution for the time consumed, in both luminosity conditions, processing a jet RoI identified at LVL1; figure 6.4 shows, instead, the contribution of each algorithm block to the overall time.
The average values, given in table 6.2, show that the performance of the SiTrack algorithm

	Start-up luminosity	**Design luminosity**
Sorting (ms)	0.25	0.6
Seeding (ms)	0.95	2.3
Vertexing (ms)	0.18	0.5
Extension (ms)	1.6	2.5
Total (ms)	**3**	**6**

Table 6.2: Timing measurements for jet reconstruction at start-up and design luminosity; the average processing time taken by each reconstruction step is given, along with the average total algorithmic processing time.

meets the requirements posed by the LVL2 environment at both luminosity regimes. Anyway, the algorithm hasn't been yet completely optimized for the reconstruction of jet samples; this is an important topic that will be addressed in the near term, in order to improve the safety margin in case of multi-jet signatures.

6.4 On-line b-tagging

In this section, a LVL2 b-tagging algorithm based on the likelihood-ratio method will be described. As will be pointed out in the following, this method is quite general and can make use of different quantities, in order to separate the signal from the background samples.
So, the description of various discriminating variables will be given, along with the b-tagging performance they provide. Finally, the combined b-tagging performance, obtained merging all these quantities, will be provided in terms of b-jet selection efficiency and rejection power against light quark jets.
All these studies will be described in detail only for the start-up luminosity scenario; results obtained simulating design luminosity conditions will be instead provided in the last section.

6.4.1 The likelihood-ratio method

The likelihood-ratio method is a statistical tool used to separate two or more event classes, and is based on a set of characteristic variables.
The likelihood-ratio variable W is evaluated, for a given event, as the ratio between the probability distributions for two alternative hypotheses. In the application to the b-tagging selection, the likelihood-ratio variable is defined as

$$W = S(s)/S(b),$$

where $S(s)$ and $S(b)$ are the probability densities for the signal, the b-jets, and the background, represented in this case by the u-jets.
This variable is widely used to obtain the best possible separation between signal and background, in terms of a single variable, in fits aimed at extracting the fraction of signal events in a given sample. The same variable can be also directly used, as in the b-jet selection case,

to select the signal events, as an example applying a cut on the likelihood-ratio variable itself. The probability density distributions used in the b-tagging application can be functions of some parameter of each track (e.g. the transverse impact parameter d_0) or of some collective property of the jet (e.g. its track multiplicity). In the first case, these distributions should take the form

$$s(par_1, par_2, par_3, \ldots, par_n),$$
$$b(par_1, par_2, par_3, \ldots, par_n),$$

where the $1, \ldots, n$ indices identify each track belonging to the jet; the corresponding likelihood-ratio variable is thus defined as

$$W = \frac{s(par_1, par_2, par_3, \ldots, par_n)}{b(par_1, par_2, par_3, \ldots, par_n)}$$

Exact evaluation of the s and b functions is very difficult, since it would require an almost infinite amount of simulated data; as a matter of fact, in order to reasonably populate a n-dimensional cube, about 100 entries are needed for each dimension, corresponding to n^{100} tracks; even worse, the number of tracks in a jet is not fixed.
Anyway, if we assume that the variables corresponding to different tracks are independent, the ratio between the overall probability densities is reconducted to the product between the ratios of the single probability densities:

$$W = \prod_{i=1}^{n} \frac{s(par_i)}{b(par_i)},$$

which is much easier to evaluate.
In the b-tagging case, track parameters are correlated in a complicated way; the correlation depends, as a matter of fact, on the proper time for the B hadron and on its decay kinematics. Anyway it can be proved that, neglecting these correlations, no mistake is made; simply, the discriminant power of the W variable will result slightly reduced.
The W variable, can take any value between 0 (for the background) and $+\infty$ (for the signal). For practical reasons, it is useful to handle a variable defined on a finite interval; to achieve this, W is usually replaced by another variable

$$X = \frac{W}{1 + W},$$

which can only range between 0 and 1.
As will be shown in the following, signal events (b-jets) pile-up around $X = 1$, while the background (u-jets) takes values closer to $X = 0$.

6.4.2 On-line b-tagging variables

As said before, different quantities, evaluated on the reconstructed tracks, can be used to build the discriminant variable for the b-tagging selection. In the following, a throughout

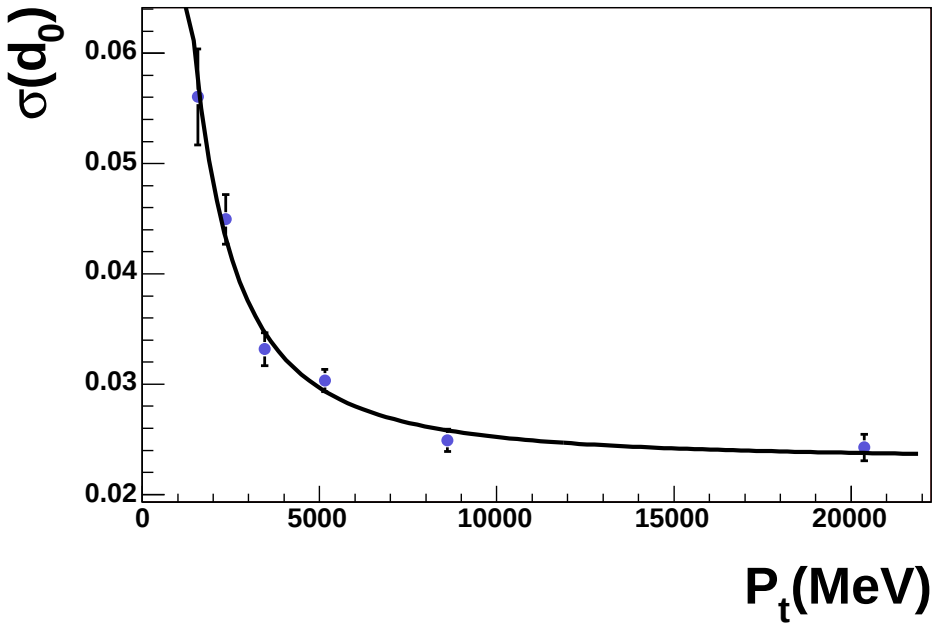

Figure 6.6: Parametrization of the error on d_0 as a function of the corresponding reconstructed p_T value.

review of the most significant choices is given, along with the b-tagging performance they provide. In particular, each method will be characterized, on single jets, by the corresponding b-tagging curve, showing the rejection on u-jets, defined as the inverse of the efficiency on those jets ($R_u = 1/\epsilon_u$), as a function of the efficiency on b-jets (ϵ_b).

Transverse impact parameter

The most natural choice is to build the b-tagging discriminant variable selection exploiting the transverse impact parameter d_0 of the tracks reconstructed by SiTrack. As a matter of fact, since the hadrons containing b-quarks have a finite lifetime, the tracks coming from their decays are characterized by large d_0 values, while tracks coming from u-jets are dominantly coming from the primary vertex ($d_{vtx} = 0$).
In particular, the significance of the transverse impact parameter $S = d_0/\sigma(d_0)$ is used, where $\sigma(d_0)$ is the error on the impact parameter; since the error on d_0 is not defined on the reconstructed track, as three points are fitted by one and only one circle, the uncertainty on the impact parameter has been parametrized as a function of the reconstructed p_T, as shown in figure 6.6. Tests have been performed comparing the results obtained adopting the $S = d_0/\sigma(d_0)$ variable instead of d_0; these have shown that, since the impact parameter divided by its error contains more information, the corresponding b-tagging selection provides

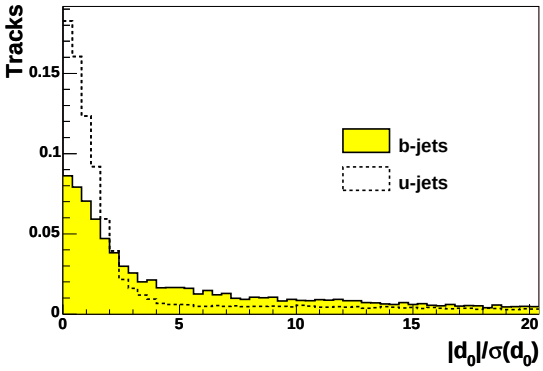

Figure 6.7: Distribution of the transverse impact parameter significance for tracks coming from b-jets (shaded plot) and u-jets (dashed line).

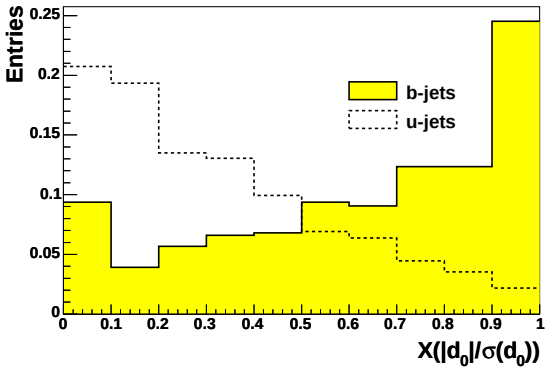

Figure 6.8: Distribution of the discriminant variable X based on transverse impact parameter significance for b-jets (shaded plot) and u-jets (dashed line).

a slightly better performance.
Figures 6.7 and 6.8 respectively show the distributions of the impact parameter significance and the corresponding discriminant variable X for b-jets and u-jets. From these plots it can be guessed that the impact parameter significance is a promising choice for the discriminant variable, since the two distribution are very well separated.
This is confirmed by the corresponding b-tagging curve shown in figure 6.9, where it can be noticed that this method is capable of providing a rejection factor close to 10 even retaining a 50% selection efficiency on b-jets.

Longitudinal impact parameter

The track impact parameter in the RZ plane, i.e. z_0 of the reconstructed tracks, can be adopted to build another discriminant variable for the b-tagging selection.
In analogy with the d_0 impact parameter, the z_0 distribution shows a peak around the primary vertex position (z_{vtx}) for tracks coming from u-jets, while larger values of $z_0 - z_{vtx}$ are expected for b-jets. Anyway, unlike what happens for the transverse impact parameter, no *a priori* knowledge of z_{vtx} is available; this information has hence to be reconstructed, starting from the tracks produced by SiTrack. A simple sliding window approach was adopted, very similar to the one implemented inside SiTrack (see chapter 4), granting a 96% efficiency (94% at design luminosity) and a resolution on z_{vtx} of about 170μm.
After the primary vertex position has been reconstructed, the $z_0 - z_{vtx}$ variable can be applied to the b-tagging selection. Figures 6.11 and 6.12 respectively show the distributions of the longitudinal impact parameter and the corresponding discriminant variable X for b-jets and u-jets. Also in this case the two distributions are pretty different; anyway, from these plots it can be argued that the b-tagging performance will be worse than the one obtained with the transverse impact parameter significance, since in this case the separation between two

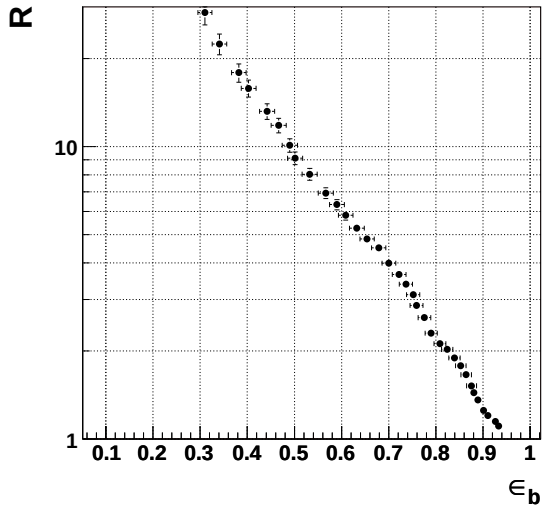

Figure 6.9: Performance of the b-tagging selection based on the d_0 significance discriminant variable.

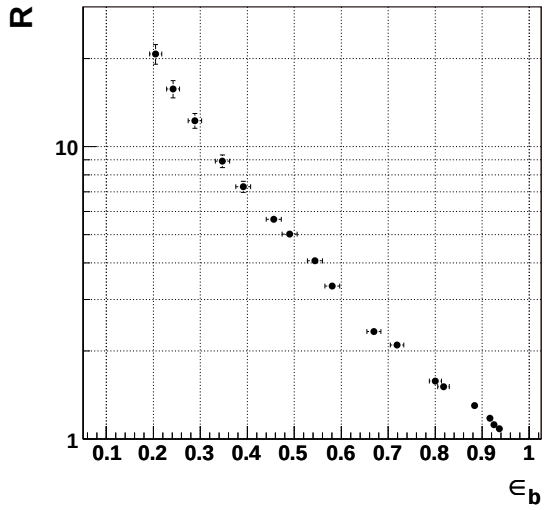

Figure 6.10: Performance of the b-tagging selection based on the z_0 discriminant variable.

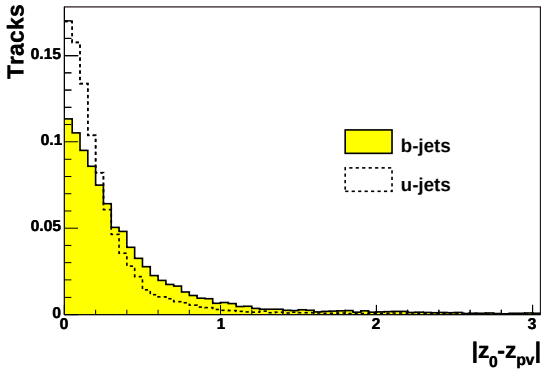

Figure 6.11: Distribution of the longitudinal impact parameter significance for tracks coming from b-jets (shaded plot) and u-jets (dashed line).

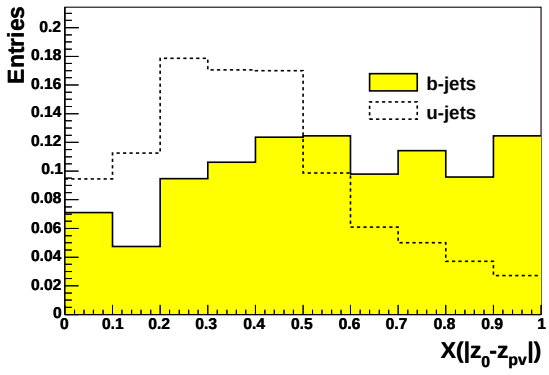

Figure 6.12: Distribution of the discriminant variable X based on longitudinal impact parameter significance for b-jets (shaded plot) and u-jets (dashed line).

distributions is much less sharp.
This guess is confirmed by looking at the b-tagging curve shown in figure 6.10; in this case, for 50% b-jet efficiency a rejection factor close to 5 is obtained, which is a factor of two lower than the one obtained using d_0. Anyway, since the correlation between the two impact parameters of a given track is expected not to be complete, the combination of the two

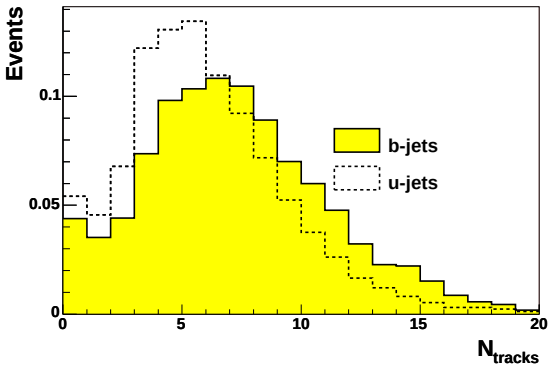

Figure 6.13: Distribution of the reconstructed track multiplicity inside the RoIs coming from b-jets (shaded plot) and u-jets (dashed line).

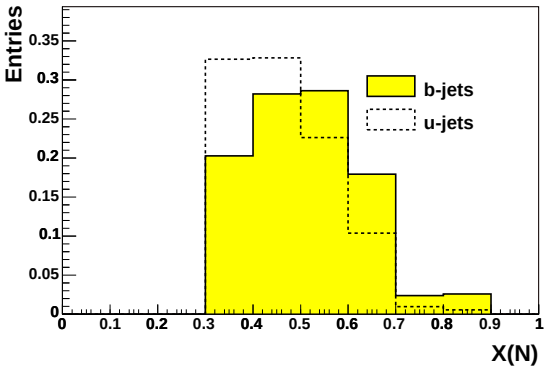

Figure 6.14: Distribution of the discriminant variable X based on the reconstructed track multiplicity inside the RoIs coming from b-jets (shaded plot) and u-jets (dashed line).

methods presented so far, which will be covered in next section, looks very promising.

Track multiplicity

Moving to variables collectively characterizing the reconstructed jets, the first one studied is the average track multiplicity in the jet RoI.
It must be noticed that, for methods based on individual track parameters, the transformation from the original variable to the discriminant one has the main role of combining information coming from different sources. In this case, as for all the collective jet variables, no combination is needed; anyway the transformation to the discriminant variable still plays a fundamental role, since it has the effect of reshaping the variable distribution so that signal and background accumulate toward the opposite ends of the interval. This way, the desired b-tagging working point can be selected moving a single cut between 0 and 1.
Figures 6.13 and 6.14 respectively show the distributions of the average track multiplicity and the corresponding discriminant variable X for b-jets and u-jets.
From these plots it is clear that, even if the two distributions are quite different, the impact of track multiplicity on b-tagging selection cannot be as important as the ones discussed above. As a matter of fact, figure 6.15 shows that, as an example, 50% b-jet efficiency corresponds to a rejection factor below 3.
Even if this result is rather poor, it is worth to try combining this variable with the others mentioned above, since the correlation between them should be negligible; this will be done in next section.

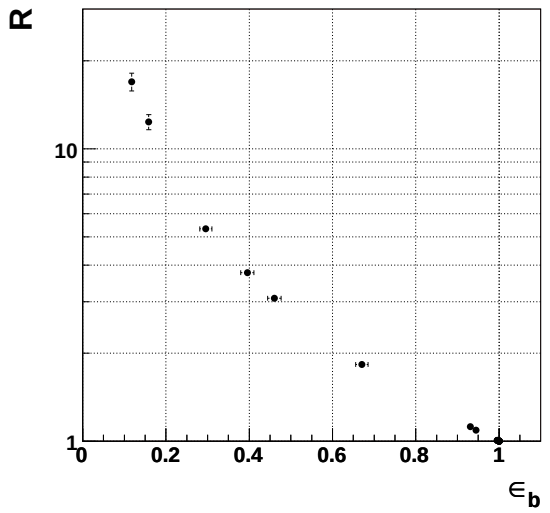

Figure 6.15: Performance of the b-tagging selection based on the track multiplicity discriminant variable.

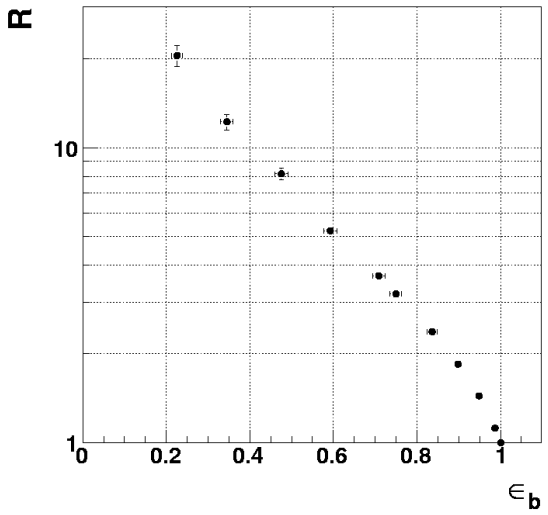

Figure 6.16: Performance of the b-tagging selection based on the jet energy discriminant variable.

Jet energy

A variable related to the jet energy can be defined as

$$E = \sum_{i=1}^{N_{trk}} \frac{E_i \, f(d_0/\sigma)}{E_{tot}},$$

where E_i is the energy of each reconstructed track, evaluated as if the corresponding particle was massless, $f(d_0/\sigma)$ is the transverse impact parameter likelihood-ratio variable and the sum runs on all the tracks inside a given RoI. Since $f(d_0/\sigma)$ is close to 0 for tracks from the primary vertex and ~ 1 for tracks from secondary vertexes, E roughly corresponds to the fraction of jet energy carried by tracks coming from a secondary vertex; so, E is expected to reach higher values for b-jets than for u-jets.
This quantity has been studied as a possible discriminating variable for the b-tagging selection; figures 6.17 and 6.18 show the distributions of the jet energy and the corresponding discriminant variable X for b-jets and u-jets.
It is immediately evident that E can provide a good b-tagging discriminant variable, as proved by the corresponding b-tagging curve shown in figure 6.16.
Anyway, since E is strongly correlated with the discriminant variable based on d_0, it is expected that its power will be diluted in case the two methods are combined.

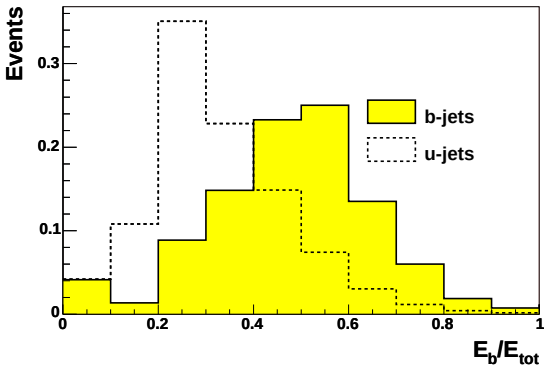

Figure 6.17: Distribution of the reconstructed jet energy for b-jets (shaded plot) and u-jets (dashed line).

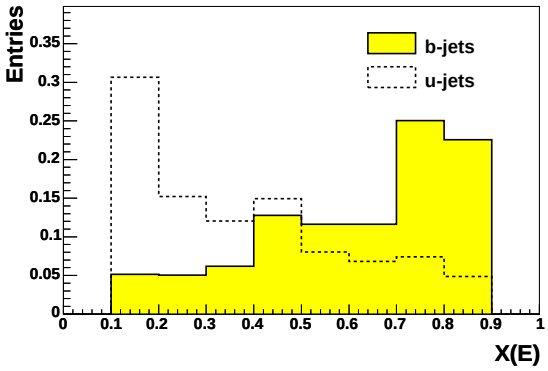

Figure 6.18: Distribution of the discriminant variable X based on the reconstructed jet energy for b-jets (shaded plot) and u-jets (dashed line).

Invariant mass

Invariant mass b-jets can be distinguished from u-jets by computing the invariant mass of the B hadron:

$$M = \sqrt{E^2 - P^2}$$

where E and P are the energy and the momentum of the B hadron respectively. The method has many limitations both from the physics and from the reconstruction point of view: the nominal B hadron masses (above 5000 MeV) can be correctly reconstructed only in few decay states and the precision of the invariant mass determination depends strongly on the tracking efficiency and resolution. Moreover the charged tracks reconstructed in a b-jet RoI come both from the B hadron decay and from the fragmentation process: it is then important to discriminate between the two types of tracks. Using the weight $w = f(d_0/\sigma)$ defined in the previous section the energy and the momentum vector of the B hadron has been estimated as

$$E = \sum_{i=1}^{N_{trk}} w_i e \ , \qquad P_x = \sum_{i=1}^{N_{trk}} w_i p_{x\,i} \ , \qquad P_y = \sum_{i=1}^{N_{trk}} w_i p_{y_i} \ , \qquad P_z = \sum_{i=1}^{N_{trk}} w_i p_{z\,i} \ ,$$

where the track energy has been computed, assuming the pion mass, from the absolute value of the reconstructed momentum.
Figures 6.19 and 6.20 show respectively the distributions of the invariant mass and the corresponding discriminant variable X for b-jets and u-jets. The original mass difference between B hadron ($\sim$ 5000 MeV) and light hadron ($\leq$ 1000 MeV) has been largely reduced by the effects previously discussed ending up to a very modest rejection power, shown in 6.21, comparable to the one found using the track multiplicity variable.
All the variable related to the B hadron properties (track multiplicity, energy and invariant mass) will benefit from a secondary vertex finding algorithm allowing to identify the tracks

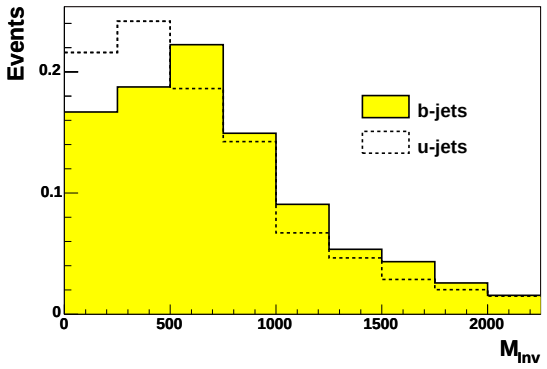

Figure 6.19: Distribution of the reconstructed invariant mass for b-jets (shaded plot) and u-jets (dashed line).

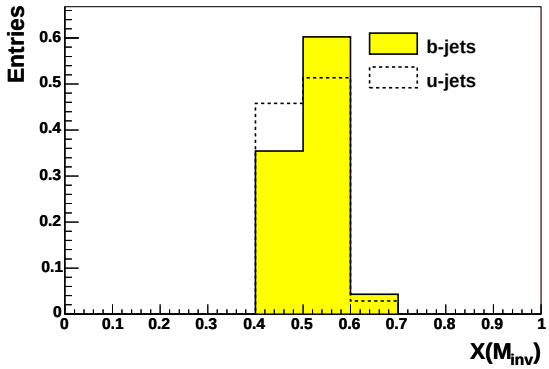

Figure 6.20: Distribution of the discriminant variable X based on the reconstructed jet invariant mass for b-jets (shaded plot) and u-jets (dashed line).

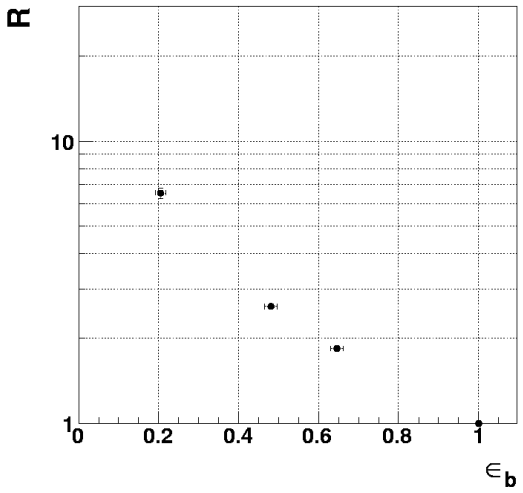

Figure 6.21: Performance of the b-tagging selection based on the invariant mass discriminant variable.

issued from the b decay. Precise vertex reconstruction will probably require to refine the track resolution and to estimate reliable errors on the track parameters.

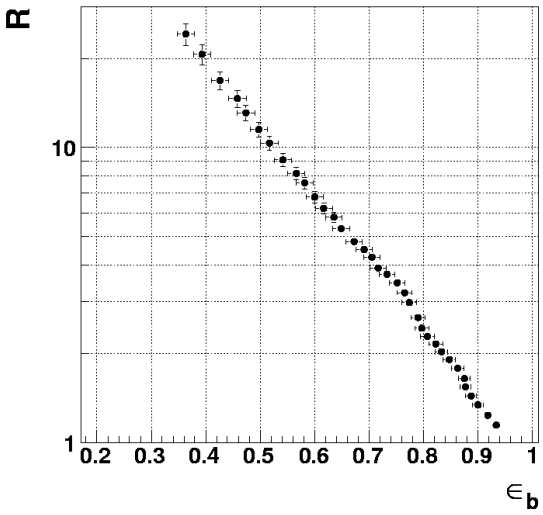

Figure 6.22: Performance of the b-tagging selection based on the two-dimensional combination of d_0 significance and z_0 discriminant variables.

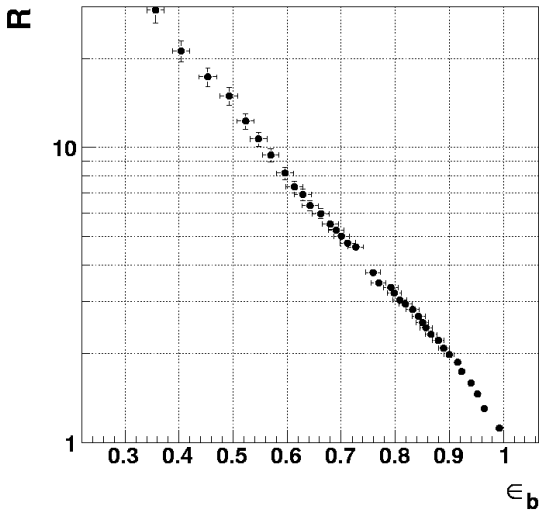

Figure 6.23: Performance of the b-tagging selection obtained combining all the discriminant variables: d_0 significance, z_0, track multiplicity, jet energy and invariant mass.

6.4.3 Combined on line b-tagging performance

In this section the combination of the methods analyzed so far will be treated.
In principle, the best way to combine n different discriminant variables would be to build an n-dimensional discriminant function. This method would provide the best results, since it correctly takes into account the correlation between the variables; anyway, it is practically unfeasible for $n > 2$, given the high number of tuning tracks that would be needed to reasonably populate the corresponding n-dimensional histogram.
Another possibility is that of using the product of the n discriminant functions based on single variables; this method has the disadvantage of discarding correlations between variables, but can be easily applied to an infinite number of variables.
The first and more precise approach will be applied to the two most effective variables: the transverse and longitudinal impact parameters. The resulting b-tagging curve is given in figure 6.22. The combination of all the methods discussed so far, requiring in principle to handle a fifth-dimensional discriminant function, has to be obtained using the product of the single variable discriminant functions (except for the impact parameters). The results are shown in figure 6.23.
It can be noticed that the addition of the discriminant variables characterizing the reconstructed jet improve significantly the rejection only at high b-jet efficiency.

6.4.4 On-line b-tagging at design luminosity

All the results described so far have been obtained on datasets for which the start-up luminosity conditions (2×10^{33} cm^{-2} s^{-1}) were simulated. The same studies have also been repeated on samples containing exactly the same hard processes, mixed with an average of $\sim$23 pile-up interactions per event, to reproduce the operating conditions at high luminosity (1×10^{34} cm^{-2} s^{-1}).
The comparison between the two luminosity conditions is very important, since it provides a way to test the robustness of both the track reconstruction at LVL2 and the b-tagging algorithm. Furthermore, since the b-tagging selection is crucial for many channels with a significant discovery potential, it is important to prove that it can be an effective trigger ingredient also at design luminosity.
In the section on tracking performance, the comparison between the two luminosity regimes was already discussed, showing that little difference is expected for the tracking efficiency, while the fake fraction is almost doubled, even if always below 15%. So, as expected, the the methods based on the transverse impact parameter mantains the same performance. The discriminant power of the variable based on longitudinal impact parameter is, on its turn, partly spoiled by the lower primary vertex efficiency in the first stage of the reconstruction but, since the performance for the a posteriori vertex remains stable, the final performance are only slightly degraded. The variables characterizing the reconstructed jet maintain their modest rejection powers.
The results obtained from the study of b-tagging performance at design luminosity are summarized in the curve shown in figure 6.24, where it is compared with the one corresponding to start-up conditions showing that, within the present uncertainty, the two rejections in the two luminosity regimes are compatible.

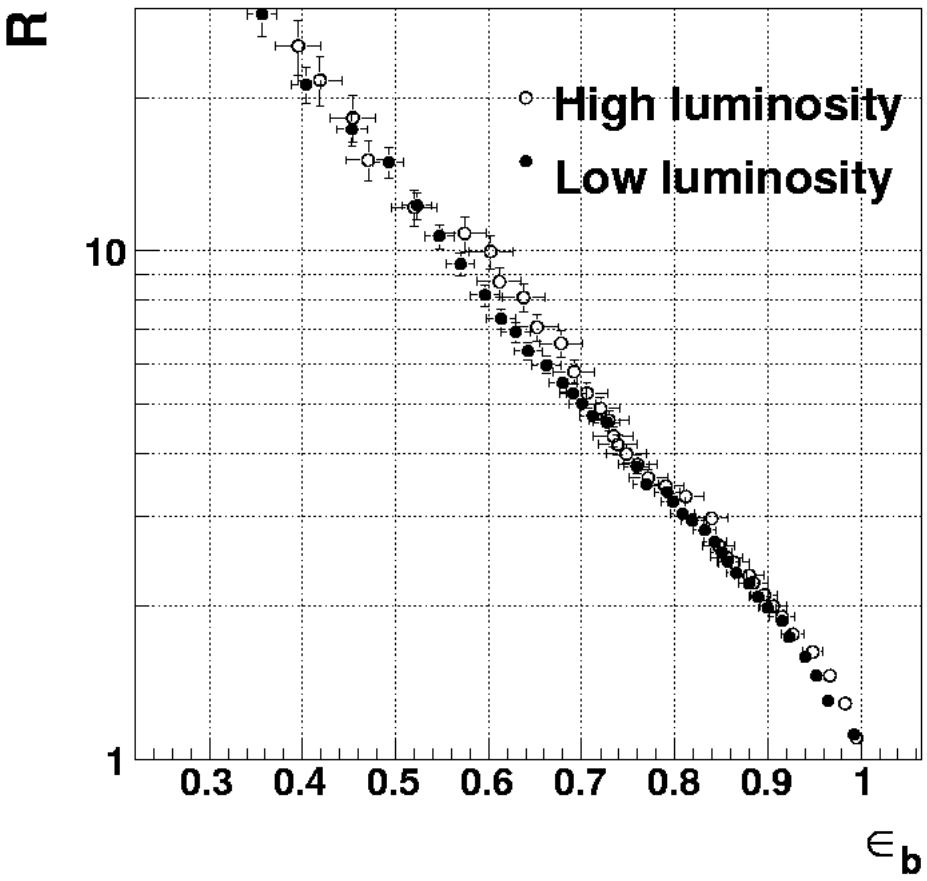

Figure 6.24: Performance of the b-tagging selection obtained combining all the discriminant variables: d_0 significance, z_0, track multiplicity, jet energy and invariant mass.

Chapter 7

Application to the B-Physics Trigger

7.1 B-physics trigger strategy

In this chapter, the B-physics trigger strategy currently foreseen by the ATLAS experiment [49] will be reviewed.
The semi-inclusive selection of $D_s^{\pm} \rightarrow \phi\ \pi^{\pm}$ decays will be discussed in more detail. In particular, the application of the SiTrack algorithm to this selection at LVL2 will be studied in terms of efficiency and trigger rates, and the results will be used to evaluate the impact of this selection scheme to the Δm_s measurement in ATLAS.

7.1.1 Strategies for the different luminosity regimes

The ATLAS experiment was recently posed some new constraints regarding the B-physics studies programme:

- the target luminosity value of 2×10^{33} cm^{-2} s^{-1} was proposed for the early phases of LHC operation; since this value is twice higher than the one originally foreseen for the reduced luminosity period, an improved rejection power is needed for each selection stage, in order to avoid filling the trigger bandwidth with fake candidate events;

- due to economic considerations, the T/DAQ system will be descoped both in terms of network bandwidth and computing power, at least in the first data-taking period; this means that the amount of trigger menu budget devoted to B-physics will be reduced accordingly; at the same time, the limited available computing power poses very strong timing constraints on the selection algorithms;

- again, due to budget constraints, a staged detector geometry was proposed for the start-up phase; this choice would, as an example, affect the online tracking reconstruction, crucial for the B-physics trigger; the online reconstruction algorithms, used as ingredients for the online selections, will thus have to be proven efficient also in this

scenario; even though it is very probable, given the present construction status, to have all the relevant detectors (in particular the pixel detector) ready at the start up.

As a result of the limitations described above the B-physics trigger will (in the current baseline trigger strategy) rely on only di-muon based selections, at the peak initial luminosity of 2×10^{33} cm^{-2} s^{-1}, as well as in the design luminosity regime In this scheme, muons passing a threshold around 6 GeV at LVL1, will be further confirmed at LVL2 and at the EF, exploiting the precise muon chamber and calorimeter measurements and extrapolating them to the Inner Detector tracking system. The di-muon selection is well suited for the identification of a set of specific exclusive and semi-inclusive decays, such as B mesons decaying to $J/\Psi \to \mu^+\mu^-$ and $B_{d,s} \to \mu^+\mu^-(X)$, but doesn't cover many other interesting channels, originally foreseen in the ATLAS physics programme.
So, as the luminosity falls to values below around 2×10^{33} cm^{-2} s^{-1}, further trigger selections, devoted to B-physics studies will be added; these additional selections are based on a single muon trigger, plus one or more calorimeter trigger objects. This way it will be possible to perform a semi-inclusive reconstruction of decay candidates such as $J/\Psi \to e^+e^-$, $B \to h^+h^-$ and $D_s^\pm \to \phi\,\pi^\pm$. In all these additional triggers, the reconstruction of the LVL1 muon will be refined at the HLT, as already described for the di-muon case. Anyway, it is still not decided whether the HLT reconstruction will be performed in the usual RoI-guided mode or in the so called full-scan mode, described below.
RoI-guided reconstruction, currently considered the baseline option, simply foresees the application of the standard ATLAS HLT architecture to the B-physics sector. In this scenario, low E_T electromagnetic and jet RoIs identified at LVL1 are used, at the HLT, to perform track reconstruction in the ID; and then the invariant mass and topological cuts specific to the selected decays can be applied.
The full-scan approach, on the other hand, doesn't use the RoIs to search for B-decay products and, instead, performs track reconstruction in the full acceptance of the Silicon detectors for events with a single muon trigger. This strategy, even although more efficient than the one based on RoI reconstruction, requires a significantly higher computing power and could thus lead to lower signal selection rates. On the other side, the RoI-based approach needs a careful tuning of the LVL1 threshold and of the sizes in η and ϕ for the ID region analyzed at the HLT, in order to maintain a reasonable selection efficiency level. In next sections, this problem will be directly addressed for the $D_s^\pm \to \phi\,\pi^\pm$ decays.

7.1.2 Estimation of the trigger rates

Preliminary studies have been carried out to provide estimates of the trigger rates expected in the RoI guided scenario described in previous subsection. The LVL1 muon trigger, used in its low-p_T configuration, is based on data from the two inner RPC layers in the barrel region and on the two outer TGC stations for the endcap. The main background for the single muon trigger object comes from in decays in flight of π and K mesons; these can be reduced at the HLT by requiring that the muon detector measurements match a track reconstructed in the ID after applying a compatibility test between the two independently determined p_T values. Furthermore, since the prompt-muon cross section rapidly decreases with increasing muon momenta, the single muon trigger rate should be easily controlled by tuning the LVL1

	2×10^{33} cm^{-2} s^{-1}		1×10^{33} cm^{-2} s^{-1}	
HLT stage	**LVL2**	**EF**	**LVL2**	**EF**
$B_{d,s} \to \mu^+\mu^-(X)$	200 Hz	*small*	100 Hz	*small*
$J/\Psi \to \mu^+\mu^-$		10 Hz		5 Hz
$D_s^\pm \to \phi\,\pi^\pm$	-	-	60 Hz	9 Hz
$B \to \pi^+\pi^-$	-	-	20 Hz	3 Hz
$J/\Psi \to e^+e^-$	-	-	10 Hz	2 Hz
Total	200 Hz	10 Hz	190 Hz	20 Hz

Table 7.1: Estimated output rates of the HLT selection for the different signatures selected by the ATLAS B-physics trigger.

threshold but with a corresponding loss of efficiency. In particular, simulations show that a single muon trigger rate of ~ 20 kHz is expected at 1×10^{33} cm^{-2} s^{-1}, if a 6 GeV threshold is applied at LVL1.
For di-muon triggers, even lower thresholds should be accessible; as a matter of fact, applying a 6 GeV threshold, the double muon trigger should have a rate below 1 kHz. In this case, the main physical background are heavy-flavour decays. As in the single muon trigger, candidates identified at LVL1 are then confirmed or rejected at the HLT, requiring the matching with ID tracks.
For the EM and jet triggers, needed to complete the B-physics signatures for the lower luminosity scenario, the most important quantities are the average RoI multiplicity and the efficiency with respect to the decay products to be selected. The RoI multiplicity is a particularly relevant quantity for LVL2 processing, since, along with the size of each RoI, it determines the fraction of the detector that must be read out in order to perform the B-trigger selection and hence the execution time. Studies, based on fast simulations of the LVL1 calorimeter trigger, have been performed on $b\bar{b}$ samples containing at least one muon with $p_T > 6$ GeV [50]; these show that, on average, two jet and one EM RoI are identified if a LVL1 E_T thresholds of 5 GeV and 2 GeV respectively are applied in the jets and EM trigger algorithms/selections. However these results need to be confirmed using a full simulation of the LVL1. In the following, the specific case of $D_s^\pm \to \phi\,\pi^\pm$ decays will be covered, using fully simulated data.
The selection efficiency of the RoI mechanism is strongly related to the size of the RoIs themselves; studies have been performed on $J/\Psi \to e^+e^-$ and $D_s^\pm \to \phi\,\pi^\pm$ decays, evaluating the average distance of the decay products from their mother particle in both η and ϕ directions. These showed that, in both cases, an RoI width of $\Delta\eta \times \Delta\phi = 1 \times 1.5$, corresponding approximately to 7% of the ID region, should be sufficient to grant a almost full efficiency. More details will be given in the next sections, where the reconstruction of the $B_s \to D_s^\pm \to \phi\,\pi^\pm$ decay will be treated. Summarizing, the estimated HLT rates for the signatures mentioned/discussed above are given in table 7.1, along with the total B-physics output rates in the two luminosity scenarios discussed.

7.1.3 Selection of the semi-inclusive $D_s^{\pm} \to \phi\,\pi^{\pm}$ decays

As already mentioned, the semi-inclusive selection of $D_s^{\pm} \to \phi\,\pi^{\pm}$ decays is based on a single muon trigger, with the additional demand for a jet cluster with E_T exceeding 5 GeV. In case the RoI-guided approach is adopted for track reconstruction at LVL2, a preliminary evaluation of the geometrical selection efficiency suggests the use of an RoI width of $\Delta\eta \times \Delta\phi = 1 \times 1.5$.
Some further constraints on the selection performance for this channel come from the offline analyses, which require that the trigger:

- has good efficiency for decays in which the three final-state daughters (K^+, K^-, π) have $p_T > 1.5$ GeV;
- reconstructs ϕ^0 candidates from two oppositely charged tracks in a relatively large mass window around the nominal ϕ^0 mass;
- reconstructs D_s candidates from two tracks which pass the ϕ^0 selection and a third track in a relatively large mass window around the nominal D_s mass.

For the exclusive $B_s \to D_s\pi$ selection, additional constraints are:

- good reconstruction efficiency for the π track combined to the three D_s products for $p_T > 1$ GeV;
- reconstruction of B_s candidates from the three tracks which pass the D_s selection and a fourth track in a relatively large mass window around the nominal B_s mass;
- good B_s reconstruction efficiency for $p_T(B_s) > 10$ GeV, corresponding to the cut applied for offline sample preselection.

In next section all these trigger configuration details will be reviewed, using fully simulated $B_s \to D_s \to \phi\,\pi$ samples and the complete description of the LVL1 calorimeter algorithm selecting the jet RoI.
Once the trigger selections have been fully specified, the corresponding track reconstruction performance for the SiTrack algorithm will be studied. Finally, in the last section, tracks reconstructed at LVL2 will be used to tune exclusive and semi-inclusive selections for B meson decays including D_s in the final state, exploiting both kinematical and topological cuts; the impact of this trigger scheme on the measurement of Δm_s will be then discussed.

7.2 Trigger configuration for $B_s \to D_s \to \phi\,\pi$ decays

In this section, the configuration of the LVL1 and LVL2 parameters for the selection of exclusive $B_s \to D_s \to \phi\,\pi$ decays will be discussed.
Once a viable solution will be obtained, the corresponding tracking performance for the SiTrack algorithm will be studied.

7.2.1 Data samples used

All the studies presented in this chapter are based on signal channel samples containing the $B_s \to D_s\,\pi,\ \ D_s \to \phi\,\pi,\ \ \phi \to K^+K^-$ decay chain, where a muon with p_T exceeding 6 GeV is produced in the decay of the other b hadron.
The background samples used contains instead $b\bar{b}$ events where one b-hadron decays to $\mu\,X$ where $p_T(\mu) > 6$ GeV.
Both signal and background events are then mixed, on average, with 4.6 pileup interactions, to simulate the luminosity condition corresponding to 2×10^{33} cm^{-2} s^{-1}. It must be noticed that this working condition corresponds the upper end of the luminosity range in which this trigger will be used; for this reason the results obtained with the this background sample have to be considered as conservative estimates. Furthermore, the staged version of the ID is simulated in these datasets; this, as mentioned in chapter 2, means that the second pixel layer is missing in both the barrel and the endcap regions and that the TRT has a reduced η acceptance.

7.2.2 LVL1 configuration

In this section, the LVL1 jet RoI mechanism will be studied and tuned on the signal sample, starting from the 5 GeV threshold value suggested by preliminary studies. In particular, the dependence of the LVL1 jet RoI multiplicity and of the selection efficiency from the chosen threshold will be studied.

Jet RoI multiplicity

In figure 7.1, the average LVL1 jet RoI multiplicity is plotted as a function of the LVL1 E_T threshold applied. These results clearly show that the average number of RoIs per event drops as the LVL1 threshold is increased; in particular, the average multiplicity values obtained for reconstructed E_T values exceeding 5, 6 and 10 GeV are given in table 7.2.

	$E_T > 5$ GeV	$E_T > 6$ GeV	$E_T > 10$ GeV
Multiplicity	3.7	2.9	1.4

Table 7.2: Average LVL1 jet RoI multiplicity for different LVL1 E_T thresholds.

Obviously, from the LVL2 processing point of view, the best choice would be to increase the E_T threshold until a mean multiplicity around 1 is reached in order to get a significant advantages compared to the full scan approach where the whole event is read out. However a drop in the B_s selection efficiency is expected as the LVL1 threshold is increased. An indication of this is shown in, again looking at] figure 7.1 by the fact that the bin containing the number of events where no RoI is reconstructed keeps growing as the E_T threshold is moved from 5 to 10 GeV. A more detailed estimation of the selection performance must be thus provided, in order to find a trade-off between multiplicity and efficiency.

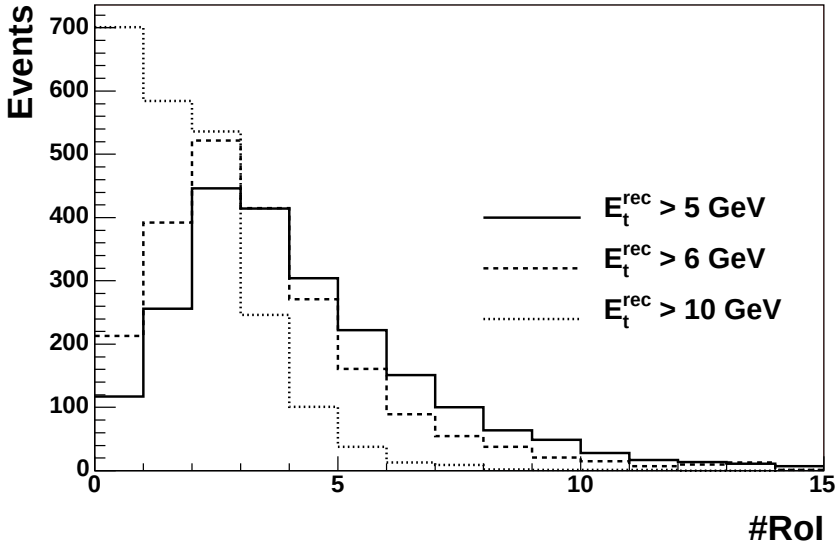

Figure 7.1: LVL1 jet RoI multiplicity for different LVL1 E_T thresholds.

Jet RoI matching efficiency

To evaluate the dependence of the selection efficiency from the LVL1 E_T threshold, we define an RoI as matching the generated B_s if its direction is contained within a $\Delta\eta \times \Delta\phi = 1.5 \times 1.5$ region around the RoI center, as suggested by preliminary studies based on fast calorimeter simulations. The matching efficiency is then defined as the percentage of events where at least one jet RoI is found matching the B_s.
In figure 7.2, the p_T distribution of the B_s hadrons matching the jet RoIs is compared, for three different LVL1 E_T thresholds, with that of the original B_s sample; the corresponding matching efficiencies are plotted, in figure 7.3, as a function of the transverse momentum of the B_s hadron; all the plots shown in the following are normalized to the offline request of p_T >1.5 GeV for all the decay products.
Looking at figure 7.3, it can be noticed that increasing the LVL1 threshold from 5 to 6 GeV results in an efficiency drop of more than 10% for B_s hadrons having a transverse momentum below 25 GeV; the matching efficiency is dramatically decreased for even higher E_T thresholds.

Choice of LVL1 parameters

Summarizing the results obtained so far, the best choice for the E_T LVL1 threshold seems to be 5 GeV, coinciding with the one pointed out by the preliminary studies based on a fast simulation of the calorimeters.
As a matter of fact, higher thresholds would be too inefficient in identifying the B_s direction

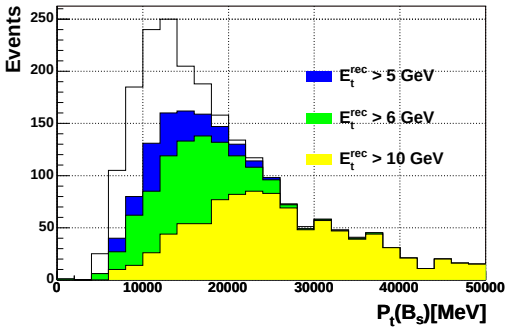

Figure 7.2: Distribution of the transverse momentum for the B_s hadrons matching the jet RoIs produced applying 5, 6 and 10 GeV LVL1 E_T thresholds; the p_T distribution for the unbiased B_s sample is also shown.

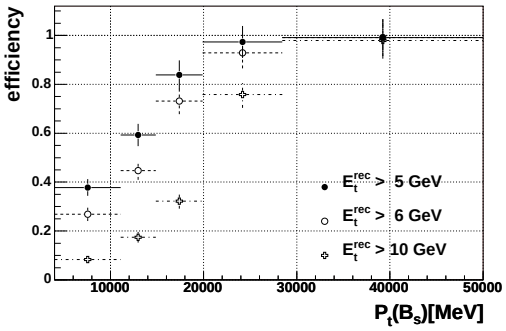

Figure 7.3: Jet RoI to B_s hadron matching efficiency, as a function of its transverse momentum; the result obtained for three different LVL1 E_T thresholds (5, 6 and 10 GeV) are reported.

and would strongly bias the transverse momentum distribution for the selected B_s hadrons. At the same time, the average RoI multiplicity is already quite high if a 5 GeV threshold is applied on the reconstructed transverse energy. This means that it is impossible to increase the selection efficiency by lowering the E_T threshold, since this would result in an unacceptably high number of RoIs produced for each event, and in the processing of an amount of data almost compatible with the full-scan option.

7.2.3 LVL2 tracking configuration

Once the LVL1 threshold on reconstructed transverse energy has been established, the optimal geometrical acceptance of the jet RoIs has to be decided. As already mentioned, this is an important quantity, since it is related to both the selection efficiency for the B_s decay products and to the amount of data processed, on average, for each event.
In the last subsection, the SiTrack configuration adapted to the staged detector scenario will be then discussed.

LVL2 RoI size optimization

Figures 7.4 and 7.5 respectively show the distance in η and ϕ between the center of the RoI that best matches the B_s and the B_s decay product which is farther away from the center of the RoI itself. As in previous section, the plots shown in the following are filled only for the events matching the offline requirements, among which the most relevant for this study is the 1.5 GeV p_T cut on the decay products.
The cuts applied to those distributions have been chosen taking into account their impact on the corresponding selection efficiency. Since the loss of one single B_s decay product means losing the possibility to reconstruct the corresponding event, the signal selection efficiency can be roughly evaluated as the percentage of events passing a particular cut. In table 7.3

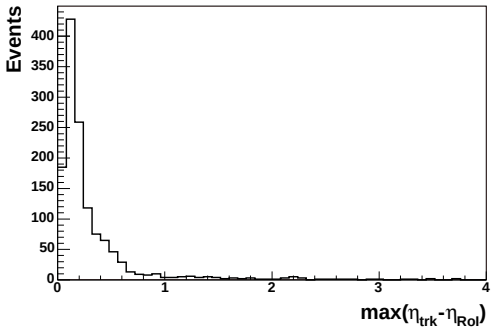

Figure 7.4: Maximum η distance between the B_s decay products and the center of the best matching RoI.

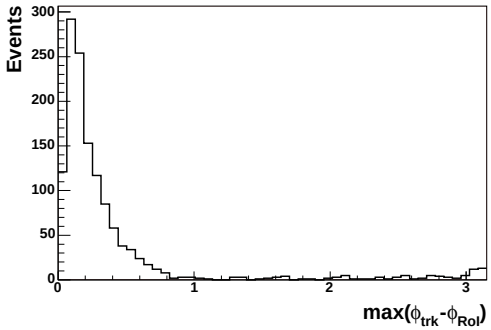

Figure 7.5: Maximum ϕ distance between the B_s decay products and the center of the best matching RoI.

the efficiency estimation corresponding to three different cuts is reported for both η and ϕ.

	Δ(trk-RoI)<0.5	Δ(trk-RoI)<0.75	Δ(trk-RoI)<1.0
η efficiency	86%	93%	95%
ϕ efficiency	85%	92%	93%

Table 7.3: Estimated selection efficiencies for three different η and ϕ RoI sizes.

Looking at these values, the best choice seems to be Δ(trk-RoI)<0.75, which corresponds to an RoI region of $\Delta\eta \times \Delta\phi = 1.5 \times 1.5$, very similar to the one pointed out by preliminary studies based on fast simulation; the corresponding impact on the transverse momentum distribution for the B_s hadrons is shown in figure 7.6. This choice is also confirmed by figure 7.7, where the selection efficiency is plotted, as a function of the B_s transverse momentum, for the three different cuts, applied to both η and ϕ.

As a matter of fact, the cut at 1.0, compared with the one at 0.75, grants a modest gain in efficiency (almost always below 5%) at the cost of having to process an almost double size RoI. On the contrary, the cut at 0.5, while leading to an interesting reduction of processed data, causes a significant loss in efficiency.
As a final consideration, it can be noticed that the asymptotic selection efficiency shown in figure 7.7 is more than 5% higher than what expected multiplying the efficiencies of the two separate η and ϕ cuts, clearly pointing to a correlation between the two variables.
In conclusion, combining the LVL1 E_T threshold and the LVL2 RoI size discussed above, the overall selection efficiency, integrated over p_T of the B_s hadron, corresponds to 80% with respect to the B_s sample meeting the offline requirements. The amount of data processed at LVL2 for each event can be easily evaluated too; since one $\Delta\eta\times\Delta\phi = 1.5\times1.5$ RoI corresponds approximately to 7% of the entire event and given the average jet RoI multiplicity produced by a E_T threshold of 5 GeV, it is foreseen that with this trigger configuration 27% of each event will be processed, on average, at LVL2. It must be noticed, however, that this value

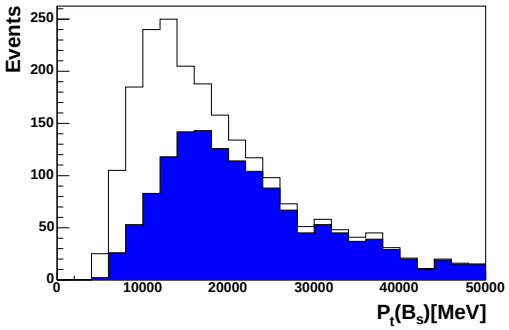

Figure 7.6: Distribution of the transverse momentum for the B_s hadrons whose decay products matching a jet RoI within a $\Delta\eta \times \Delta\phi = 1.5 \times 1.5$ region; the p_T distribution for the raw B_s sample π, K $p_T > 0.5$ GeV is also shown.

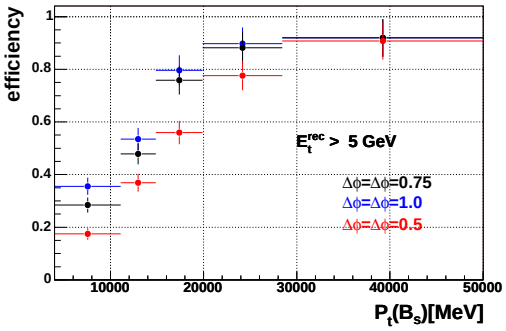

Figure 7.7: B_s decay products selection efficiency, as a function of its transverse momentum; the behaviour of three different cuts on η and ϕ, 0.5, 0.75 and 1.0, is compared.

will be reduced slightly by the partial overlap of RoI.

SiTrack configuration for the staged scenario

As mentioned before, the data samples used in the studies presented here have been simulated using a detector simulation corresponds to the initial staged scenario. This has a major impact on the configuration adopted for track reconstruction with SiTrack, since the space points from an entire Pixel detector layer, the intermediate one, are missing. As a consequence, the logical layer configuration adopted inside SiTrack differs significantly from the ones described in the previous chapters; furthermore, a set of maps adapted to the staged scenario have to be used in this case. In particular, although the seeding process still combines the B-layer with two further logical layers, this time the requirement of picking the second space point in the Pixel detector has to be removed, otherwise there would be no layer redundancy in the barrel region. This choice, although increasing the robustness against detector inefficiencies, has the drawback of leading to a worse seed resolution on z_0, hence decreasing the primary vertex reconstruction efficiency. As in the b-tagging application, the seeds are then extended with SCT space points from two further logical layers.
Since the offline selection requires the best possible tracking efficiency down to $p_T \sim 1.5$ GeV, the cuts on ϕ_{12}, d_{12} and d_3 have been tuned on Monte Carlo tracks with simulated transverse momentum exceeding 1.5 GeV. This time, looser cuts have been applied to the other variables; as a matter of fact, in order to correctly tag a signal event, it is crucial to reconstruct all the decay products of the meson to be tagged (D_s or B_s). This means that an higher efficiency has to be preferred to a very low fake fraction.
Another difference, with respect to the tuning adopted for the b-tagging, is in the cuts applied in the for primary vertex reconstruction. First of all a wider sliding window (2 mm) has been used; secondly since the signal is characterized by lower p_t values, the d_{12} selection for

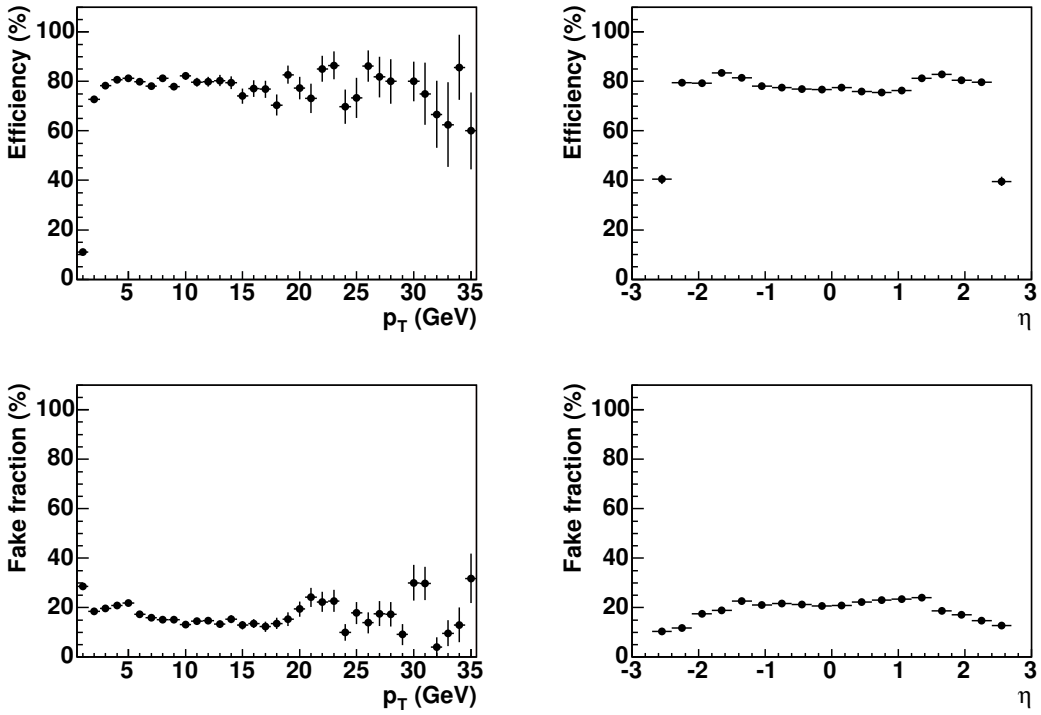

Figure 7.8: Tracking performance on $B_s \to D_s^{\pm} \to \phi\, \pi^{\pm}$ samples. The upper two plots show the tracking efficiency as a function of p_T and η; in particular, the efficiency quoted in the left plot refers to tracks having a $p_T > 1.5$ GeV. The lower two plots show the fake fraction, as a function of p_T and η.

the vertexing histogram had to be loosened. This could cause a degradation of the vertexing performance, since a larger fraction of fake seeds is allowed to enter the vertexing histogram.

7.2.4 LVL2 track reconstruction performance

In this section, the selection performance results using the tuning described above are presented. All the plots presented here have been produced using signal samples containing $B_s \to D_s^{\pm} \to \phi\, \pi^{\pm}$ decays.
Figure 7.8 shows the reconstruction efficiency and the fake fraction, as a function of p_T and η of the simulated tracks; in the η plot, the efficiency is evaluated for tracks having generated $p_T > 1.5$ GeV.
At first sight, the results look very similar to those obtained in the b-tagging chapter; although an evident efficiency drop is present in the barrel η region. This can be easily explained by looking at figure 7.9 where the impact of vertexing performance on track reconstruction is shown.
First of all, the average vertexing efficiency is significantly lower (around 88.5%) than the

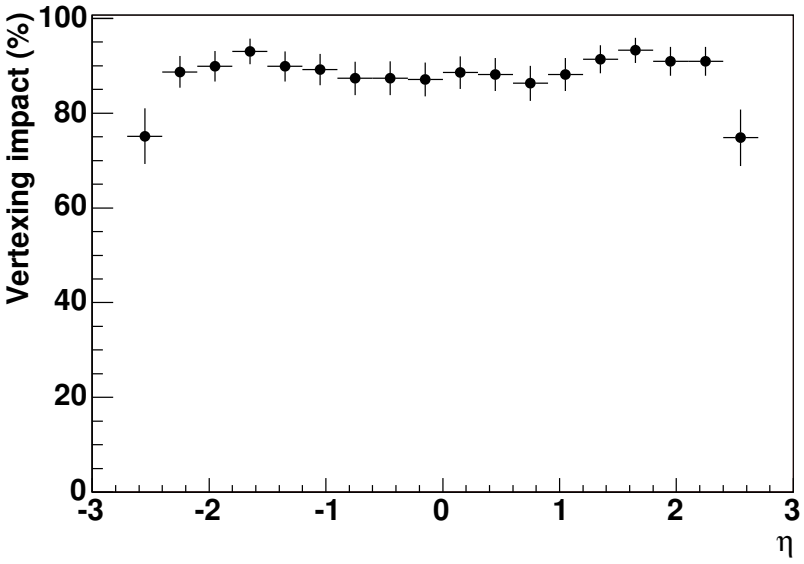

Figure 7.9: Impact of vertex reconstruction on tracking efficiency, as a function of η.

one obtained on b-jets in the same luminosity conditions. Then, figure 7.9, showing the ratio between the overall η tracking efficiency and the one evaluated in case a good primary vertex candidate was found, has the same η shape noticed in figure 7.8. This means that, as expected, the vertexing efficiency is partly spoiled in the barrel region, where many seeds are formed using SCT space points; in the endcap region, where two physical Pixel layers can be combined with the B-layer during seed formation, the vertexing efficiency is instead a bit higher. These results are summarized in table 7.4, where the overall track reconstruction performance is compared with the one obtained normalizing to those events where the primary vertex was correctly identified.

	Overall	**Good vertex**
Efficiency	77.0 ± 0.5%	87.0 ± 0.5%
Fake fraction	20.6 ± 0.1%	15.4 ± 0.1%

Table 7.4: Average tracking efficiency and fake fraction, evaluated on B-physics samples; the overall values are compared with the ones obtained normalizing to those events where the primary vertex was correctly identified.

So, even if the overall efficiency is similar to the one obtained for b-jets, the main causes of inefficiencies are very different in the two cases; in fact, they were related to tight cuts in the b-tagging samples, and to a poor vertexing performance in this case.
Timing measurements have also been performed on a 2.4 GHz processor using these data

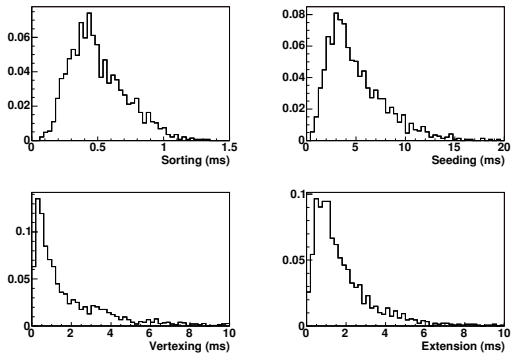

Figure 7.10: Processing time consumed by each algorithm block.

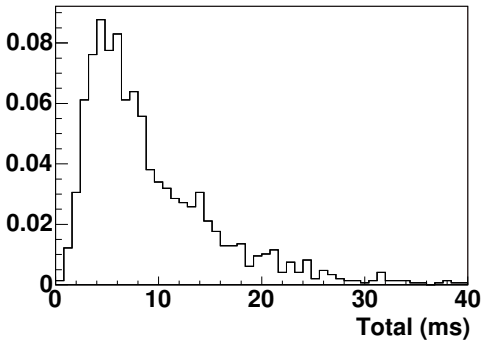

Figure 7.11: Processing time consumed by SiTrack in order to reconstruct the tracks contained in a jet RoI identified at LVL1.

	Average processing time (ms)
Sorting	0.5
Seeding	5.0
Vertexing	1.8
Extension	1.8
Total	**9.2**

Table 7.5: Timing measurements for jet reconstruction at start-up luminosity; the average processing time taken by each reconstruction step is given along with the average total algorithmic processing time.

samples. Figure 7.11 shows the distribution for the time consumed, in both luminosity conditions, processing a jet RoI identified at LVL1 and figure 7.10 shows the contribution of each algorithm block to the overall time.
The average values, given in table 7.5, show that the performance of the SiTrack algorithm already meets the requirements posed by the LVL2 environment, even if it hasn't yet been fully optimized for the reconstruction of jet samples, especially as far as the vertexing part is concerned.
The safety margin against high jet RoI multiplicities is nevertheless very limited, even assuming faster processors to be adopted for the operation in ATLAS. Anyway, adopting $\Delta\eta \times \Delta\phi = 1.5 \times 1.5$ RoIs, large superpositions are expected, so that the timing should not scale as the number of identified RoIs. Furthermore, as already mentioned, fast simulations taking into account a more refined LVL1 calorimeter clustering algorithm, foresee an average number of RoIs per event close to one. So, these results will have to be carefully crosschecked with new versions of the full simulation, in order to be sure that the required timing targets can be met by LVL2 track reconstruction algorithms.

7.3 Selection performance for $B_s \to D_s^{\pm} \to \phi\,\pi^{\pm}$ decays

In this section, the tracking strategy discussed above will be applied to the selection of channels relevant for B-physics studies in ATLAS; in particular the cases of the semi-inclusive selection of $D_s^{\pm} \to \phi\ \pi^{\pm}$ decays and the exclusive selection of the $B_s \to D_s^{\pm} \to \phi\ \pi^{\pm}$ process. As will be explained in next chapter, these channels play a fundamental role in the measurement of the properties of the B_s hadrons and, in particular, of the $B_s^0 - \bar{B}_s^0$ mixing.

7.3.1 Ingredients for the selection algorithm

As shown in chapter 6, the b-tagging selection has to be implemented using rather sophisticated statistical methods, since no information at all is available on the final state for signal events. On the other hand, the selection of decay channels relevant for B-physics studies, whose final state is completely or at least partially known, can be performed simply exploiting their kinematical and topological properties.
In particular, the most powerful tools used in these cases are invariant mass cuts, since they provide a selection specific to each of the signal decay channels. For each pair of tracks reconstructed at LVL2, the invariant mass is evaluated as

$$M = m_1^2 + m_2^2 + 2\ e_1 \cdot e_2 - 2\,\vec{p}_1 \cdot \vec{p}_2,$$

where m_1 and m_2 are the hypothetical masses of the two particles which are combined together, e_1 and e_2 are their energies, evaluated as $e = \sqrt{|\,\vec{p}\,|^2 + m^2}$ and $\vec{p} = (p_x,\ p_y,\ p_z)$ is their three-momentum. For most of these cuts, e.g. for the one selecting the $\phi \to K^+K^-$ decay, tracks are combined in opposite charge-sign pairs.
An event is then selected if it contains a track combination passing the invariant mass cuts, i.e. having an invariant mass within a window around the appropriate particle mass.
However invariant mass cuts are not the first selection applied after track reconstruction. In fact in order to reduce the combinatorial background and to minimize the overall execution time, preliminary track selection cuts are applied as follows:

- reconstructed p_T is required to be at least 1.4 GeV for the D_s decay products and at least 0.9 GeV for the π produced in the B_s decay, consistent with the offline requirements discussed before. These cuts aim at removing low-p_T tracks and so reducing the number of fake tracks formed by combinations of hits from more than one particle;

- two tracks are combined only if their longitudinal impact parameter, z_0 parameters are less than Δz away one from the other; this cut prevents the combination of two tracks coming from different reconstructed vertices and so greatly reduces the combinatorial background to the invariant mass selections. In principle the same result could be obtained performing an *a posteriori* primary vertex reconstruction, as was done for the b-tagging selection; however since this method would introduce additional inefficiencies in the track reconstruction, the selection based on Δz is preferred.

Once preliminary tracks cuts are applied and invariant mass selections have been performed, a cut on the transverse momentum of the reconstructed candidate particles is finally applied.

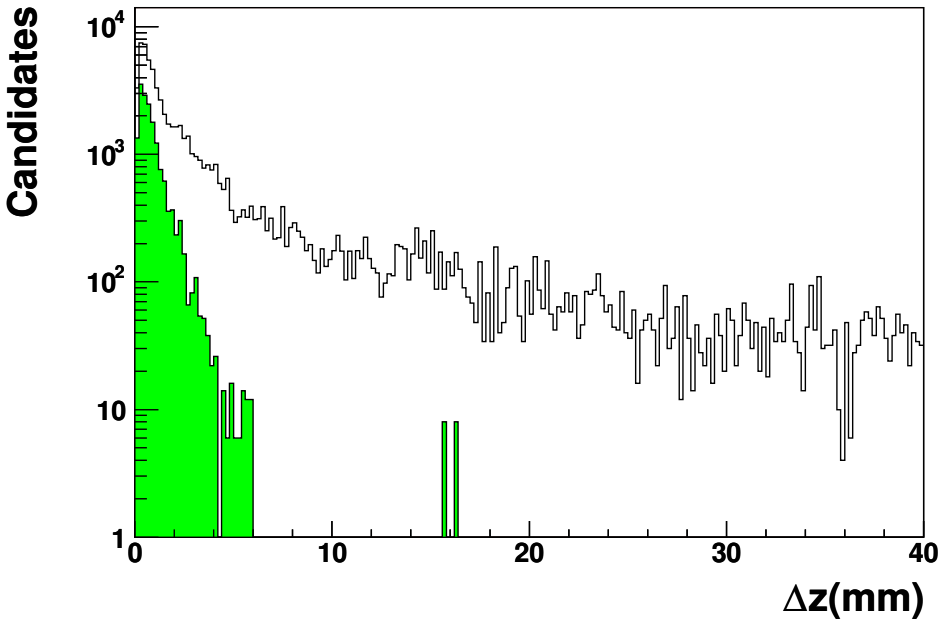

Figure 7.12: The distribution of Δz for tracks reconstructed at LVL2. Distributions are shown for signal track combinations (shaded histogram) and for the combinatorial background (open histogram).

In particular, for the selections treated in this chapter, a cut corresponding to the offline requirement of $p_T(B_s) > 10$ GeV will be studied.

7.3.2 Tuning of the selection algorithm

In this section, the above mentioned cuts will be tuned on the signal sample containing $B_s^0 \to D_s^{\pm}\,\pi^{\mp}$, $D_s^{\pm} \to \phi^0\,\pi^{\pm}$, $\phi^0 \to K^+K^-$ decays.
Figure 7.12 shows the distributions used to tune the Δz cut variable; from the comparison between the shapes obtained for the signal and the combinatorial background, follows the track selection:

$$\Delta z \; < \; 3 \text{ mm}.$$

In order to tune the selections based on invariant masses, their distributions for the signal events sample will be studied; in particular, for each reconstructed particle to be selected, the following histograms will be shown:

- All combinations: this histogram contains, for the ϕ^0 selection case, entries for all opposite charge sign track-pair combinations within the event; for the D_s and B_s selections it contains, instead, all the combination of a third track with a previously

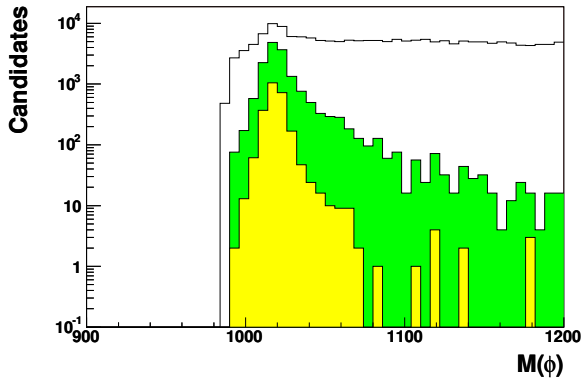

Figure 7.13: Reconstructed invariant for ϕ^0 candidates; distributions are shown for all combinations (solid histogram), for the best combinations (dark grey) and for the correct combinations (light grey).

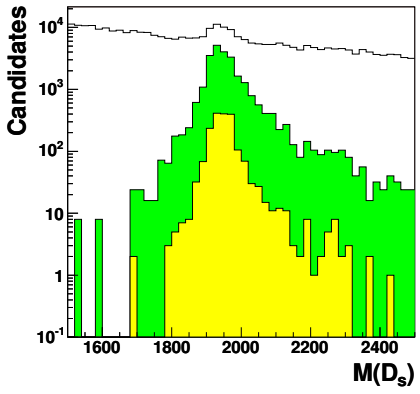

Figure 7.14: Reconstructed invariant for D_s candidates; distributions are shown for all combinations (solid histogram), for the best combinations (dark grey) and for the correct combinations (light grey).

selected candidate, respectively, for the ϕ^0 or the D_s; for the B_s selection, opposite charge is required;

- Correct combination: this histogram contains an entry for each combination of tracks having at least two space points associated to the Monte Carlo products of the signal decay;
- Best combination: this histogram contains an entry for the combination of tracks, having all their space points associated to the Montecarlo products of the signal decay, which best matches the nominal mass of the parent particle to be reconstructed; for example, for $\phi^0 \to K^+K^-$, only the reconstructed tracks completely associated to the K^+ and K^- from the ϕ^0 decay are combined together.

The distribution for all combinations, whose shape is not biased by selecting combinations nearest to the nominal parent mass, is shown to give an estimate of the amount of background rejected by each selection; as a matter of fact, its shape is very similar to the one that would be obtained for background samples. The correct combination and best combination plots are used to tune the central value and the width of each selection mass window; in fact they provide, respectively, an estimate of the interval within which the reconstructed signal mass lies and of its central core.
Figures 7.13, 7.14 and 7.15 show the mass tuning histograms, respectively for the ϕ^0, D_s and B_s selections. From gaussian fits performed on the best combination histogram, the central value and the width of each mass distribution has been obtained, as shown in table 7.6.
Finally, figure 7.16 shows the distribution for the reconstructed $p_T(B_s)$, obtained using combinations of tracks correctly linked to Montecarlo particles produced in the decay of B_s mesons

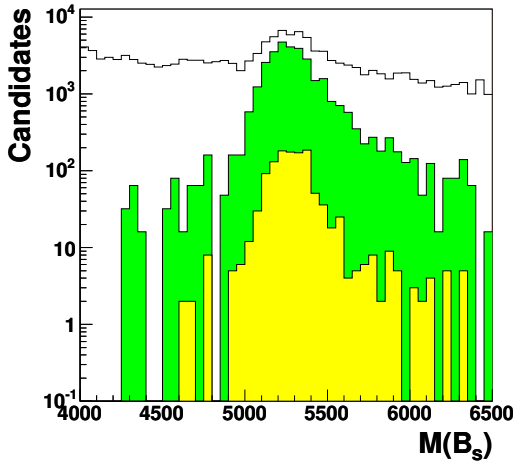

Figure 7.15: Reconstructed invariant for B_s candidates; distributions are shown for all combinations (open histogram), for the best combinations (dark grey) and for the correct combinations (light grey).

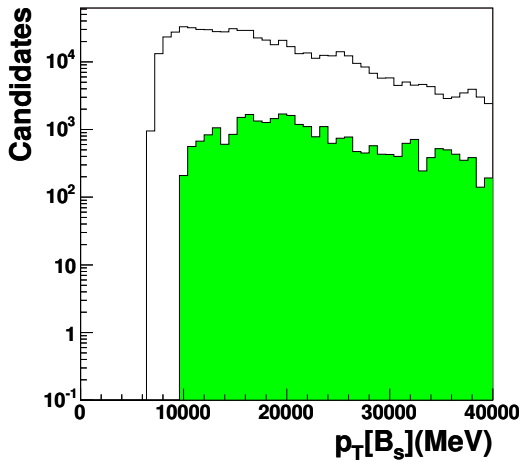

Figure 7.16: Reconstructed transverse momentum for B_s candidates; distributions are shown for all combinations (open histogram) and for combinations of tracks correctly linked to Monte Carlo particles produced in the decay of B_s mesons with $p_T >$ 10 GeV.

	Central value	**PDG mass**	**Width**	**PDG width**
ϕ^0	1019 MeV	1019.417 ± 0.014 MeV	5.7 MeV	4.458 ± 0.032 MeV
D_s	1944 MeV	1968.6 ± 0.6 MeV	32 MeV	-
B_s	5247 MeV	5369.6 ± 2.4 MeV	110 MeV	-

Table 7.6: Estimated central values and widths for each mass distribution, compared with the corresponding Particle Data Group (PDG) values.

with $p_T > 10$ GeV; the distribution obtained using all possible combinations is shown for comparison. These histograms suggest that a

$$p_T(B_s)_{rec} > 9 \text{ GeV}$$

has to be applied on the transverse momentum of the reconstructed B_s candidate, in order to efficiently select the signal sample required by offline analyses.

7.3.3 Semi-inclusive selection efficiency and rate

In order to obtain a semi-inclusive selection of the $D_s^{\pm} \to \phi\ \pi^{\pm}$ decays, the following cuts have been used:

- cut selecting $p_T > 1.4$ GeV for the reconstructed tracks;
- cut at $\Delta z < 3$ mm for each track combination processed;
- invariant mass selection for ϕ^0 candidates; given the distribution seen in figure 7.13, an asymmetrical window is selected around the central mass value; in order to study the dependence of the selection efficiency from the invariant mass cuts, three different window widths were used. These configurations adopt $[-2.5\,\sigma,\ +3.0\,\sigma]$, $[-2.0\,\sigma,\ +3.0\,\sigma]$ and $[-2.0\,\sigma,\ +2.5\,\sigma]$ windows and will be respectively referenced as *loose*, *standard* and *tight* in the following;
- invariant mass selection for D_s candidates; also in this case, given the asymmetrical signal distribution, the same *loose*, *standard* and *tight* windows are selected around the central mass value.

The resulting selection has then been applied to the signal and background samples, obtaining the efficiencies given in table 7.7 for the three different mass windows.

	Signal eff.	**Background eff.**	**Rate**
Loose selection	$58 \pm 1\%$ $(50 \pm 1\%)$	$7.2 \pm 0.3\%$	288 ± 12 Hz
Standard selection	$56 \pm 1\%$ $(48 \pm 1\%)$	$6.4 \pm 0.2\%$	256 ± 8 Hz
Tight selection	$55 \pm 1\%$ $(46 \pm 1\%)$	$5.7 \pm 0.2\%$	228 ± 8 Hz

Table 7.7: Semi-inclusive selection efficiencies and rates for signal ($D_s^{\pm} \to \phi\ \pi^{\pm}$) and background ($B \to \mu\ X$) samples, evaluated for the three different invariant mass selection cuts adopted. The signal efficiency has been evaluated with respect to the sample correctly selected by the LVL1 RoI strategy and interesting for offline studies; in brackets, the normalization to the total offline sample is given, to factorize the impact of the RoI strategy.

It should be noted that the signal efficiency has been normalized to the fraction of the sample interesting for offline studies and passing the LVL1 RoI selection. The normalization to the total offline sample is given as well, to show the impact of the RoI strategy on the overall selection performance. From this comparison it is evident that, even if the efficiency drop introduced by the RoI mechanism cannot be considered negligible, at the same time it isn't the main source of inefficiency.

	Products rec.	**Candidate rec.**	**Event selection**
Efficiency	62%	57%	59%

Table 7.8: Efficiencies for signal events obtained after each selection step; results are given for the *loose* cut configuration.

In order to explain these values, it is interesting to see how the efficiency for signal events varies at each selection step; in particular, table 7.8 shows the following quantities:

- Products reconstruction efficiency; it corresponds to the combined track reconstruction efficiency for the three D_s decay products.
  This could be naively evaluated as ϵ^3, where $\epsilon = 0.77$ is the average track reconstruction efficiency, for tracks having p_T above 1.5 GeV, quoted in table 7.4; but the result obtained this way is too low (around 46%) to match with the one given in table 7.8.
  This is easily explained reminding that ϵ contains a factor accounting for primary vertex reconstruction efficiency, i.e. $\epsilon = \epsilon_{vtx} \cdot \epsilon_{trk}$, where $\epsilon_{vtx} = 0.885$ is the vertex reconstruction efficiency and $\epsilon_{trk} = 0.87$ is the track reconstruction efficiency for events where the primary vertex has been correctly reconstructed.
  So, the products reconstruction efficiency has to be evaluated as $\epsilon_{vtx} \cdot \epsilon_{trk}^3$ (the vertexing efficiency is a collective event variable and has thus to enter this expression just once), obtaining a much more sensible result, around 58%.
  The small discrepancy with respect to the value quoted in table 7.8 could be due to a slightly pessimistic evaluation of the vertexing efficiency; as a matter of fact, while ϵ_{vtx} is averaged over the entire signal sample, the efficiency given in table 7.8 refers to the offline sample, which contains higher p_T tracks, which usually lead to a better primary vertex determination.

- Candidate reconstruction efficiency; it is the efficiency for the selection, within the invariant mass windows adopted, of a good D_s candidate, reconstructed from three tracks correctly linked to the corresponding Montecarlo particles. This value is lower than the one for products reconstruction efficiency, since each invariant mass cut, besides rejecting most of the combinatorial background, discards a small fraction of signal events.

- Event selection efficiency; it is the efficiency for the selection, within the invariant mass windows adopted, of a D_s candidate, whatever is the nature of the tracks used to reconstruct it.

It can be noticed that, applying the ϕ^0 and D_s invariant mass cuts, the selection efficiency decreases; part of the efficiency is then recovered for the event selection, thanks to the contribution of fake D_s combinations entering the mass windows. Anyway, the two efficiency values are very similar, since most times the selected candidate is a correctly reconstructed D_s, proving that the selection procedure is robust with respect to the fraction of fake candidates.
Coming to the rates, these have been evaluated starting from the assumption that the RoI based confirmation of the muon at LVL2 will reduce the muon rate from the 23 kHz provided by LVL1 to 9 kHz. Anyway, according to preliminary results on LVL2 muon confirmation performance, this assumption is pessimistic, since it should be possible to achieve a further reduction down to 5 kHz [51].

7.3.4 Exclusive selection efficiency and rate

To apply an exclusive selection of the $B_s \to D_s\pi$ decays, the following additional cuts have been adopted:

- invariant mass selection for B_s candidates; given the distribution seen in figure 7.15, an additional asymmetrical window is selected around the central B_s mass value; again, in order to study the dependence of the selection efficiency from the invariant mass cuts, two different window configurations were studied.
  The first one, referenced as *loose* in the following, adopts a $[-3.0\,\sigma,\ +3.5\,\sigma]$ window for the selection of ϕ^0 and D_s candidates and a $[-3.0\,\sigma,\ +5.0\,\sigma]$ B_s mass window.
  The second one, referenced as *tight*, uses a $[-2.5\,\sigma,\ +3.0\,\sigma]$ window to select ϕ^0 and D_s candidates and a $[-3.0\,\sigma,\ +4.0\,\sigma]$ B_s mass window;

- cut at $p_T(B_s) > 9$ GeV, in order to efficiently select all B_s candidates with p_T exceeding 10 GeV, as required by offline analyses.

This selection has then been applied to the signal and background samples, obtaining the efficiencies given in table 7.9 for the two different mass windows configurations.

	Signal eff.	**Background eff.**	**Rate**
Loose selection	$45 \pm 1\%$ $(36 \pm 1)\%$	$(1.9 \pm 0.1)\%$	(76 ± 1) Hz
Tight selection	$42 \pm 1\%$ $(34 \pm 1)\%$	$(1.2 \pm 0.1)\%$	(52 ± 1) Hz

Table 7.9: Exclusive selection efficiencies for signal ($B_s \to D_s\pi$) and background ($B \to \mu\ X$) samples, evaluated for two different sets of invariant mass cuts. The signal efficiency has been evaluated with respect to the sample correctly selected by the LVL1 RoI strategy and interesting for offline studies; in brackets, the normalization to the total offline sample is given, to factorize the impact of the RoI strategy.

Also in this case, the quoted signal efficiencies refer to the offline sample correctly selected by the RoIs identified at LVL1. The comparison with the efficiency values normalized to the total offline sample, again shows that a relatively small efficiency drop is introduced by the RoI mechanism. This time, the selection efficiency results slightly lower than the one predicted by the $\epsilon_{vtx} \cdot \epsilon_{trk}^4$ formula, which corresponds to ~50%. This small discrepancy is probably due to the fact that a lower p_T cut is applied to the π produced in the B_s decay, which is thus reconstructed with an efficiency lower than ϵ_{trk}.

7.4 Comments and conclusions

The results presented in this chapter prove the feasibility of an RoI-based approach to the selection of semi-inclusive $D_s^{\pm} \to \phi\ \pi^{\pm}$ decays, even at full start-up luminosity, provided a significant fraction of the LVL2 trigger budget is devoted to this selection. In case this wouldn't be possible, the described scheme could be adapted to apply an exclusive selection of $B_s \to D_s\pi$ decays (which constitute the physically most interesting part of the $D_s^{\pm} \to \phi\ \pi^{\pm}$ sample), in which case the LVL2 output rate is reduced to a surely affordable value.
It is worth noting, anyway, that the results presented here suffer from many pessimistic assumptions:

- the simulated detector geometry corresponds to the staged scenario, where the intermediate pixel layer is missing. First of all, this leads to a reduced primary vertex reconstruction efficiency, which can be balanced only adopting loose track reconstruction cuts and thus introducing a larger fraction of fake track candidates. Then, given the reduced spatial resolution of SCT space points with respect to the ones produced by the Pixel detector, worse track parameters are obtained by the SiTrack algorithm, leading to a worse estimation of invariant masses;

- the datasets used contain a number of pile-up events corresponding to the full start-up luminosity conditions (2×10^{33} cm^{-2} s^{-1}), while the baseline B-trigger strategy foresees that hadronic selections should operate only at lower luminosities (below 2×10^{33} cm^{-2} s^{-1}); this has obviously a negative effect on both the signal efficiency and the LVL2 output rate;

- the assumption for muon rate reduction at LVL2 could be largely pessimistic, leading to an overestimation of the output LVL2 rate up to a factor of two.

Even in these conditions, the selection procedure can still be refined; here are listed the three main improvements which the selection could benefit from:

- the LVL1 muon could be validated using the LVL2 track reconstruction, at a presumably low cost in terms of processing time; a first benefit would be the reduction of the background rate. Then this would also give the opportunity to use the z_0 parameter of the reconstructed muon as a vertexing seed for track reconstruction in the jet RoI, thus increasing the vertexing efficiency and saving a large amount of processing time;

- the track seeds produced by the SiTrack algorithm could be extended to the entire SCT or even to the TRT. In this case, besides a better resolution on track parameters, a significantly lower fraction of fake tracks would be obtained, leading to a much lower efficiency for background events;

- further rejection power against fake D_s and B_s candidates could be achieved, implementing a secondary vertex reconstruction tool inside the event selection algorithm.

Chapter 8

Impact on Unitarity Triangle Determination

8.1 The Unitarity Triangle

In this section, the fundamental role played in Standard Model physics by the CKM matrix will be reviewed; its possible parametrizations, leading to the introduction of the so-called Unitarity Triangle, will be then explained.

8.1.1 The CKM matrix in the Standard Model

As explained in chapter 1, the request of invariance under chiral transformations forbids the introduction of explicit fermionic mass terms in the SM Lagrangian.
This problem is solved adding a Yukawa coupling term between the quark fields and an Higgs doublet ϕ

$$\mathcal{L}_m = -\lambda_d^{ij}\bar{Q}_L^i \cdot \phi\, d_R^j - \lambda_u^{ij}\epsilon^{ab}\bar{Q}_{La}^i \cdot \phi_b^\dagger u_R^j + h.c.$$

where the i, j indices identify the quark families, while λ_d^{ij} and λ_u^{ij} are complex matrices.
The coupling term can be rewritten as

$$\mathcal{L}_m = -m_d^i \bar{d}_L^i d_R^i \left(1+\frac{h}{v}\right) - m_u^i \bar{u}_L^i u_R^i \left(1+\frac{h}{v}\right) + h.c.$$

where m_d^i and m_u^i are real coefficients proportional to the quark masses, using the relations

$$u_R^i \to W_u^{ij} u_R^j, \qquad d_R^i \to W_d^{ij} d_R^j \tag{8.1}$$

$$u_L^i \to U_u^{ij} u_L^j, \qquad d_L^i \to U_d^{ij} d_L^j \tag{8.2}$$

where W_u, W_d, U_u and U_d are unitary matrices transforming quark fields from the flavour eigenstates basis to the one formed by mass eigenstates [52].
Moving to that basis, the charged hadronic current becomes

$$J^{\mu+} = \frac{1}{\sqrt{2}}\bar{u}_L^i \gamma^\mu d_L^j \to \frac{1}{\sqrt{2}}\bar{u}_L^i \gamma^\mu (U_u^\dagger U_d)^{ij} d_L^j$$

showing the unitary rotation of the d_L^i fields, operated by the CKM matrix

$$V = U_u^\dagger U_d = \begin{pmatrix} V_{ud} & V_{us} & V_{ub} \\ V_{cd} & V_{cs} & V_{cb} \\ V_{td} & V_{ts} & V_{tb} \end{pmatrix}.$$

8.1.2 CKM matrix parameters

The number of independent CKM matrix parameters can be evaluated by completely general considerations; in the hypothesis of having n quark families, a generic unitary matrix $n \times n$ contains n^2 independent real parameters, which can be seen as rotation angles in an n-dimensional space and as complex phases.
In our case, applying a rotation of the $2n$ quark fields, it is possible to remove the $2n-1$ complex phases from one row and one column of the V matrix; the -1 comes from the invariance of V under collective rotations of the quark fields, or, put another way, from the fact that the phase of the element where the chosen row and column cross can't be removed twice.
Summarizing, the real independent parameters in the V matrix are

$$N = n^2 - (2n-1) = (n-1)^2$$

and can be grouped in

$$N_a = \begin{pmatrix} n \\ 2 \end{pmatrix} = \frac{1}{2}n(n-1)$$

rotation angles in the n-dimensional quark generation space and in

$$N_p = \frac{1}{2}(n-1)(n-2)$$

complex phases.
Thus, assuming that $n = 3$, as indicated by experimental measurements, the total number of CKM matrix parameters is $N = 4$, divided in three rotation angles and one complex phase, usually called δ.
These are fundamental SM parameters, like the masses of elementary particles or the Weinberg angle; this means that their values aren't theoretically predicted and have to be measured experimentally.

8.1.3 Standard parametrization of the CKM matrix

The CKM matrix can be described in many different ways, as a function of its four parameters; usually it is introduced adopting the following "standard" parametrization:

$$V = \begin{pmatrix} c_{12}c_{13} & s_{12}c_{13} & s_{13}e^{-i\delta} \\ -s_{12}c_{23} - c_{12}s_{23}s_{13}e^{i\delta} & c_{12}c_{23} - s_{12}s_{23}s_{13}e^{i\delta} & s_{23}c_{13} \\ s_{12}s_{23} - c_{12}c_{23}s_{13}e^{i\delta} & -s_{23}c_{12} - s_{12}c_{23}s_{13}e^{i\delta} & c_{23}c_{13} \end{pmatrix}$$

where $c_{ij} = \cos\theta_{ij}$ e $s_{ij} = \sin\theta_{ij}$ (with $i,\ j = 1,\ 2,\ 3$) and δ is the phase providing its complex part; the c_{ij}, s_{ij} coefficients can all be chosen to be positive.
Experimental measurements show that s_{13} and s_{23} have values of the order of $\mathcal{O}(10^{-3})$ and $\mathcal{O}(10^{-2})$ respectively. Hence, at a good level of accuracy, the following identification can be adopted

$$s_{12} = |V_{us}|, \quad s_{13} = |V_{ub}|, \quad s_{23} = |V_{cb}|.$$

8.1.4 Wolfenstein parametrization

It is phenomenologically known that the CKM matrix elements show a precise hierarchical structure, simplified in the following parametrization:

$$V \approx \begin{pmatrix} \mathcal{O}(1) & \mathcal{O}(10^{-1}) & \mathcal{O}(10^{-3}) \\ \mathcal{O}(10^{-1}) & \mathcal{O}(1) & \mathcal{O}(10^{-2}) \\ \mathcal{O}(10^{-3}) & \mathcal{O}(10^{-2}) & \mathcal{O}(1) \end{pmatrix};$$

the modulus of the elements mixing quarks belonging to the same family ($|V_{ud}|$, $|V_{cs}|$ and $|V_{tb}|$) is close to one, while is ~ 0.2 for those connecting the first and the second families ($|V_{us}|$ and $|V_{cd}|$), $\sim 4 \cdot 10^{-2}$ for those linking the second and the third families ($|V_{cb}|$ and $|V_{ts}|$) and $\sim 5 \cdot 10^{-3}$ for those mixing the first and the third families ($|V_{ub}|$ and $|V_{td}|$).
A possible CKM matrix parametrization, proposed by Wolfenstein [53], transparently shows this hierarchy; infact, in this approximation, each matrix element is expanded in series with respect to the $\lambda = |V_{us}| \approx 0.22$ parameter:

$$V = \begin{pmatrix} 1 - \frac{\lambda^2}{2} & \lambda & A\lambda^3(\rho - i\eta) \\ -\lambda & 1 - \frac{\lambda^2}{2} & A\lambda^2 \\ A\lambda^3(1 - \rho - i\eta) & -A\lambda^2 & 1 \end{pmatrix} + \mathcal{O}(\lambda^4),$$

where λ, A, ρ and η form a parameters set alternative to the standard one containing s_{12}, s_{13}, s_{23} and δ.
The main limitation of this choice is that, neglecting terms of $\mathcal{O}(\lambda^4)$ and $\mathcal{O}(\lambda^5)$, it doesn't grant the precision required by the most accurate phenomenological applications.

8.1.5 Generalized Wolfenstein parametrization

Among the possible generalizations of the Wolfenstein parametrization, the predominantly adopted one starts from the definition of the parameters (λ, A, ρ, η) as

$$s_{12} = \lambda, \quad s_{23} = A\lambda^2, \quad s_{13}e^{-i\delta} = A\lambda^3(\rho - i\eta)$$

to be considered exact at all orders in λ [54], [55].
From these definitions follows

$$\rho = \frac{s_{13}}{s_{12}s_{23}}\cos\delta, \quad \eta = \frac{s_{13}}{s_{12}s_{23}}\sin\delta.$$

Substituting into the standard parametrization, an exact expression of the CKM matrix in terms of (λ, A, ρ, η) is obtained. Expanding each term in series with respect to λ, the

Wolfenstein parametrization is recovered, with the addition of higher order terms.
Stopping at $\mathcal{O}(\lambda^5)$ we get

$$V = \begin{pmatrix} 1-\frac{1}{2}\lambda^2-\frac{1}{8}\lambda^4 & \lambda+\mathcal{O}(\lambda^7) & A\lambda^3(\rho-i\eta) \\ -\lambda+\frac{1}{2}A^2\lambda^5[1-2(\rho+i\eta)] & 1-\frac{1}{2}\lambda^2-\frac{1}{8}\lambda^4(1+4A^2) & A\lambda^2+\mathcal{O}(\lambda^8) \\ A\lambda^3(1-\overline{\rho}-i\overline{\eta}) & -A\lambda^2+\frac{1}{2}A\lambda^4[1-2(\rho+i\eta)] & 1-\frac{1}{2}A^2\lambda^4 \end{pmatrix},$$

where [54]

$$\overline{\rho} = \rho(1-\frac{\lambda^2}{2}), \quad \overline{\eta} = \eta(1-\frac{\lambda^2}{2}).$$

The main advantage of this generalization is the absence of significant corrections to V_{us}, V_{cd}, V_{ub} and V_{us}; furthermore, as explained in the following, the substitution adopted for V_{td} allows to obtain a simple higher order generalization for the Unitarity Triangle.

8.1.6 The Unitarity Triangle

The unitarity of the CKM matrix implies relations, called orthogonality relations, between its elements:

$$\sum_{k=u,c,t} V_{ki}V_{kj}^* = 0, \quad i \neq j \in \{d,s,b\};$$

Associating each term of these relations to a vector in the $(\overline{\rho},\overline{\eta})$ complex plane, each relation can be graphically represented by a triangle. Figure 8.1 shows the triangle corresponding to

$$V_{ud}V_{ub}^* + V_{cd}V_{cb}^* + V_{td}V_{tb}^* = 0,$$

which is, for sure, the most relevant orthogonality relation from the phenomenological point of view; on each side of the triangle is shown its length, scaled by a factor $A\lambda^3$. Given their structure, the orthogonality conditions are invariant with respect to phase redefinitions for the quark fields; infact, such transformations simply rotate the corresponding triangles in the $(\overline{\rho},\overline{\eta})$ plane, leaving their sides and angles unchanged. These quantities are thus physical observables and can be measured experimentally.
The particular relevance of the triangle in figure 8.1 is due to the fact that it is the only one having similar lengths for all its sides. All the other orthogonality conditions correspond, on the contrary, to triangles having one side much shorter than the others by orders of magnitude; this obviously poses many disadvantages from the experimental point of view, since, as an example, it means that one of the three angles to be measured is very close to zero. Furthermore, the condition depicted in figure 8.1 is particularly interesting for the quantities it involves, V_{ub}, V_{cb} and V_{td}, on whose measurement much effort has been already put.
Anyway, the study of triangles corresponding to the other conditions will become more relevant as soon as precise measurements on rare CP violating decays will be available.
Another invariant under phase transformations is the area of each triangle, which can be evaluated as

$$A_\Delta = \frac{1}{2}\left|\mathrm{Im}[(V_{ki}V_{kj}^*)(V_{li}V_{lj}^*)^*]\right|, \quad k \neq l \in \{u,c,t\}.$$

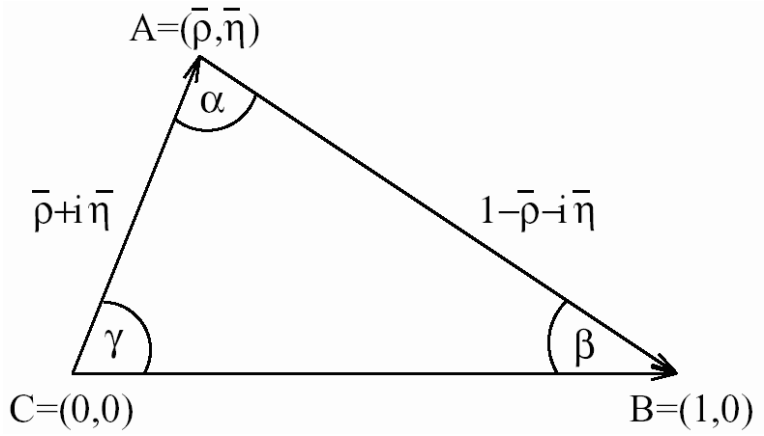

Figure 8.1: The Unitarity Triangle: over each side is shown its length, scaled by a factor $A\lambda^3$, as evaluated in Wolfenstein parametrization. It must be noticed that, in this parametrization and in its generalization, the CB side is real, to an excellent approximation; the first imaginary contributions to the corresponding $V_{cd}V_{cb}^*$ term appear only at $\mathcal{O}(\lambda^7)$.

Furthermore, the unitarity of the CKM matrix grants that A_Δ is the same for all the triangles built starting from orthogonality relations.
Finally, A_Δ is strictly related to CP violation in the Standard Model; infact, the entity of CP violation in Standard Model phenomena can be evaluated by the parameter

$$J_{CP} = \mathrm{Im}(V_{ij}V_{lk}V_{lj}^*V_{ik}^*), \quad i \neq l \in \{u,c,t\}, \quad j \neq k \in \{d,s,b\};$$

which is related to Unitarity Triangle area through

$$|J_{CP}| = 2 \cdot A_\Delta.$$

This means that, in case of no CP violation, all unitarity triangles would have $A_\Delta = 0$, coherently with the fact that their sides would be real, as all CKM elements.

8.2 Fit of the Unitarity Triangle

The experimental measurements involving CKM matrix elements and other related parameters (e.g. ε_K, $\Delta M_{d,s}$, etc...) can be used to constrain the Unitarity Triangle (UT) parameters. In this section, the most relevant constraints will be summarized, along with the statistical methods adopted to fit the UT parameters.

8.2.1 Constraints on $\overline{\rho}$ and $\overline{\eta}$

In the ideal case of having no uncertainties on the experimental measurements, the corresponding constraints would be represented as curves in the $(\overline{\rho}, \overline{\eta})$ plane; in that case, supposing the Standard Model picture of flavour physics is correct, all the curves should cross

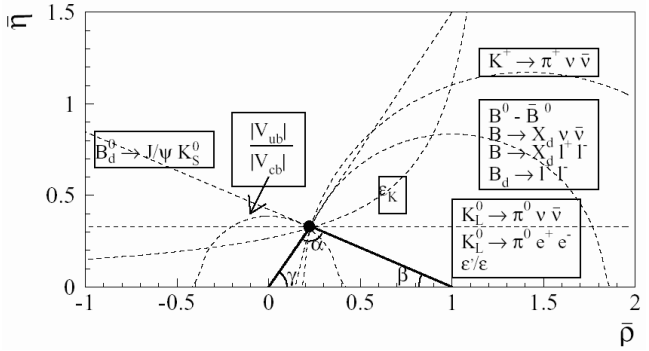

Figure 8.2: Ideal constraints on the Unitarity Triangle. For each experimental measurement constraining the apex of the triangle, the corresponding curve in the $(\overline{\rho},\overline{\eta})$ plane is shown. In case of no uncertainties on the measurements, all the curves cross in the same place.

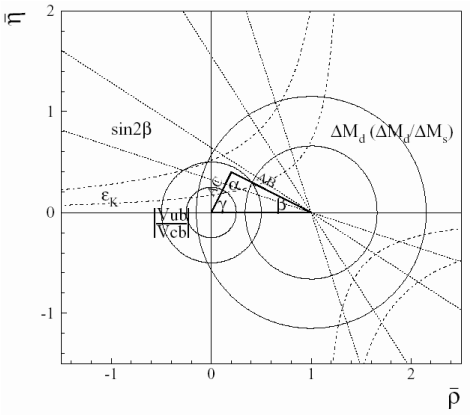

Figure 8.3: Realistic constraints on the Unitarity Triangle. In this case, each constraint corresponds to a permitted region for $\overline{\rho}$ and $\overline{\eta}$. The widths of the depicted regions are purely explicative and do not represent the current experimental situation.

in one point, as shown in figure 8.2.
Currently, there are five most relevant and independent measurements used to constrain $(\overline{\rho},\overline{\eta})$ in the Standard Model. The corresponding constraints are graphically represented in figure 8.3 as allowed regions for $\overline{\rho}$ and $\overline{\eta}$ and no more as single curves, since the measurements are affected by both experimental and theoretical uncertainties.

- $|V_{ub}|$ **constraint:**
  the length of the AC side of the UT is determined by

$$R_b = \sqrt{\overline{\rho}^{\,2} + \overline{\eta}^{\,2}} = \left(1 - \frac{\lambda^2}{2}\right)\frac{1}{\lambda}\left|\frac{V_{ub}}{V_{cb}}\right|.$$

  The corresponding constraint is represented by a circle centered in $(0,0)$ and having a radius equal to R_b.

- $|\varepsilon_K|$ **constraint:**
  the ε parameter, related to CP violation in the K meson system, can be theoretically calculated as

$$\varepsilon = C_\varepsilon \hat{B}_K \mathrm{Im}\,\lambda_t\{\mathrm{Re}\,\lambda_c[\eta_1 S_0(x_c) - \eta_3 S_0(x_c,x_t)] - \mathrm{Re}\,\lambda_t \eta_2 S_0(x_t)\}e^{i\pi/4},$$

  where the C_ε constant is

$$C_\varepsilon = \frac{G_F^2 F_K^2 m_K M_W^2}{6\sqrt{2}\pi^2 \Delta M_K} = 3.837 \cdot 10^4.$$

Starting from this formula and substituting

$$\lambda_t = V_{ts}^* V_{td} \approx -A^2\lambda^5(1-\overline{\rho}-i\overline{\eta}), \quad \mathrm{Re}\,\lambda_t \approx -A^2\lambda^5(1-\overline{\rho}), \quad \mathrm{Im}\,\lambda_t \approx A^2\lambda^5\overline{\eta},$$
$$\lambda_c = V_{cs}^* V_{cd} \approx -(\lambda - \frac{1}{2}\lambda^3), \qquad \mathrm{Re}\,\lambda_c \approx -(\lambda - \tfrac{1}{2}\lambda^3), \qquad \mathrm{Im}\,\lambda_c \approx 0,$$

obtained from the generalized Wolfenstein parametrization stopping respectively at $\mathcal{O}(\lambda^7)$ and $\mathcal{O}(\lambda^5)$, we get

$$|\varepsilon| = \overline{\eta}[(1-\overline{\rho})A^2 C_1 + \frac{1}{\lambda^4} C_2] A^2 \lambda^{10} \hat{B}_K.$$

A strong dependence of the right hand side from $\lambda = |V_{us}|$ could be expected; anyway it is almost completely canceled by the contributions of $A = |V_{cb}|/\lambda^2$ and C_2/λ^4 in parenthesis. The largest uncertainties on this constraint come, instead, from the theoretically calculated $\hat{B}_K$ parameter and partly from A^4 or, equivalently, $|V_{cb}|^4$.
This constraint corresponds to an hyperbola in the $(\overline{\rho}, \overline{\eta})$ plane.

- ΔM_d **constraint:**
the R_t length of the AB side can be determined studying the mixing phenomena in the $B_d^0 - \overline{B}_d^{\,0}$ system, parametrized by ΔM_d, obtaining

$$R_t = \sqrt{(1-\overline{\rho})^2 + \overline{\eta}^{\,2}} = \frac{1}{\lambda}\frac{|V_{td}|}{|V_{cb}|},$$

where

$$|V_{td}| \propto \frac{\sqrt{\Delta M_d}}{F_{B_d}\sqrt{\hat{B}_{B_d}}}.$$

Since m_t, ΔM_d and η_B are known with good precision, the main uncertainties come from $F_{B_d}\sqrt{\hat{B}_{B_d}}$. R_t, furthermore, suffers from the additional uncertainty on $|V_{cb}|$.
The corresponding constraint is represented in the $(\overline{\rho}, \overline{\eta})$ plane by a circle centered in $(1, 0)$ and having a radius equal to R_t.

- $\Delta M_d/\Delta m_s$ **constraint:**
measuring the properties of the $B_d^0 - \overline{B}_d^{\,0}$ mixing, parametrized by Δm_s and ΔM_d, provides an alternative way of determining R_t:

$$R_t = \frac{1}{\lambda}\xi\sqrt{\frac{m_{B_s}}{m_{B_d}}}\sqrt{\frac{\Delta m_s}{\Delta M_d}}\left(1 - \frac{\lambda^2}{2} + \overline{\rho}\lambda^2\right), \quad \xi = \frac{F_{B_s}\sqrt{\hat{B}_s}}{F_{B_d}\sqrt{\hat{B}_d}}.$$

This constraint follows from the theoretical calculation of ΔM_d and Δm_s, and the $(1 - \lambda^2/2 + \overline{\rho}\lambda^2)$ term accounts for the fact that $|V_{ts}/V_{cb}|$ is not equal to 1; anyway, for $0 \leq \overline{\rho} \leq 0.5$, this factor differs from unity for less than 2%.
The advantages of determining R_t from the $\Delta M_d/\Delta m_s$ ratio, are the lower hadronic uncertainties on ξ with respect to those on $F_{B_d}\sqrt{\hat{B}_{B_d}}$ and the independence from m_t and $|V_{cb}|$.

- $a(\psi K_S)$ **constraint:**
  the CP asymmetry $a_{\psi K_S}$, induced by mixing, allows to determine the β angle of the UT avoiding almost completely hadronic uncertainties, through the relation

$$(\sin 2\beta)_{\psi K_S} = 0.739(XXX) \pm 0.048.$$

  The value quoted here is a world average, completely dominated by the results of the BaBar and Belle collaborations.

8.2.2 Bayesian approach to the Unitarity Triangle fit

Different statistical methods have been proposed to constrain the apex of the Unitarity Triangle; even if these methods show significant differences, mainly in the treatment of experimental and theoretical uncertainties, they all aim at achieving basically the same achievements. First of all, the common goal is desuming, starting from experimental measurements, a region containing the apex of the triangle with a given level of probability or confidence; in most cases, the fit also provides an estimate of the best value for $\overline{\rho}$ and $\overline{\eta}$. Then, in every method the experimental uncertainties deriving from statistical errors and systematic effects, and the theoretical uncertainties, are combined into a global uncertainty on $\overline{\rho}$ and $\overline{\eta}$.
Nowadays, given the high precision reached for both experimental measurements and theoretical calculations, very accurate statistical analysis methods have to be adopted. These mainly differ in the way theoretical and systematic uncertainties are treated and for the interpretation of their final result. On this basis, they can be subdivided into two main groups: those adopting the bayesian approach, based on a generalization of Bayes' theorem for the conditioned probability; those following the so-called frequentist approach, which, in order to reduce the amount of *a priori* assumptions, don't associate any statistical distribution to theoretical parameters.
In the following, an example application of the first approach will be adopted [56]. Its basic idea can be summarized as follows: when uncertainties are introduced for each parameter used to constrain the UT apex, a family of curves is obtained, each weighted according to the statistical distribution for the corresponding parameter; so, also the points in the ($\overline{\rho}$,$\overline{\eta}$) plane, having the same *a priori* probability, acquire different weights and the confidence level for the $\overline{\rho}$ and $\overline{\eta}$ values accumulates in a given region.
This approach is formalized in the next two subsections.

Bayesian inference

Each of the five equations described before connects a constraint c_j (where c_j stands for $|V_{ub}/V_{cb}|$, $|\varepsilon_K|$, ΔM_d, $\Delta M_d/\Delta m_s$, $\sin 2\beta$ for $j = 1, ..., 5$) to the $\overline{\rho}$ and $\overline{\eta}$ UT parameters, through a relation

$$c_j = c_j(\overline{\rho},\, \overline{\eta};\, \mathbf{x}),$$

where $\mathbf{x} = \{x_1, x_2, ..., x_N\}$ are additional parameters representing all the experimentally measured or theoretically calculated quantities connected to c_j.
In the ideal case of perfect knowledge of c_j and $\mathbf{x}$, all the points contained in the corresponding curve are completely equivalent. In real life, both c_j and $\mathbf{x}$ are affected by uncertainties;

anyway the ignorance on any quantity is never complete. First of all, some values will be excluded experimentally or by theoretical limits. Furthermore, given an interval where a particular quantity almost certainly lies, it is possible to assign different probabilities to different subintervals; this happens, as an example, for mass measurements, where the values close to the best experimental estimation are considered the most probable. In other words, it is always possible to define a probability density function (p.d.f.) for each element of the $\{c_j,\, \mathbf{x}\}$ set.
These considerations suggest to adopt a bayesian approach, where each uncertainty is described in terms of a probability distribution $f(\cdot)$, quantifying our confidence level on different values for the same variable. Following these assumptions, $\overline{\rho}$ and $\overline{\eta}$ can be inferred by a simple application of probability laws, thus avoiding *ad hoc* solutions, used instead by other analysis methods. Applying Bayes' theorem to a single constraint we get

$$\begin{aligned} f(\overline{\rho},\, \overline{\eta},\, c_j,\, \mathbf{x} \,|\, \hat{c}_j) &\propto f(\hat{c}_j \,|\, c_j,\, \overline{\rho},\, \overline{\eta},\, \mathbf{x}) \cdot f(c_j,\, \overline{\rho},\, \overline{\eta},\, c_j,\, \mathbf{x}) \\ &\propto f(\hat{c}_j \,|\, c_j) \cdot f(c_j \,|\, \overline{\rho},\, \overline{\eta},\, \mathbf{x}) \cdot f(\mathbf{x},\, \overline{\rho},\, \overline{\eta}) \\ &\propto f(\hat{c}_j \,|\, c_j) \cdot \delta(c_j - c_j(\overline{\rho},\, \overline{\eta},\, \mathbf{x})) \cdot f(\mathbf{x}) \cdot f_\circ(\overline{\rho},\, \overline{\eta}), \end{aligned} \tag{8.3}$$

where $\hat{c}_j$ is the best estimate for c_j and $f_\circ(\overline{\rho},\, \overline{\eta})$ corresponds to the *a priori* distribution for the two UT parameters.
This formula follows from probability laws, assuming the independence of the different quantities and noticing that $\hat{c}_j$ depends from $(\overline{\rho},\, \overline{\eta},\, \mathbf{x})$ only through c_j. This is true for the Standard Model case, since c_j can be unambiguously desumed from the knowledge of $\overline{\rho}$, $\overline{\eta}$ and $\mathbf{x}$.
The extension to the realistic case, where more constraints are used, is obtained modifying the above formula into

$$f(\overline{\rho},\, \overline{\eta},\, \mathbf{x} \,|\, \hat{c}_1, ..., \hat{c}_M) \propto \prod_{j=1,...,M} f_j(\hat{c}_j \,|\, \overline{\rho},\, \overline{\eta},\, \mathbf{x}) \times \prod_{i=1,...,N} f_i(x_i) \times f_\circ(\overline{\rho},\, \overline{\eta}),$$

where M and N are respectively the number of constraints and of parameters; again, the independence of the different quantities has been used.
Integrating this function with respect to $\mathbf{x}$ we obtain

$$f(\overline{\rho},\, \overline{\eta} \,|\, \hat{\mathbf{c}},\, \mathbf{f}) \propto \mathcal{L}(\hat{\mathbf{c}} \,|\, \overline{\rho},\, \overline{\eta},\, \mathbf{f}) \times f_\circ(\overline{\rho},\, \overline{\eta}),$$

where $\hat{\mathbf{c}}$ represents the set of experimentally measured constraints and

$$\mathcal{L}(\hat{\mathbf{c}} \,|\, \overline{\rho},\, \overline{\eta},\, \mathbf{f}) = \int \prod_{j=1,...,M} f_j(\hat{c}_j \,|\, \overline{\rho},\, \overline{\eta},\, \mathbf{x}) \prod_{i=1,...,N} f_i(x_i) dx_i$$

is the overall *likelihood*, taking into account all possible values for the x_i, properly weighted according to the corresponding *p.d.f.* $f(\mathbf{x})$. Even if all the $\overline{\rho}$ and $\overline{\eta}$ values have the same *a priori* probability ($f_\circ(\overline{\rho},\, \overline{\eta}) = cost$), their probability distribution clusters, *a posteriori*, around those values maximizing the *likelihood*.
Finally, the *p.d.f.* obtained, assuming *a priori* equiprobable values for $\overline{\rho}$ and $\overline{\eta}$, is

$$f(\overline{\rho},\, \overline{\eta}) \propto \int \prod_{j=1,...,M} f_j(\hat{c}_j \,|\, \overline{\rho},\, \overline{\eta},\, \mathbf{x}) \prod_{i=1,...,N} f_i(x_i) dx_i.$$

The integral can be evaluated with Montecarlo methods, for which the normalization problem is easily solved. Once a normalized distribution for $\overline{\rho}$ and $\overline{\eta}$ has been evaluated, it is possible to define probability intervals $P(w)$ through the conditions

$$(\overline{\rho}, \overline{\eta}) \in P(w) \text{ if } f(\overline{\rho}, \overline{\eta}) > z_w$$
$$\int_{P_w} f(\overline{\rho}, \overline{\eta})\, d\overline{\rho}\, d\overline{\eta} = w.$$

It must be noticed that the bayesian inference method doesn't make any distinction between the case in which the likelihood for a particular constraint is different from zero only in a limited interval (which is the case usually referred as a measurement) and the case in which it goes to zero only on one side (case faced when $c_j \to \infty$ or 0 and experimental measurements provide only a lower or an upper limit). This latter case applies, at the moment, to the Δm_s measurement; as a consequence, available data on this constraint naturally enter the analysis process, with the same dignity of other constraints; this is not true, on the contrary, for the other approaches proposed in literature.

Systematic and theoretical uncertainties

The most relevant controversy in the statistical analysis of the Unitarity Triangle is connected with the quantitative treatment of the uncertainties arising from systematic effects or from theoretical calculations.
One of the strongest points of the bayesian approach is that the concept of uncertainty it is based on has the same meaning in all the possible cases; as an example, there is no difference between the above mentioned uncertainties and the ones coming from random fluctuations that could have affected the experimental measurement. The inferential formula derived in the previous subsection can be thus used in its generalized form, including in $\mathbf{x}$ also the parameters which are responsible of systematic uncertainties.
Furthermore, independently from the assumptions made on the *p.d.f.* for $\mathbf{x}$, the overall likelihood $f(\hat{c}_j)$ are approximatively gaussian, due to a mechanism similar to the central limit theorem. This grants results which prove stable with respect to variations, within reasonable intervals, of the models and the parameters adopted to describe theoretical and systematic uncertainties. By the way, this explains why methods based on χ^2 minimization can be considered an approximation of the bayesian method adopted here.
As far as the choice for $f_i(x_i)$ is concerned, given the low sensitivity of the final result with respect to the model adopted, the problem can be simplified reducing to a couple of possible choices. A gaussian model will be used to describe cases where the uncertainty mainly comes from statistical effects or where the systematic error is due to many comparable contributions. A uniform *p.d.f.* will be adopted, instead, for those parameters assuming values in a limited interval, within which all points are considered equiprobable.

8.3 Current status of the Unitarity Triangle fit

This section is devoted to the discussion of the latest results, obtained from the Unitarity Triangle analysis assuming that the Standard Model picture of flavour physics is correct.

Parameter	Value	Gaussian σ	Theoretical uncertainty
λ	0.2240	0.0036	-
$\|V_{cb}\|$ ($\times 10^{-3}$) (excl.)	42.1	2.1	-
$\|V_{cb}\|$ ($\times 10^{-3}$) (incl.)	41.6	0.7	0.6
$\|V_{ub}\|$ ($\times 10^{-4}$) (excl.)	33.0	2.4	4.6
$\|V_{ub}\|$ ($\times 10^{-4}$) (incl.)	40.9	4.6	3.6
m_t (GeV)	167	5	-
m_c (GeV)	1.3	0.1	-
Δm_d (ps^{-1})	0.502	0.006	-
Δm_s (ps^{-1})	> 14.4 at 95% C.L.	sensitivity 19.2	-
$F_{B_d}\sqrt{\hat{B}_{B_d}}$ (MeV)	223	33	12
ξ	1.24	0.04	0.06
$\hat{B}_K$	0.86	0.06	0.14
$\|\varepsilon_K\|$ ($\times 10^{-3}$)	2.28	0.013	-
$\sin 2\beta$	0.739	0.048	-

Table 8.1: Input parameters for the Unitarity Triangle fit: for each parameter are quoted the best value, the experimental error and the theoretical uncertainty.

From the statistical point of view, the above described bayesian method will be adopted [57]. After a brief summary of the current status of the input fit parameters, the results for $\overline{\rho}$, $\overline{\rho}$ and for the α, β and γ angles will be reported; then some tests of the SM description of mixing phenomena will be discussed; finally, the *a posteriori* p.d.f. obtained for Δm_s will be discussed.

8.3.1 Current status of the input parameters

Table 8.1 shows, for each UT fit input parameter, the central value, the statistical uncertainties (associated to a gaussian distribution) and the systematic or theoretical one (for which a flat distribution is adopted), updated in February 2005.
The main novelties with respect to the past years are the final LEP/SLD likelihood for Δm_s (which now indicates a slightly lower value, while the sensitivity is almost unchanged), the use of $|V_{ub}|$ measurements from inclusive semileptonic decays at the B factories [] and the updated value of $sin2\beta$.
In addition, the updated values of the top mass $m_t^{pole} = 178.0 \pm 4.3$ GeV [] and of the CKM parameter λ were used. The latter comes from the average of the following values []

$$\lambda(V_{us} \text{ from Kl3}) = 0.2250 \pm 0.0021$$
$$\lambda(V_{ud} + \text{unitarity}) = 0.2265 \pm 0.0020.$$

As far as theoretical calculations are concerned, a significant improvement has been achieved for the inclusive determination of $|V_{cb}|$. Another important update is related to the effect of the so-called chiral logs on the lattice evaluation of $F_{B_d}\sqrt{\hat{B}_{B_d}}$, which is reflected on ξ. The

Parameter	68%	95%	99%
$\overline{\rho}$	0.196 ± 0.045	[0.104, 0.283]	[0.073, 0.314]
$\overline{\eta}$	0.347 ± 0.025	[0.296, 0.396]	[0.281, 0.412]
α (°)	96.1 ± 7.0	[82.1, 110.0]	[77.7, 114.8]
β (°)	23.4 ± 1.5	[20.8, 26.1]	[20.2, 27.1]
γ (°)	60.3 ± 6.8	[47.0, 74.2]	[42.5, 78.9]
$sin2\alpha$	-0.21 ± 0.24	[-0.65, 0.27]	[-0.77, 0.41]
$sin2\beta$	0.726 ± 0.028	[0.670, 0.780]	[0.651, 0.797]
$sin(2\beta+\gamma)$	0.947 ± 0.038	[0.852, 0.996]	[0.813, 0.998]
$Im\lambda_t$ (10^{-5})	13.3 ± 0.9	[11.5, 15.1]	[10.9, 15.6]

Table 8.2: Values and probability ranges for the UT parameters obtained from the UT fit using the following constraints: $|V_{ub}|/|V_{cb}|$, Δm_d, Δm_s, ε_K and $sin2\beta$. The value of $Im\lambda_t = ImV_{ts}^* V_{td}$ is also given.

central value of that ratio increased of about 5%, while the corresponding uncertainty is now 50% higher.

8.3.2 Fit results

Using the above mentioned constraints from $|V_{ub}|/|V_{cb}|$, Δm_d, Δm_s, ε_K and $sin2\beta$, the fit results summarized in table 8.2 are obtained. The central value for each p.d.f. is calculated using the median and the error corresponds to 34% probability regions on each side of the median; asymmetric errors are symmetrized changing the quoted central value. The 95% and 99% probability intervals for each UT parameter are also quoted.
Figure 8.4 shows the regions for $\overline{\rho}$ and $\overline{\eta}$, allowed by the adopted constraints, and corresponding to 68% and 95% probability.
Figure 8.5 shows, instead, the one-dimensional *a posteriori* p.d.f.'s obtained for α, $sin2\beta$, γ and $sin(2\beta+\gamma)$ and the corresponding 68% and 95% probability intervals.

8.3.3 Test of the CKM mechanism in the Standard Model

The standard fit, whose results are shown in figure 8.4, already provides a striking evidence of the success of the flavour physics description provided by the Standard Model; as a matter of fact, the overlap between the different and independent constraints is almost complete and enables to select quite a tiny allowed region for the $\overline{\rho}$ and $\overline{\eta}$ parameters.
Anyway more stringent tests can be performed; the most crucial one is performed providing evidence of CP violation by using the sides of the UT, i.e. CP-conserving processes, such as the semileptonic B decays and $B_{d,s} - \bar{B}_{d,s}$ oscillations. The comparison of the region selected by these constraints and the one selected by the direct measurements of CP violation in the kaon (ε_K) or in the B ($sin2\beta$) sectors is shown in figure 8.6 and gives a picture of the success of the SM in the flavour sector.
A more quantitative check is provided by the comparison between the value of $\overline{\rho}$ and $\overline{\eta}$

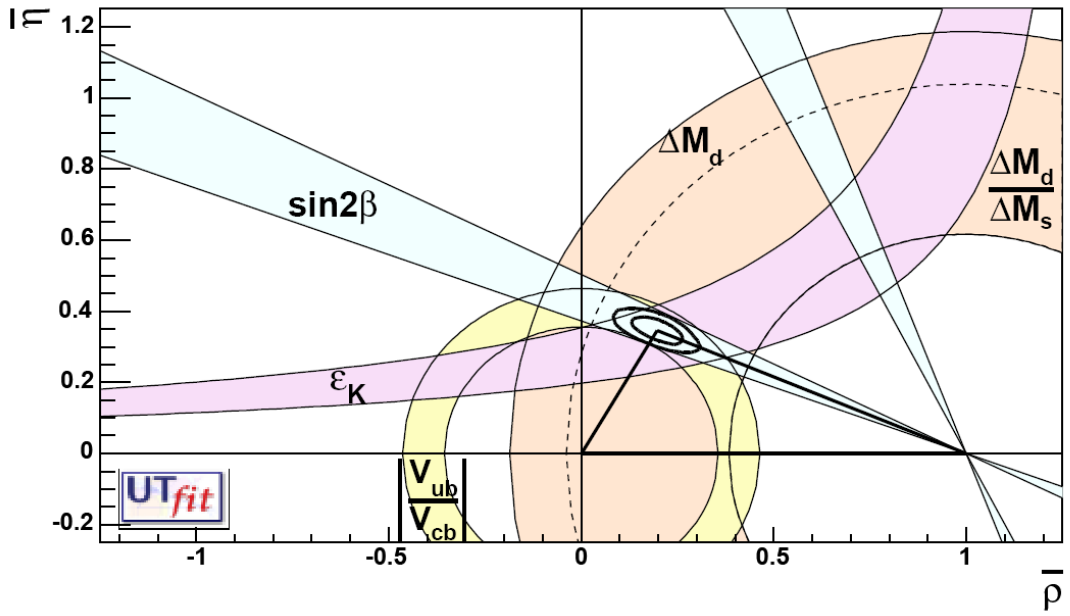

Figure 8.4: Allowed regions for $\overline{\rho}$ and $\overline{\eta}$; the closed contours at 68% and 95% probability are shown. The full lines correspond to 95% probability regions for each of the constraints.

computed from CP-conserving and CP-violating observables:

$$\begin{array}{lll} \overline{\rho} = 0.169 \pm 0.057 \ \ ([0.055, 0.310] \text{ at } 95\%) & & \\ \overline{\eta} = 0.364 \pm 0.037 \ \ ([0.252, 0.430] \text{ at } 95\%) & \text{from UT sides only} & \\ \overline{\rho} = 0.241 \pm 0.070 \ \ ([0.098, 0.363] \text{ at } 95\%) & & \\ \overline{\eta} = 0.311 \pm 0.030 \ \ ([0.260, 0.371] \text{ at } 95\%) & \text{from } S(J/\psi K^0) + \varepsilon_K. & \end{array}$$

Another test can be performed by comparing the value of $sin2\beta$ from $S(J/\psi K^0)$ and the one determined from measurements connected to the sides of the UT

$$\begin{array}{lll} sin2\beta = 0.734 \pm 0.043 \ \ ([0.616, 0.811] \text{ at } 95\%) & \text{UT sides only} \\ sin2\beta = 0.726 \pm 0.037 \ \ ([0.652, 0.800] \text{ at } 95\%) & S(J/\psi K^0) \end{array}$$

Finally, the value of $sin2\beta$ obtained by using all the constraints but the direct determination is

$$sin2\beta = 0.725 \pm 0.043 \ \ ([0.634, 0.804] \text{ at } 95\%) \qquad \text{UT sides} + \varepsilon_K,$$

showing an impressive agreement with the directly measured one. Anyway this is not a novelty, since the value of $sin2\beta$ was correctly predicted by UT fits even before its first direct measurement.
In conclusion, the agreement of all these determinations confirms the validity of CKM mechanism in the SM. This test relies on several non-perturbative techniques, such as the Operator Product Expansion for computing B decay rates, the Heavy Quark Effective Theory and

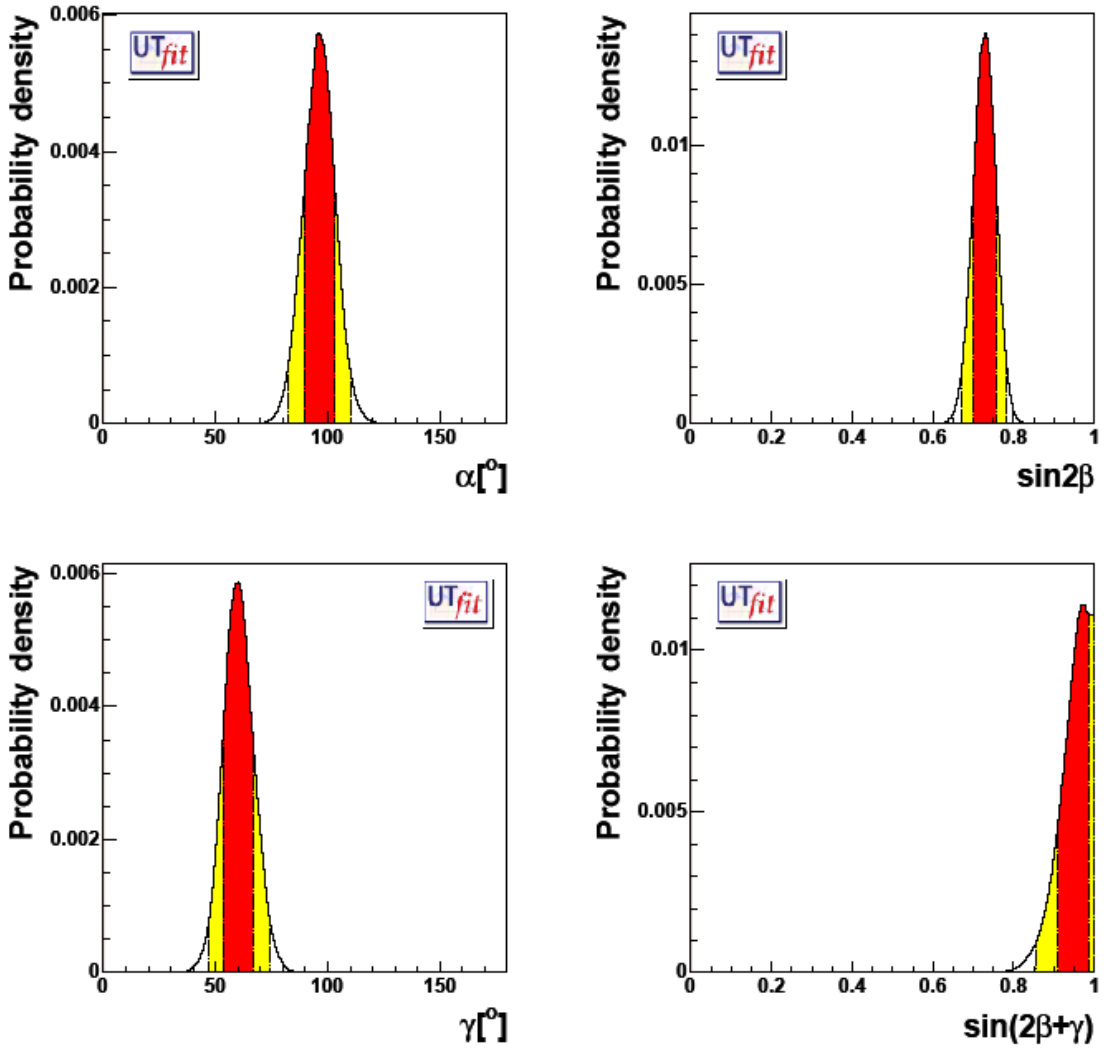

Figure 8.5: From top to bottom and from left to right, the *a posteriori* p.d.f.s for α, $sin2\beta$, γ and $sin(2\beta+\gamma)$. The red (darker) and the yellow (lighter) zones correspond respectively to 68% and 95% of the area.

LQCD, which are used to extract the CKM parameters from the experimental measurements. The overall consistency of the UT fit gives confidence on the theoretical tools.

8.3.4 Indirect determination of Δm_s

Another important outcome of the Unitarity Triangle analysis is the possibility to extract the *a posteriori* p.d.f. for Δm_s, shown in figure 8.7.
The corresponding numerical results, obtained including or not the experimental likelihood

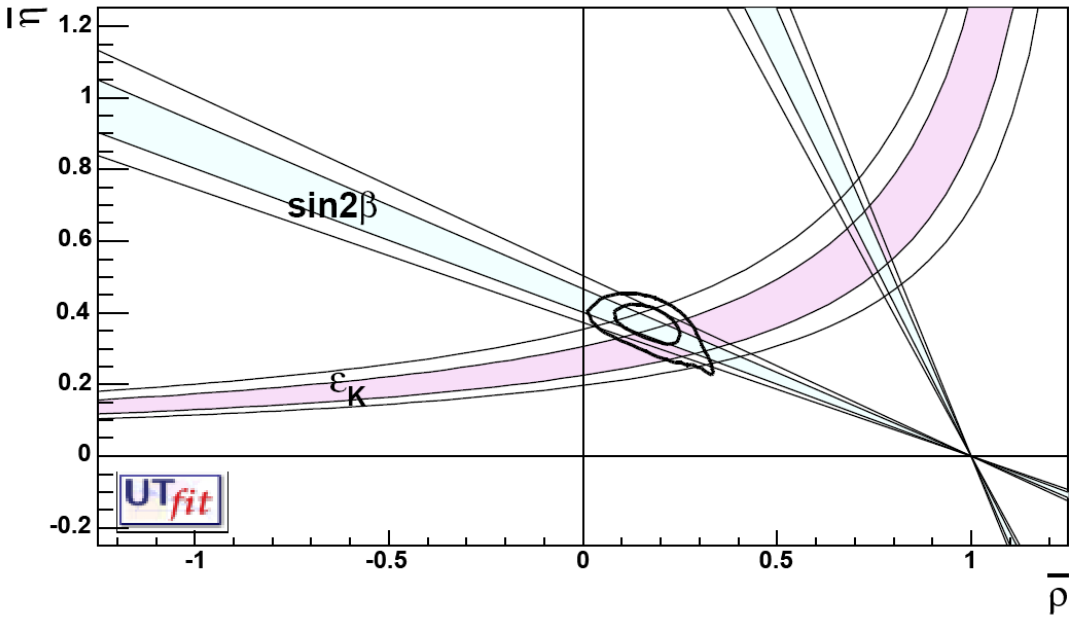

Figure 8.6: Allowed regions for $\overline{\rho}$ and $\overline{\eta}$ (closed contours at 68% and 95% probability ranges), as selected by the measurements of $|V_{ub}|/|V_{cb}|$, Δm_d, and by the limit on Δm_s, are compared with the bands (at 68% and 95% probability ranges) from the measurements of CP-violating quantities in the kaon (ε_K) and in the B ($sin2\beta$) sectors.

Parameter	**68%**	**95%**	**99%**
Δm_s (without Δm_s) (ps^{-1})	21.2 ± 3.2	[15.4, 27.8]	[13.8, 30.0]
Δm_s (including Δm_s) (ps^{-1})	18.5 ± 1.6	[15.6, 23.1]	[15.1, 27.3]

Table 8.3: Central values and ranges for Δm_s corresponding to defined levels of probability, obtained by including or not the experimental information on Δm_s.

for Δm_s in the fit procedure, are given in table 8.3, showing that the inclusion of $B_s - \bar{B}_s$ mixing information in the UT analysis has a large impact on the determination of Δm_s. The present experimental analyses of $B_s - \bar{B}_s$ mixing at LEP and SLD have established a sensitivity of 18.3 ps^{-1} and show an evidence at about $2\,\sigma$ for a positive signal at around 17.5 ps^{-1}, well compatible with the range of the Δm_s distribution from the UT fit.
As will be widely discussed in the following, accurate measurements of Δm_s will provide a fundamental ingredient for testing the Standard Model.

8.4 Tests for new physics: a model independent approach

In general, Standard Model extensions can introduce new physics contributions through many new parameters, e.g. flavour changing couplings, coefficients for short range interactions,

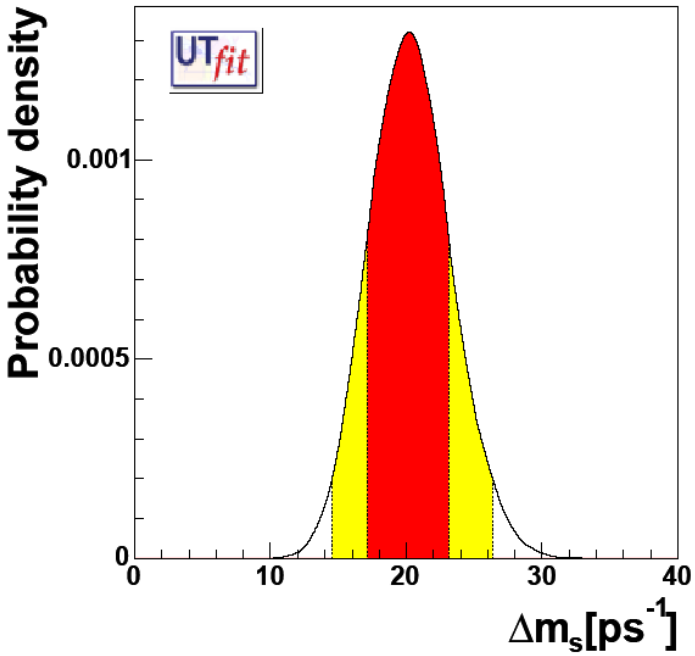

Figure 8.7: Δm_s probability distribution, obtained without using the experimental information from $B_s - \bar{B}_s$ mixing.

matrix elements for new local operators.
Assuming there is no way of having significant new physics effects in the measurement of $|V_{ub}|/|V_{cb}|$ from tree level processes, it is interesting to study the possible contributions to the $B^0_{d,s} - \bar{B}^0_{d,s}$ and $K^0 - \bar{K}^0$ mixings; the complete set of newly introduced parameters strongly depends, anyway, from the details of the adopted model. Anyway, since those mixing processes are described by a single amplitude, their analysis can be performed adopting a model independent approach.
The new physics contributions can be, infact, described in a completely general way as a function of two parameters, the difference in modulus and in phase between the new amplitude and the SM one. As far as the $B^0_q - \bar{B}^0_q$ mixing is concerned, we can define

$$C_q e^{2i\phi_q} = \frac{\langle B^0_q | H^{full}_{eff} | \bar{B}^0_q \rangle}{\langle B^0_q | H^{SM}_{eff} | \bar{B}^0_q \rangle} \qquad (q = d,\ s),$$

where H^{SM}_{eff} contains only the box diagrams foreseen in the Standard Model, while H^{full}_{eff} includes also the new physics contributions. From this definition follows that, in case of no new effects, $C_q = 1$ and $\phi_q = 0$. The experimental observables determined through the study

of $B_q^0 - \bar{B}_q^0$ mixing phenomena are connected to their SM counterparts through the relations

$$\begin{gathered}\Delta m_d = C_d \Delta m_d^{SM}, \\ A_{CP}(J/\psi K_s) = \sin 2(\beta + \phi_d), \\ \Delta m_s = C_s \Delta m_s^{SM}.\end{gathered}$$

Moving to the $K^0 - \bar{K}^0$ mixing, it is convenient to introduce a single parameter connecting the imaginary amplitude part to the corresponding SM one

$$C_\varepsilon = \frac{\mathrm{Im}[\langle K^0 | H_{eff}^{full} | \bar{K}^0 \rangle]}{\mathrm{Im}[\langle K^0 | H_{eff}^{SM} | \bar{K}^0 \rangle]};$$

this implies a simple relation for $|\varepsilon_K|$

$$|\varepsilon_K| = C_\varepsilon |\varepsilon_K|^{SM}.$$

This way, all the new physics contributions that could enter the Unitarity Triangle analysis are parametrized by four real coefficients, C_d, ϕ_d, C_s and C_ε.
Since the limited number of available constraints wouldn't be sufficient to fit all these parameters together, we assume that new physics effects can modify (at least to a first approximation) only one amplitude out of three. This is the only strong assumption done in the present analysis, since it isn't valid in many specific models in which new physics effects enter simultaneously all the amplitudes.
First of all, the contribution to the $K^0 - \bar{K}^0$ mixing will be studied; the CKM fit provides the following indirect measurement

$$C_\varepsilon = 0.85^{+0.19}_{-0.13} \qquad [0.60,\ 1.27] \quad \text{at } 95\% \text{ C.L.}$$

This value is compatible with unity, but its distribution is quite wide. This means that significant new physics contributions are still allowed for the $K^0 - \bar{K}^0$ mixing.
Anyway it can be noticed that the experimental measurement of $|\varepsilon_K|$ can only constrain the product $C_\varepsilon \cdot \hat{B}_K$. So, the large distribution obtained for C_ε simply reflects the theoretical uncertainty on the $\hat{B}_K$ hadronic parameter. Furthermore, it can be shown that, in this scenario, the distributions for the other UT parameters ($\overline{\rho}$, $\overline{\eta}$, $\sin 2\beta$, etc...) almost completely match those obtained using the Standard Model parametrization ($C_\varepsilon = 1$).
Moving to the $B_s^0 - \bar{B}_s^0$ mixing, the distribution found for C_s shows an evident peak at 1; anyway it isn't upper limited, since Δm_s hasn't been experimentally measured yet. In this case too, the distributions for the other UT parameters aren't significantly different from the SM ones ($C_s = 1$).
Finally, the possible new physics contributions to the $B_d^0 - \bar{B}_d^0$ mixing are evaluated. Figure 8.8 shows the two-dimensional distribution for the (C_d, ϕ_d) couple; it can be noticed that two different solutions are possible. The first one shows a peak around Standard Model values ($C_d = 1$ e $\phi_d = 0$); the second one shows, instead, the possibility of really distinct new physics contributions. The presence of two solutions corresponds to the fact that, as shown in figure 8.8,

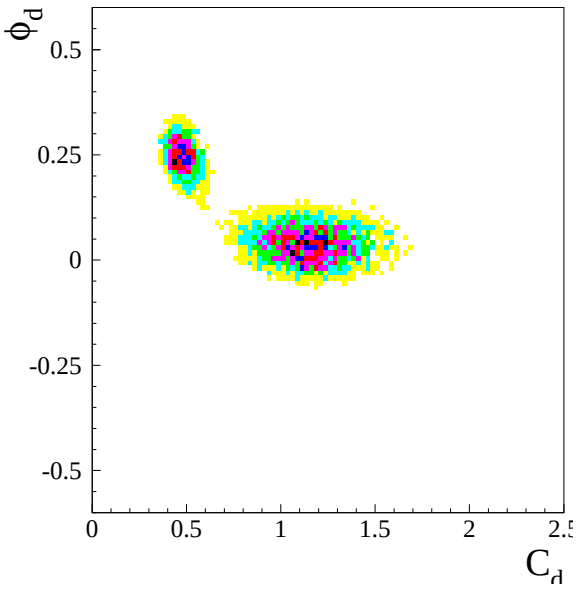

Figure 8.8: Model independent analysis: distribution for the (C_d, ϕ_d) couple.

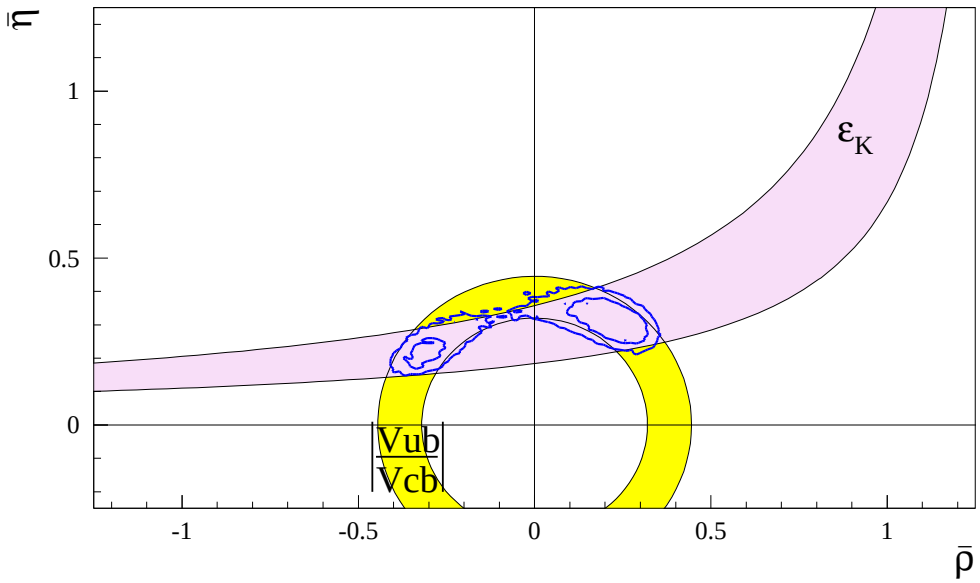

Figure 8.9: Model independent analysis: distribution for the ($\overline{\rho}$, $\overline{\eta}$) couple.

the $|\varepsilon_K|$ constraint crosses the zone allowed by $|V_{ub}|/|V_{cb}|$ in two distinct regions. The region having positive $\overline{\rho}$ values corresponds to the Standard Model solution. In order to discard one solution, an independent measurement of $\overline{\rho}$ or γ is needed. The solution corresponding to a

new physics scenario has been recently discussed in literature [58].
One last comment on the naturalness of this solution; first of all it must be noticed that even there is still room for new physics contributions, these are not needed to provide a coherent picture of the UT. Furthermore, let's suppose that the new physics solution for the $B_s^0 - \bar{B}_s^0$ mixing is indeed the correct one; in this case, it would be rather surprising to find out that, in the Standard Model, which should thus be considered a wrong theory, Δm_d and $\sin 2\beta$ select one of the two regions predicted by $|V_{ub}|/|V_{cb}|$ and $|\varepsilon_K|$ and, in particular, the one discarded by the new physics solution. So, in this sense, the consistency of the new physics solution would be accidental and scarcely natural.

8.5 ATLAS B-physics reach and impact on UT determination

During the last few years B-physics made significant progress, as proved by the results from Unitarity Triangle analysis discussed above. Currently attention is mainly devoted to the measurements provided by B-factories; anyway, also the CDF and D0 experiments have both started to provide preliminary measurements obtained in their new run phase.
Although the physics potential of all these experiments is high, it may well be that the very precise B-decay measurements needed for finding evidence of new physics will be left for the LHC experiments. The LHC should also make possible QCD tests in beauty production in proton-proton collisions at the highest energies.
So, from the ATLAS experiment's point of view, the issue of maximizing B-physics capabilities in the context of a possibly reduced initial T/DAQ system is very important.
In this section a brief overview of the B-physics channels were ATLAS could provide a significant contribution will be given [59].

8.5.1 Precise $sin2\beta$ measurement from $B_d \to J/\psi K_s^0$

The ATLAS sensitivity to the $sin2\beta$ measurement with the $B_d \to J/\psi K_s^0$ decay will be achieved with an analysis method based on maximum likelihood. In particular the most relevant quantities entering this method are the time evolving probability functions describing the $B_d \to J/\psi K_s^0$ and $B_d \to J/\psi K_s^0$ decays, respectively called $W_+(t)$ and $W_-(t)$, and the corresponding complex amplitudes $\mathcal{A}$ and $\bar{\mathcal{A}}$ at time $t = 0$.
In order to provide an estimation for the measurement sensitivity, the time resolution function $\rho(t - t_i)$ was approximated by a Gaussian of width $\sigma = 0.069$ps, while the minimum proper lifetime allowed in the event selection was taken to be 0.5ps.
ATLAS will achieve high sensitivity in this channel by dedicated triggers selecting $J/\psi \to \mu^+\mu^-$ and $J/\psi \to e^+e^-$. Several tagging methods have been tested, using a muon or electron from the associated B-decay, or the charge of the jet that contains a signal B-decay.
Maximal performance should be achievable combining the lower threshold di-muon trigger $\mu 6\mu 3$ with the very low threshold trigger selecting $\mu 6$ at LVL1 and a pair of electrons $e1e1$ by a global track search at LVL2. Combining all tags, a precision on $sin2\beta$ of 0.01 could be achieved after 3 years running at a luminosity of 2×10^{33} cm^{-2} s^{-1}. The most conservative estimate is instead made using only the di-muon higher-threshold trigger $\mu 6\mu 5$. The corresponding precision after 3 years at the same luminosity will be 0.016. It was estimated that

the corresponding systematic uncertainty would be 0.005.

8.5.2 Measurement of Δm_s with $B_s^0 \to D_s\,\pi$ and $B_s^0 \to D_s\,a_1$

In $B_s^0 \to D_s\,\pi$ and $B_s^0 \to D_s\,a_1$ decays the probability p_- that an initially (time $t = 0$) pure B_s^0 will be observed as a B_s^0 and the probability p_+ that it will remain a B_s^0 can be described in terms of Γ, $\Delta Gamma_s$ and Δm_s.
The parameter Δm_s can be thus derived from the ratio:

$$r(t) = \frac{p_+(t) - p_-(t)}{p_+(t) + p_-(t)} = \frac{cos\Delta m_s t}{cosh\Delta\frac{\Gamma_s}{2}t}$$

which is diluted in the case of $\Delta\Gamma_s \neq 0$ by the time dependent hyperbolic function. It was shown however that for $\Delta\Gamma_s/\Gamma < 0.2$ no significant change in the sensitivity range of Δm_s is expected.
More details about the expected ATLAS sensitivity on Δm_s will be given in the next sections.

8.5.3 Measurement of $\Delta\Gamma_s$ and ϕ_s from $B_s^0 \to J/\psi\,\phi$

The $B_s^0 \to J/\psi\,\phi$ decay leads to three final state helicity configurations and their linear combinations are CP eigenstates with different CP parities. This means that it is not possible to extract a CP-violating weak mixing phase $\phi_s = arg(V_{cs}^* V_{cb}/V_{cs}V_{cb}^*)$ if the helicity amplitudes are not separated. The experimental observables are three independent angles and the B_s^0 proper time of the decay $B_s^0 \to J/\psi\phi \to \mu^+\mu^- K^+K^-$. In some cases the initial B_s^0 flavour can also be tagged.
In the analyses proposed for ATLAS, the difference of the mass eigenstate decay rates, $\Delta\Gamma_s$, their average value Γ_s and the weak phase ϕ_s are simultaneously determined along with the two helicity amplitude values and their strong phases. The mixing parameter $x_s \equiv \Delta m_s$ is assumed to be measured as described above. While all eight parameters are independent in the theoretical models, the experimental resolution causes some to become correlated. The di-muon trigger was assumed to select the events with p_T larger than 6 GeV for the first muon and 3 GeV for the second muon.
After 3 years at a luminosity of 10^{33} cm^{-2} s^{-1} the value of $\Delta\Gamma_s$ can be determined with a relative error of 12%. The precision of the ϕ_s determination depends on the value of x_s and on the proper-time resolution, and should be high enough to be sensitive to new physics.

8.5.4 Measurement of rare decays

Flavour changing neutral current decays $b \to s$, $b \to d$ which occur only at loop level in the SM have small exclusive branching ratios $Br < \mathcal{O}(10^{-5})$. They are sensitive to new physics. Within the SM, these decays are sensitive to the CKM matrix elements $|V_{td}|$ and $|V_{ts}|$.
In the era before LHC, some rare decays are accessible at e^+e^- factories and at the Tevatron. In particular, quite accurate measurements should be available for $B \to K^*\gamma$ at the time of LHC start-up. Also the process $B \to K^*\mu^+\mu^-$ could have already been seen by that time; however the mass and angular distributions can only be studied at LHC.

Purely muonic rare decays can, instead, be observed before LHC only if they are drastically enhanced comparing to the SM predictions $Br(B_s^0 \to \mu^+\mu^-) = (3.5 \pm 1.0) \cdot 10^{-9}$ and $Br(B \to \mu^+\mu^-) = (1.5 \pm 1.0) \cdot 10^{-10}$.
Using the simulation of the detector response, ATLAS has demonstrated that purely muonic decays can be selected by the trigger and reconstructed in the offline analyses at both reduced and design luminosities. In particular, already after one year of data-taking at design luminosity, ATLAS will be able to observe $B_s^0 \to \mu^+\mu^-$ and measure its branching ratio and perform a high sensitivity search for $B_d^0 \to \mu^+\mu^-$.

8.6 Prospects for the determination of Δm_s

In this section will be discussed the interest of measuring the Δm_s parameter, in terms of its impact on the UT analysis. In particular will be investigated to which extent a determination of that experimental constraint could allow to possibly invalidate the SM, thus signaling the presence of new physics effects.
The choice of performing this kind of study on Δm_s is guided by two main considerations. First of all, the measurement of this parameter will probably represent the most important B-physics outcome of the ATLAS experiment and, in general, of the experiments operating at LHC. Furthermore, since it is measured in the decay channels posing the most stringent demands on HLT track reconstruction algorithms, its study is strictly related to what described in previous sections.
In particular, after a general discussion on the importance of this measurement with respect to UT determination, the prospects for its achievement in ATLAS will be given; the impact of the LVL2 selection, described in chapter 7, on the experiment's reach will be then discussed.

8.6.1 Impact of Δm_s determination on the UT analysis

As already mentioned in the section devoted to SM tests performed using UT fit results, the study of the compatibility between different constraints can be a powerful tool to spot inconsistencies in the SM picture of flavour physics and, thus providing evidence for new physical phenomena.
In CKM fits based on a χ^2 minimization, a conventional evaluation of compatibility stems automatically from the value of the χ^2 at its minimum. The compatibility between constraints in the bayesian approach is simply done by comparing two different p.d.f.s.
Let us consider, for instance, two p.d.f.s for a given quantity obtained from the UT fit, $f(x_1)$, and from a direct measurement, $f(x_2)$: their compatibility is evaluated by constructing the p.d.f. of the difference variable, $x_2 - x_1$, and by estimating the distance of the most probable value from zero in units of standard deviations. The latter is done by integrating this p.d.f. between zero and the most probable value and converting the integral into the equivalent number of standard deviations for a gaussian distribution. The advantage of this approach is that no approximation is made on the shape of p.d.f.s. In the following analysis, $f(x_1)$ is the p.d.f. predicted by the UT fit while the p.d.f of the measured quantity, $f(x_2)$, is taken Gaussian for simplicity. The number of standard deviations between the hypothetically measured value, $\bar{x}_2 \pm \sigma(x2)$, and the predicted value (distributed according to $f(x_1)$) is plotted

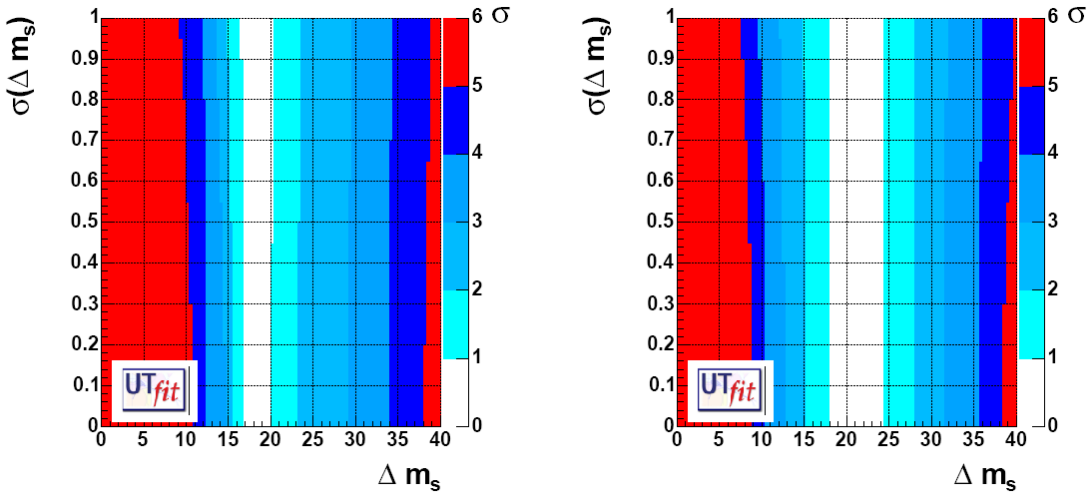

Figure 8.10: The compatibility between the direct and indirect determination of Δm_s, as a function of the value of Δm_s (ps^{-1}), using (left) or ignoring (right) the present experimental bound.

as a function of $\bar{x}_2$ (on the x axis) and $\sigma(x_2)$ (on the y axis). The compatibility between x_1 and x_2 can be then directly estimated on the plot, for any central value and error of the measurement of x_2.
Applying this method to the Δm_s variable, we obtain the plots in figure 8.10, showing the compatibility of the indirect determination of Δm_s with a future determination of the same quantity, obtained using or ignoring the experimental information coming from the present bound.
Given its experimental complexity, the Δm_s measurement will be intrinsically very precise; infact, its value will be measured only once a precision below 1 ps^{-1} will be available. This precision value corresponds to the scale adopted for the compatibility plot.
From figure 8.10 it is evident that, even if the 3σ compatibility region is currently pretty wide and doesn't provide a very stringent constraint on Δm_s, once a measurement of Δm_s with an expected accuracy of ~ 1 ps^{-1} is available, a value of Δm_s greater than 32 ps^{-1} would imply new physics at 3σ level or more. So, the measurement of Δm_s will provide, in future, a reliable tool to test the validity of the Standard Model.
Coming to the impact on UT determination, useful information can be derived from the comparison between the compatibility plots obtained using or ignoring the present experimental bound. As a matter of fact, these show that, even if the current experimental measurement is characterized by a limited significance, its introduction in the fit process grants a much higher precision on the *a posteriori* determination of Δm_s; it can be shown that the same is true for the indirect determination of the other parameters. In conclusion, this means that a direct measurement obtained with an higher significance would allow to greatly refine the quality of the Unitarity Triangle fit.

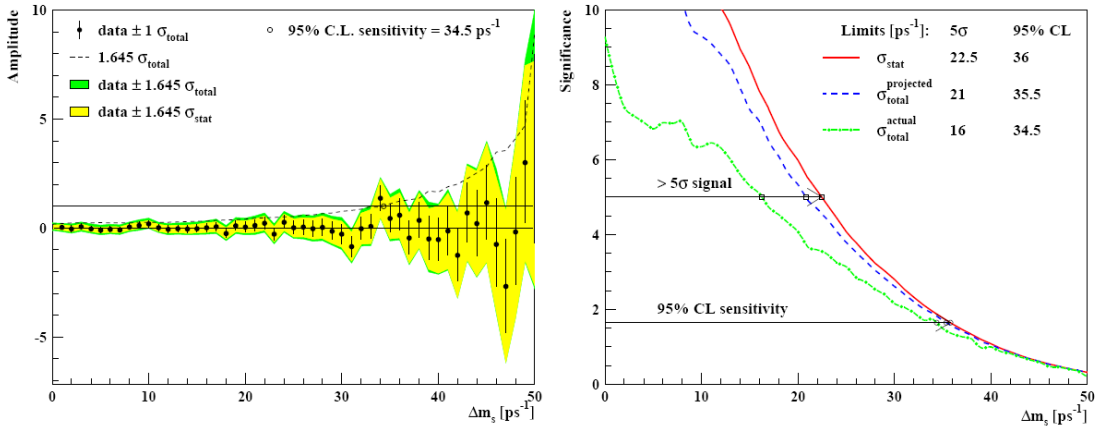

Figure 8.11: The B_s^0 oscillation amplitude as a function of Δm_s (left) and the corresponding measurement significance, again as a function of Δm_s (right); both results are shown for an integrated luminosity of 10 fb^{-1}.

8.6.2 Impact of the trigger selection on Δm_s reach

The maximum value of Δm_s measurable in ATLAS was estimated by the B-physics analysis group, using a simplified Monte Carlo model [60].
In particular, the Δm_s measurement limits were obtained applying the amplitude fit method [61] to the data sample. In this method a new parameter, the B_s^0 oscillation amplitude $\mathcal{A}$, is introduced in the likelihood function by replacing the oscillation term $\mu_0 cos\Delta m_s t_0$ with $\mu_0 \mathcal{A} cos\Delta m_s t_0$ in the B_s^0 probability density function. For each value of Δm_s, the new likelihood function is minimized with respect to $\mathcal{A}$, keeping all other parameters fixed, and a value $\mathcal{A} \pm \sigma_{\mathcal{A}}^{stat}$ is obtained. One expects, within the estimated uncertainty, $\mathcal{A} = 1$ for Δm_s close to its true value, and $\mathcal{A} = 0$ for Δm_s far from the true value. One defines a 5 σ limit as the value of Δm_s for which $1/\sigma_{\mathcal{A}} = 5$, and a sensitivity at 95% confidence limit as the value of Δm_s for which $1/\sigma_{\mathcal{A}} = 1.645$. Limits are computed with the statistical uncertainty $\sigma_{\mathcal{A}}^{stat}$, and, in some cases, with the total uncertainty $\sigma_{\mathcal{A}}^{total} = \sigma_{\mathcal{A}}^{stat} + \sigma_{\mathcal{A}}^{syst}$; the systematic uncertainty takes into account effects such as the wrong-tagging, the parametrization of the proper time resolution or the impact of background events.
Adopting the nominal ATLAS offline parameters, the amplitude as a function of Δm_s for an integrated luminosity of 10 fb^{-1} is shown in figure 8.11, along with the significance of the measurement in units of $\sigma_{\mathcal{A}}$.
The 5σ measurement limit is 22.5 ps^{-1} and the 95% C.L. sensitivity is 36.0 ps^{-1}, when computed with the statistical uncertainty only. Computed with the total uncertainty, the 5σ measurement limit is 16.0 ps^{-1} and the 95% C.L. sensitivity is 34.5 ps^{-1} for the actual systematic uncertainties, and 21 ps^{-1} and 35.5 ps^{-1} in case the uncertainty on the proper time resolution can be reduced to half of the standard value (this scenario will be referenced as the one adopting projected systematic in the following).

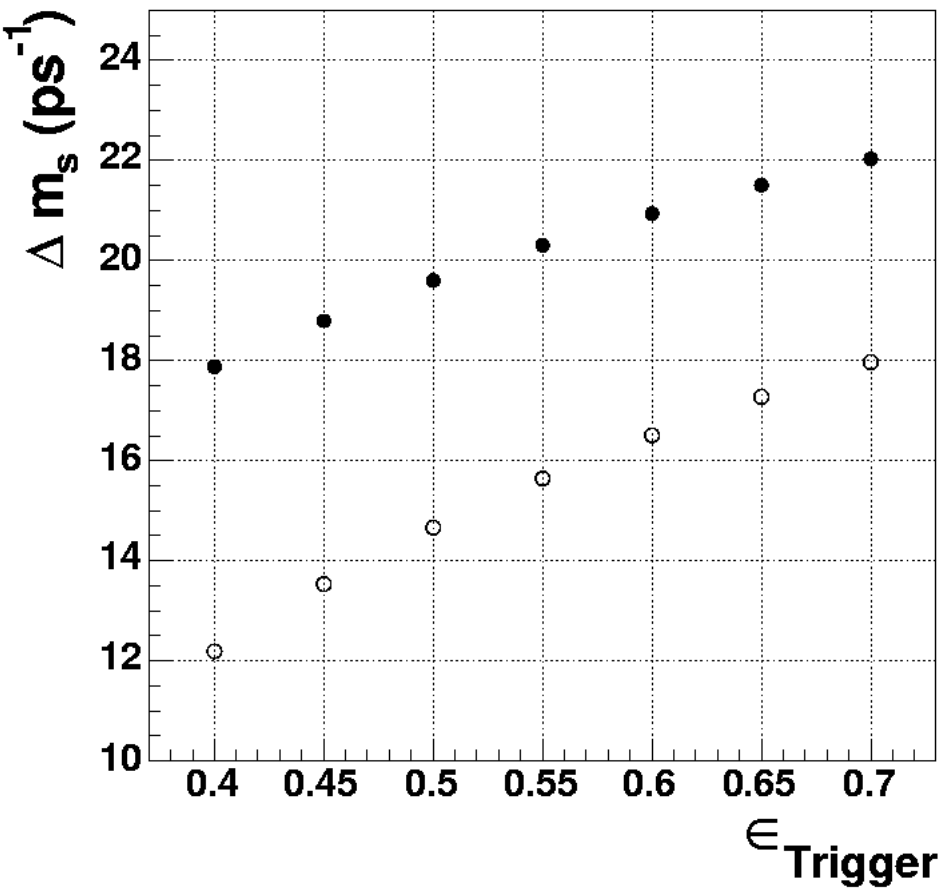

Figure 8.12: Dependence of 5σ measurement limits for Δm_s on the trigger efficiency; results are given for an integrated luminosity of 10 fb^{-1}; the lower curve refers to standard systematic contributions, while the upper one assumes the projected scenario is valid.

All these results assume a 63% efficiency for the semi-inclusive LVL2 selection of D_s candidates, evaluated from previous studies tuned for operation at a luminosity of 10^{33} cm^{-2} s^{-1}. This trigger study also assumed a full detector scenario, where the pixel B-layer was 1 cm closer to the beam line, providing much more precise track parameters; it must be noticed that much more pessimistic conditions have been adopted for the study presented in chapter 7.

In order to correctly study the impact of the trigger selection described in chapter 7 on the ATLAS Δm_s reach, the dependence of Δm_s measurement limits on the trigger efficiency has been evaluated; the resulting curve is shown in figure 8.12.

It can be noticed how the ATLAS Δm_s reach is not spoiled even for trigger efficiencies lower

than 60%.
Finally the current conclusive considerations can drawn:

- the current ATLAS reach covers, even in the most optimistic case, only the Δm_s interval compatible with the indirect measurements provided by UT analysis and discussed before; this means that, at integrated luminosities around 10 fb^{-1} it will not be possible to spot incoherences of the measured value with respect to the SM prediction;

- the previous chapter showed that the main limitations to the trigger strategy come from the background rate passing the trigger selection; anyway affordable rates were obtained in case the selection was tuned for a signal efficiency around 40%. This choice doesn't spoil the Δm_s reach but simply implies that a larger integrated luminosity will be needed to achieve the same sensitivity quoted in previous studies, which assumed efficiencies around 60%. On the other hand those studies referred to a luminosity of 10^{33} cm^{-2} s^{-1}, which means that the factor of 1.5 lost by the efficiency decrease will be recovered by the fact that, operating at a doubled luminosity, a doubled number of signal events is gathered in the same time period.

Conclusions

In the present work a complete characterization of the SiTrack track reconstruction algorithm was provided. This has been carried out operating at three different levels:

- providing the results of studies on tracking performance, aimed at testing the algorithm's capability of operating on different event topologies and in different luminosity conditions;
- adapting the algorithm to the different trigger menu signatures and studying its impact on trigger selection performance; in most cases this also led to the definition of new trigger selection strategies;
- studying, in one detailed case, the impact of a trigger selection based on SiTrack on the physics reach of the ATLAS experiment.

The first item has been covered studying track reconstruction performance for two different topologies, corresponding to events containing single isolated particles and jets.
In both cases a good reconstruction efficiency has been obtained, while, at the same time, the fraction of fake track candidates was kept under control. Tracking performance proved robust with respect to changes in the luminosity conditions, since no major performance changes were spotted moving from start-up (2×10^{33} cm^{-2} s^{-1}) to design luminosity (1×10^{34} cm^{-2} s^{-1}).
Furthermore SiTrack's adaptability was demonstrated; infact it was shown how, acting on track reconstruction cut variables, it is possible to tune its p_T acceptance or to move the balance between reconstruction efficiency and rejection of fake candidates. This feature is particularly useful when adapting the algorithm to different physical selection strategies.
Finally, the timing performance of the algorithm was measured for the above mentioned samples; in all cases, the average execution time resulted compatible with the constraints posed by operation in the LVL2 framework. A further safety margin is provided by the fact that all the measurements reported in this work have been obtained on processors slower than the ones that will be adopted for the ATLAS HLT operation.
The second item was covered performing detailed studies of the trigger selection performance for three different kinds of physical signatures:

- identification of high momentum isolated electrons; in this signature, tracks reconstructed in the Inner Detector are matched to energy deposits in the calorimeters in order to reject fake electron candidates and to provide combined particle identification

capabilities. Results obtained from studies on simulated samples showed that the fake electron candidates rejection obtained employing SiTrack at LVL2 is significant and, in particular, is crucial in order to meet the rate constraints at the boundary between the LVL2 and the EF processing;

- identification of jets containing beauty hadrons; for this selection, SiTrack was tuned to achieve a very low fraction of fake track candidates, since a high purity of the reconstructed sample is mandatory in flavour tagging applications. Furthermore, the proposed b-jet selection, integrating for the first time different tagging methods, showed a significant improvement of the light quark jet rejection, especially for high b-jet selection efficiencies with respect to the previous studies. This result is very important since most b-tagging applications concern multi b-jets events; this way the b-jet selection can be used to restore an acceptable LVL2 output rate if the LVL1 thresholds are loosened to increase signal efficiency. Finally, the b-tagging selection proved very stable as a function of the luminosity regimes, allowing its usage in different running conditions;

- selection of decay channels relevant to B-physics studies; in this case SiTrack was tuned to achieve the highest possible reconstruction efficiency down to p_T values around 1.5 GeV. Then it was applied to the semi-inclusive $D_s \to \phi\pi$ and to the exclusive $B_s \to D_s\pi$ selections, relevant for the Δm_s measurement. In both cases a set of possible trigger configurations was studied, providing the resulting efficiency for signal events along with the corresponding rate for background events. These studies showed that an RoI based approach to this kind of selection is feasible, even if it introduces an additional inefficiency factor around 20%. It was also shown that, operating at full start-up luminosity (2×10^{33} cm^{-2} s^{-1}), the resulting rates would occupy a significant fraction of the LVL2 trigger budget; anyway this problem should be overcome operating this selection only at lower luminosities (below 1×10^{33} cm^{-2} s^{-1}), as foreseen by the baseline ATLAS B-trigger strategy. Anyway, in case the exclusive selection of $B_s \to D_s\pi$ decays is adopted, losing about 10% of signal efficiency, the LVL2 output rate is reduced to an affordable value even in the start-up luminosity scenario.

Finally, the impact of a trigger selection based on SiTrack on the physics reach of the ATLAS experiment was studied for the selection of $B_s \to D_s\pi$ decays, which are relevant for the study of $B_s^0 - \bar{B}_s^0$ mixing properties and for the measurement of their Δm_s parameter.
In particular, the prospects for the determination of Δm_s have been studied as a function of the trigger selection efficiency. This study showed that, for an integrated luminosity of 10 fb^{-1} (collected in six months of operation at start-up luminosity), the 5σ measurement limit ranges between 18 and 22 ps^{-1}, exceeding the current experimental limit and allowing to cover a large part of the Δm_s interval compatible with the Standard Model picture of flavour physics.

Bibliography

[1] S. Weinberg *The Making of the Standard Model*, hep-ph/0401010 (2004).

[2] M. Gell-Mann, Phys. Lett. 8, 214 (1964); G. Zweig, CERN preprint TH401 (1964).

[3] E. D. Bloom et al., Phys. Rev. Lett. 23, 930 (1969); M. Briedenbach et al., Phys. Rev. Lett. 23, 935 (1969); J. L. Friedman and H. W. Kendall, Annual Reviews of Nuclear Science 22, 203 (1972).

[4] C. N. Yang and R. L. Mills, Phys. Rev. 96, 191 (1954).

[5] J. Goldstone, A. Salam, and S. Weinberg, Phys. Rev. 127, 965 (1962).

[6] P. W. Higgs, Phys. Lett. 12, 132 (1964); Phys. Lett. 13, 508 (1964); Phys. Rev. 145, 1156 (1966).

[7] S. Weinberg, Phys. Rev. Lett. 19, 1264 (1967).

[8] A. Salam, in Elementary Particle Physics, N. Svartholm, ed. (Nobel Symposium No. 8, Almqvist and Wiksell, Stockholm, 1968), p. 367.

[9] T. P. Cheng and L. F. Li, *Gauge theory of elementary particle physics*, Clarendon Press (1984).

[10] S. Weinberg, Phys. Rev. 5, 1412 (1972).

[11] D. C. Cundy et al., Phys. Lett. B 31, 478 (1970).

[12] F. J. Hasert et al., Phys. Lett. B 46, 121, 138 (1973); P. Musset et al., J. Phys. (Paris) 11/12, T34 (1973).

[13] C. Y. Prescott et al., Phys. Lett. 77B, 347 (1978).

[14] M. Perl et al. Phys. Rev. Lett. 35, 195, 1489 (1975); Phys. Lett. 63B, 466 (1976).

[15] S. W. Herb et al., Phys. Rev. Lett. 39, 252 (1975).

[16] F. Abe et al., Phys. Rev. Lett. 74, 2626 (1995); S. Abachi et al., Phys Rev. Lett. 74, 2632 (1995).

[17] N. Cabibbo, Phys. Rev. Lett. 10, 531 (1963); M. Kobayashi and K. Maskawa, Prog. Theor. Phys. 49, 282 (1972).

[18] G. Arnison et al., Phys. Lett. 122B, 103 (1983); 126B, 398 (1983); 129B, 273 (1983); 134B, 469 (1984); 147B, 241 (1984).

[19] M. W. Grünewald *Electroweak Precision Data - Global Higgs Analysis*, hep-ex/0304023, UCD-EXPH-2003-04-01 (2003).

[20] The LEP Collaborations ALEPH, DELPHI, L3, OPAL, the LEP Electroweak Working Group and the SLD Heavy Flavour Group *A Combination of Preliminary Electroweak Measurements and Constraints on the Standard Model*, hep-ex/0312023, LEP-EWWG-2003-02 (2003).

[21] Paper on vacuum stability and Higgs constraints.

[22] R. N. Mohapatra *Unification and Supersymmetry: The frontiers of quark-lepton physics*, Springer-Verlag (1992).

[23] BaBar Experiment Technical Design Report.

[24] Belle Experiment Letter of Intent.

[25] MEG Letter of Intent.

[26] CDF Technical Design Report.

[27] F. Abe et al. *Observation of top quark production in anti-p p collisions* Phys. Rev. Lett. 74, 2626 (1995)

[28] LHC Design Report.

[29] CMS Technical Design Report.

[30] LHCb Technical Design Report.

[31] ALICE Technical Design Report.

[32] ATLAS Collaboration *ATLAS Detector and Physics Performance: Technical Design Report*, CERN-LHCC-99-014/015 (1999).

[33] ATLAS Collaboration *ATLAS: Inner Detector Technical Design Report*, CERN-LHCC-97-016/017 (1997).

[34] ATLAS Collaboration *ATLAS: Liquid Argon Technical Design Report*, CERN-LHCC-96-041 (1996).

[35] ATLAS Collaboration *ATLAS: Tile Calorimeter Technical Design Report*, CERN-LHCC-96-042 (1996).

[36] ATLAS Collaboration *ATLAS: Muon Spectrometer Technical Design Report*, CERN-LHCC-97-022 (1997).

[37] ATLAS Collaboration *ATLAS High Level Trigger, Data Acquisition and Controls Technical Design Report*, CERN/LHCC/03-022 (2003).

[38] ATLAS Collaboration *ATLAS First-Level Trigger Technical Design Report*, CERN/LHCC/98-014 (1998).

[39] T. Schörner-Sadenius, S. Tapprogge *ATLAS Trigger Menus for the LHC Start-Up Phase*, ATLAS Note ATL-DAQ-2003-004 (2003).

[40] ATLAS Collaboration *ATLAS High Level Trigger, DAQ and DCS Technical Proposal*, CERN/LHCC/2000-17 (2000).

[41] S. Armstrong et al. *An Overview of Algorithms for the ATLAS High Level Trigger*, ATL-CONF-2003-003, ATL-DAQ-2003-029 (2003).

[42] *http://atlas.web.cern.ch/Atlas/GROUPS/SOFTWARE/OO/architecture/General*

[43] G. Barrand et al. *Gaudi-A Software Architecture and Framework for Building HEP Data Processing Applications*, Comput. Phys. Commun. 140 (2001) 45.

[44] A. Baratella, M. Dameri, P. Morettini, F. Parodi *PixTrig: a LVL2 track finding algorithm based on pixel detector*, ATLAS-DAQ-2000-25 (2000).

[45] B. Stroustrup *The C++ Programming Language (3rd edition)*, Addison Wesley Longman (1997).

[46] E. J. W. Moyse and A. T. Watson *Performance and Validation of TrigT1Calo, the offline Level-1 Calorimeter Trigger Simulation*, ATLAS Internal Note, ATL-DAQ-2003-027 (2003)

[47] C. Schiavi on behalf of the ATLAS HLT group *Implementation and Performance of the High Level Trigger Electron and Photon Selection for the ATLAS Experiment at the LHC*, to be published on IEEE Transaction on Nuclear Science

[48] M. Cervetto, P. Morettini, F. Parodi, C. Schiavi *b-tagging Event Selection for the ATLAS High Level Trigger: an update*, ATL-COM-DAQ-2003-34 (2003).

[49] S. George *The ATLAS B-physics Trigger*, ATLAS Note ATL-DAQ-2004-004 (2004).

[50] B. Epp, V. M. Ghete, A. Watson *A study of the use of low E_T calorimeter RoI in the ATLAS B-trigger*, ATLAS Note ATL-COM-DAQ-2003-036 (2003).

[51] J. T. M. Baines et al. *B-Physics Event Selection for the ATLAS High Level Trigger*, ATLAS Note ATL-DAQ-2000-031 (2000).

[52] M. E. Peskin, D. V. Schroeder, *An Introduction to Quantum Field Theory*, Westview Press.

[53] L. Wolfenstein, *Phys. Rev. Lett.* **51** (1983) 1945.

[54] A. J. Buras, M. E. Lautenbacher, G. Ostermaier, *Phys. Rev. D* **50** (1994) 3433.

[55] M. Schmidtler, K. R. Schubert, *Z. Phys. C* **53** (1992) 347.

[56] M. Ciuchini, G. DAgostini, E. Franco, V. Lubicz, G. Martinelli, F. Parodi, P. Roudeau, A. Stocchi, *JHEP* **0107** (2001) 013, [hep-ph/0012308].

[57] M. Bona et al. [UTfit Collaboration], *The 2004 UTfit collaboration report on the status of the unitarity triangle in the standard model*, arXiv:hep-ph/0501199.

[58] R. Fleischer, G. Isidori, J. Matias, *JHEP* **0305** (2003) 053, arXiv:hep-ph/0302229. G. Isidori, arXiv:hep-ph/0307014.

[59] M. Smizanska, *ATLAS: B Physics Reach*, ATLAS Scientific Note, SN-ATLAS-2003-033 (2003).

[60] B. Epp, V. M. Ghete, A. Nairz, *Prospects for the measurement of B_s^0 oscillations with the ATLAS detector at LHC*, ATLAS Scientific Note, SN-ATLAS-2002-015 (2002).

[61] H. G. Moser, A. Roussarie, Nucl. Instr. Meth. A384 (1997) 491.